



**Universidade do Estado do Rio de Janeiro**

Centro de Tecnologia e Ciências

Faculdade de Geologia

Gilmar Pachá Corrêa dos Santos da Silva

**O magmatismo do Oligo–Mioceno na Província Magmática  
Somuncurá, Argentina, e a relação com a subdução andina**

Rio de Janeiro

2024

Gilmar Pachá Corrêa dos Santos da Silva

**O magmatismo do Oligo–Mioceno na Província Magmática Somuncurá,  
Argentina, e a relação com a subdução andina**

Dissertação de Mestrado apresentada, como  
requisito parcial para obtenção do título de  
Mestre, ao Programa de Pós-Graduação em  
Geociências, da Universidade do Estado do Rio  
de Janeiro. Área de concentração:  
Geociências.

Orientador: Prof. Dr. Anderson Costa dos Santos (UERJ)  
Coorientadores: Prof. Dr. Eduardo Reis Vianna Rocha-Júnior (UFBA)  
Prof. Dr. Leonardo Benedini (UNS)

Rio de Janeiro

2024

**CATALOGAÇÃO NA FONTE  
UERJ/REDE SIRIUS/CTCC**

S586	<p>Silva, Gilmar Pachá Corrêa dos Santos da. O magmatismo do Oligo-Mioceno na Província Magmática de Somuncurá, Argentina, e a relação com a subdução andina / Gilmar Pachá Corrêa dos Santos da Silva. – 2024. 150 f.: il.</p> <p>Orientador: Anderson Costa dos Santos. Coorientadores: Eduardo Reis Vianna Rocha-Júnior e Leonardo Benedini.</p> <p>Dissertação (Mestrado) - Universidade do Estado do Rio de Janeiro, Faculdade de Geologia.</p> <p>1.Magnetismo – Teses. 2. Geoquímica - Teses. 3. Geologia isotópica – Teses. I. Santos, Anderson Costa dos. II. Rocha-Júnior, Eduardo Reis Vianna. III. Benedini, Leonardo. IV. Universidade do Estado do Rio de Janeiro. Faculdade de Geologia. V. Título.</p> <p style="text-align: right;">CDU 553.3(82)</p>
	Bibliotecária responsável: Ingrid Pinheiro / CRB-7: 7048

Autorizo, apenas, para fins acadêmicos e científicos, a reprodução total ou parcial desta dissertação, desde que citada a fonte.

---

Assinatura

---

Data

Gilmar Pachá Corrêa dos Santos da Silva

**O magmatismo do Oligo-Mioceno na Província Magmática de Somuncurá,  
Argentina, e a relação com a subdução andina**

Dissertação de Mestrado apresentada, como  
requisito parcial para obtenção do título de  
Mestre, ao Programa de Pós-Graduação em  
Geociências, da Universidade do Estado do Rio  
de Janeiro. Área de concentração:  
Geociências.

Orientador: Prof. Dr. Anderson Costa dos Santos

Faculdade de Geologia - UERJ

Coorientadores: Prof. Dr. Leonardo Benedini

Universidad Nacional del Sur - UNS

Prof. Dr. Eduardo Reis Vianna Rocha - Júnior

Universidade Federal da Bahia – UFBA

Banca Examinadora:

---

Prof.<sup>a</sup> Dr<sup>a</sup>. Cecília Pavón Pivetta

Universidad Nacional del Sur - UNS

---

Prof.<sup>a</sup> Dr<sup>a</sup>. Letícia Freitas Guimarães

Universidade Federal da Bahia - UFBA

---

Prof. Dr. Valdecir de Assis Janasi

Universidade de São Paulo - USP

Rio de Janeiro

2024

## **DEDICATÓRIA**

Dedico esse trabalho a todos os cientistas que lutam pela sua pesquisa, que fazem da ciência sua vida, do laboratório sua sala de estar e do resultado um sonho feliz.  
Viva a ciência!

## **AGRADECIMENTOS**

Todos sabemos que não é fácil fazer ciência no Brasil, seja pela falta de apoio, pelo não reconhecimento social, pela falta de verba para projeto e/ou pela bolsa curta.

Sendo assim, gostaria de agradecer o apoio e a motivação que algumas pessoas me transmitiram, não hoje e nem ontem, porém ao longo de anos de convivência.

Primeiramente gostaria de agradecer a toda energia que me manteve firme e na luta, para a realização e conclusão desse projeto.

Segundo, gostaria de agradecer a minha prima Mariana Pachá, que em janeiro de 2022 me motivou enormemente para a realização da minha inscrição. Junto dela, gostaria de agradecer ao meu marido, Ariel Pachá, por todo apoio que também me deu, não só no momento da inscrição, mas a cada novo desafio que enfrentei.

Agradeço também à minha mãe, Nádia Pachá, e ao meu irmão, Guilherme Pachá, por todo apoio e torcida que tiveram ao longo desses dois anos.

Aos meus amigos, Giovanni Oliveira, Juliana Bonifácio, Mariana Bessa e Mateus Andrade, sempre meus maiores conselheiros e ouvintes dos meus podcasts ou “Pachacasts”, como eles gostam de chamar, meu eterno obrigado.

Grato ao meu orientador e coorientadores por embarcarem em mais esse desafio comigo.

A todos, minha gratidão!

Escrevendo o passado, no presente, para o futuro

*O autor*

## RESUMO

SILVA, Gilmar Pachá Corrêa dos Santos da. **O magmatismo do Oligo-Mioceno na Província Magmática de Somuncurá, Argentina, e a relação com a subdução andina.** 2024. 150 f. Dissertação (Mestrado em Geociências) – Faculdade de Geologia, Universidade do Estado do Rio de Janeiro, Rio de Janeiro, 2024.

O complexo alcalino da Sierra de Apas, localizada na Província Magmática de Somuncurá, Patagônia Norte, Argentina, se desencolveu ao longo do Oligoceno-Mioceno. A dissertação apresenta diferentes metodologias para estudar a evolução magmática da Sierra de Apas. A pesquisa integrou análises petrográficas, litogeoquímicas, isotópicas (Sr-Nd) e geocronológicas (U-Pb em apatita). A área é caracterizada por um magmatismo bimodal, com lavas basálticas e traquíticas, seguido por rochas mais evoluídas, como os riolitos. As idades U-Pb obtidas, indicam que os eventos vulcânicos ocorreram em média a 25 Ma, relacionando-se ao desenvolvimento de caldeiras e colapsos magmáticos na região. As sucessões vulcanicas foram caracterizadas em 11 elementos vulcânicos que envolvem três eventos evolutivos maiores: pré-colápsio, sin-colápsio e pós-colápsio. Os dados litogeoquímicos mostram teores de SiO<sub>2</sub> variando de 42 a 78 wt.%, com enriquecimento em elementos incompatíveis, como Zr (600-2000 ppm) e Nb (50-80 ppm). As análises de terras raras indicam concentrações elevadas de Y e La, sobretudo nas rochas traquíticas e comendíticas. O controle predominante da cristalização fracionada é evidenciado pela separação clara entre os magmas máficos e felsicos nos diagramas de Harker. Os valores isotópicos variam com <sup>87</sup>Sr/<sup>86</sup>Sr(m) entre 0,703723 e 0,900385, e <sup>143</sup>Nd/<sup>144</sup>Nd(m) de 0,512606 a 0,512894, indicando contribuições mistas do manto empobrecido e processos crustais. A modelagem isotópica mostrou que as traquitas e comenditas exibem valores de <sup>87</sup>Sr/<sup>86</sup>Sr(i) entre 0,703690 e 0,767785, refletindo contaminação crustal mais acentuada. O  $\epsilon$ Nd(i) variou de -0,3 a +5,3, destacando a influência de fontes mantélicas mais juvenis em algumas amostras. Os diagramas de modelagem geoquímica, como Nb vs. La, indicam que a cristalização fracionada foi o processo dominante, enquanto o comportamento de alguns traquitos e comenditos evidencia assimilação crustal. A evolução dos magmas foi ainda marcada por processos de fusão parcial e recarga mantélica, sugerindo um complexo sistema magmático com interações mantélicas e crustais em um ambiente tectônico modificado pela subdução andina. Em síntese, a dissertação contribui para o entendimento do magmatismo intraplaca na Patagônia, elucidando a interação entre subducção e plumas mantélicas, além de oferecer novos dados sobre a evolução de magmas alcalinos e sua relação com processos tectônicos regionais.

Palavras-chave: magmatismo alcalino; magmatismo bimodal; magmatismo intraplaca; cristalização fracionada; evolução magmática.

## ABSTRACT

SILVA, Gilmar Pachá Corrêa dos Santos da. **Oligo-Miocene magmatism in the Somuncurá Magmatic Province, Argentina, and its relationship with Andean subduction.** 2024. 150 f. Dissertação (Mestrado em Geociências) – Faculdade de Geologia, Universidade do Estado do Rio de Janeiro, Rio de Janeiro, 2024.

The alkaline complex of the Sierra de Apas, situated in the Somuncurá Magmatic Province of Northern Patagonia, Argentina, developed throughout the Oligocene-Miocene epoch. This dissertation comprehensively examines various methodologies employed to investigate the magmatic evolution of the Sierra de Apas. The research integrates petrographic, lithogeochemical, isotopic (Sr-Nd), and geochronological (U-Pb in apatite) analyses. The region is characterized by bimodal magmatism, comprising basaltic and trachytic lavas, succeeded by more evolved lithologies such as rhyolites. The U-Pb ages obtained suggest that volcanic events occurred, on average, approximately 25 million years ago, correlating with the development of calderas and magmatic collapses within the area. The volcanic succession is categorized into eleven volcanic elements, encompassing three principal evolutionary events: pre-collapse, syn-collapse, and post-collapse. Lithogeochemical data reveal  $\text{SiO}_2$  concentrations ranging from 42 to 78 wt.%, alongside enrichments in incompatible elements such as Zr (600-2000 ppm) and Nb (50-80 ppm). Analyses of rare earth elements indicate elevated concentrations of Y and La, particularly in trachytic and commenditic rocks. The predominant influence of fractional crystallization is evidenced by a distinct separation between mafic and felsic magmas in Harker diagrams. Isotopic values exhibit variability, with  $^{87}\text{Sr}/^{86}\text{Sr}(m)$  ranging from 0.703723 to 0.900385 and  $^{143}\text{Nd}/^{144}\text{Nd}(m)$  spanning 0.512606 to 0.512894, indicating mixed contributions from a depleted mantle and crustal processes. Isotopic modeling reveals that trachytes and commendites display  $^{87}\text{Sr}/^{86}\text{Sr}(i)$  values between 0.703690 and 0.767785, reflecting a pronounced degree of crustal contamination. The  $\epsilon\text{Nd}(i)$  values ranged from -0.3 to +5.3, underscoring the influence of more juvenile mantle sources in certain samples. Geochemical modeling diagrams, such as Nb vs. La, indicate that fractional crystallization was the prevailing process, whereas the behavior of select trachytes and commendites suggests crustal assimilation. The magmatic evolution was also characterized by partial melting and mantle recharge processes, indicating a complex magmatic system with interactions between mantle and crust in a tectonically modified environment shaped by Andean subduction. In conclusion, this dissertation enhances the understanding of intraplate magmatism in Patagonia, elucidating the interplay between subduction and mantle plumes while providing novel insights into the evolution of alkaline magmas and their association with regional tectonic processes.

Keywords: alkaline magmatism; bimodal magmatism; intraplate magmatism; fractional crystallization; magmatic evolution.

## **LISTA DE FIGURAS**

Figura 1 -	Mapa produzido por Wichmann (1927).....	15
Figura 2 -	Mapa esquemático com a localização dos principais magmatismos cenozoicos e as zonas magnáticas da Patagônia Argentina.....	21
Figura 3 -	Mapa de localização da Província Magmática de Somuncurá, <i>Sierra de Apas</i> , estradas e cidades.....	30
Figura 4 -	Imagen de satélite da <i>Sierra de Apas</i> e a localização das amostras utilizadas.....	31

## **LISTA DE TABELAS**

Tabela 1 -	Síntese dos eventos tectônicos ígneos e metamórficos paleozoicos da PMSC.....	19
Tabela 2 -	Síntese da formação da Província Magmática de Somuncurá (PMSC) e do embasamento mesozoico.....	23
Tabela 3 -	Divisão proposta por Kay et al. (2007) para classificar o magmatismo da Província Magmática de Somuncurá.....	24

## SUMÁRIO

<b>INTRODUÇÃO.....</b>	11
<b>1 OBJETIVOS.....</b>	14
<b>2 GEOLOGIA.....</b>	15
<b>2.1 Hipóteses de formação da Patagônia.....</b>	16
<b>2.2 Embasamentos pré-mesozoico.....</b>	17
<b>2.3 Embasamento mesozoico.....</b>	19
<b>2.4 Província Magmática de Somuncurá (PMSC).....</b>	21
<b>3 MATERIAIS E MÉTODOS.....</b>	24
<b>3.1 Campo.....</b>	24
<b>3.2 Preparação de amostras.....</b>	25
<b>3.3 Petrografia.....</b>	25
<b>3.4 Litogeoquímica.....</b>	26
<b>3.5 Microssonda.....</b>	26
<b>3.6 Geocronologia.....</b>	26
<b>3.7 Isótopos.....</b>	28
<b>4 LOCALIZAÇÃO.....</b>	29
<b>5 RESULTADOS.....</b>	32
<b>6 CONCLUSÃO.....</b>	33
<b>REFERÊNCIAS.....</b>	35
<b>APÊNDICE A - Artigo 1.....</b>	42
<b>APÊNDICE B - Artigo 2.....</b>	71
<b>APÊNDICE C - Sample Table.....</b>	144
<b>APÊNDICE D - Petrographic Table.....</b>	145

## INTRODUÇÃO

A Província Magmática Somuncurá (PMSC), no Norte da Patagônia Argentina, se desenvolveu em um intervalo de tempo compreendido entre o Oligoceno e o Mioceno (29 a 17 Ma, Kay et al. 2007). Interpretado como o maior campo vulcânico *back-arc* da Patagônia, segundo Kay et al. (2007), correspondendo à uma área de 55 mil km<sup>2</sup>, sendo, assim, um dos maiores eventos vulcânicos do mundo tendo sua relação com a subdução andina, *hotspot* e metassomatismo discutida ao longo dos anos (Navarrete et al. 2020).

No *back-arc*, o magmatismo pode ser associado às zonas de subdução, tendo uma composição e propriedades físicas diferentes do magmatismo de arco. O afinamento da espessura da litosfera em conjunto com esforços extensionais permitindo a ascensão do manto. A geoquímica, dos magmas do *back-arc*, apresenta uma assinatura de subdução, quando analisados os elementos traços e a adição de fluidos derivados da desidratação da placa oceânica durante o processo de subdução (Pearce and Stern, 2006). Sendo importante considerar os efeitos de mudanças na dinâmica da subdução, possível rotação e ruptura de placas, e a associação com o fluxo do manto (Magni, 2019).

O contexto histórico das placas Nazca-Sul Americana desempenha um papel crucial na compreensão da evolução da PMSC. Após a ruptura da placa de *Farallon* formando as placas de Nazca, Cocos e Juan de Fuca, que ocorreu entre 26-28 Ma (Herron e Heitzler, 1967), a velocidade da convergência da placa de Nazca com a placa Sul-Americana aumentou de 5-6 cm/ano para 14 cm/ano, entre as latitudes 37° - 42°S (Cordenons, 2017). Este processo, de organização das placas, com mudanças de ângulo e velocidades de subdução, está intrinsecamente ligado ao magmatismo ocorrido no período Oligo-Mioceno (De Ignacio et al. 2001).

A região vem sendo alvo de estudo desde o final do século XIX e início do século XX, e.g. Doering (1882), Ameghino (1898), e Windhausen (1921). No entanto, nos últimos 30 anos, estudos estratigráficos, morfológicos, petrológicos, tectônicos e escassas informações estratigráficas relacionadas com o planalto foram realizados por inúmeros autores (e.g. Kay, et al. 1993; Ardolino e Franchi 1993; Remesal et al. 1996; Franchi et al. 1998; Busteros et al. 1998; Caminos, 1999; Remesal et al. 1999; Cucchi et al. 1999; De Ignacio et al. 2001; Remesal et al. 2004; Kay et al.

2007; Navarrete et al. 2020). No intervalo entre esses dois extremos bibliográficos, início e final do século XX, outros autores publicaram trabalhos reconhecendo, datando e corroborando novas unidades, como Flores, M.A. (1956); Flores, M.A. (1957); Nakayama, C. (1975); Corbella, H. e Linares, E. (1977).

Inicialmente, os derrames do platô basáltico de Somuncurá foram considerados, por Ardolino e Franchi (1993), como desenvolvidos entre 33 e 17 Ma. Segundo datações  $^{40}\text{K}/^{40}\text{Ar}$ , o principal evento é de idade Oligoceno, com dois picos principais de maior volume, o primeiro entre 33 e 31 Ma, e outro entre 27 e 25 Ma.

Posteriormente, após os derrames basálticos principais, durante o Mioceno, um importante sistema vulcânico alcalino se desenvolveu. As relações estratigráficas entre os complexos alcalinos e os depósitos de platô não foram definidas com clareza até o momento.

Os complexos alcalinos, (Kay et al. 2007) representam uma porção das manifestações efusivas desenvolvidas após o platô basáltico. Rochas vulcânicas mais silicáticas que estão temporal e espacialmente relacionadas às lavas máficas incluem tufos, riolíticas, traquíticas, comendíticas, e rochas intrusivas subvulcânicas. Sendo abundantes nas regiões das *Sierras de los Chacays, Telsen, Apas, Talagapa e Alta Sierra de Somuncura*, onde parecem estar associadas às grandes centros eruptivos (Navarrete et al. 2020). Esses formam, no geral, extensos sistemas vulcânicos poligenéticos amplamente distribuídos, sendo compostos por um conjunto de rochas básicas alcalinas subsaturadas e pequenas intrusões mais diferenciadas (Corbella, 1982).

Os complexos vulcânicos alcalinos, principalmente do Mioceno, são agrupados na Super Unidade *Quiñelaf*, de acordo com a proposta de Franchi et al. (1998). As datações  $^{40}\text{K}/^{40}\text{Ar}$  realizadas até o momento, indicam um intervalo de tempo, variando de  $37 \pm 2$  Ma a  $11 \pm 2$  Ma, evidenciando, assim, possíveis inconsistências estratigráficas. Em geral, as lavas intermediárias, como os andesitos, preenchem uma porção do Oligoceno (Ardolino, 1981; Franchi e Sepúlveda, 1983), enquanto as lavas básicas e subvulcânicas, além dos diques, são do Mioceno ( $23 \pm 2$  Ma e  $15 \pm 1$  Ma; Ardolino, 1981).

As efusões traquíticas mais recentes na *Sierra Negra de Telsen* e na *Sierra de los Chacays*, também apresentam idades do Mioceno ( $22 \pm 2$  Ma;  $19,3 \pm 3$  Ma e  $18 \pm 2$  Ma; Yllañez e Lema 1979; Barbieri e Corbella 1987). Por último, no Mioceno Médio, manifestações tardias com intrusões de corpos subvulcânicos traquíticos com

idade de  $12 \pm 1$  Ma e  $11 \pm 2$  Ma ocorrem na *Alta Sierra de Somuncurá* (Ardolino e Franchi, 1993).

A falta de dados sobre a evolução magmática da *Sierra de Apas* e as conexões entre as diferentes litologias mostra a necessidade de estudos detalhados desse corpo vulcânico.

## 1 OBJETIVOS

Reconhecer e interpretar a relação da Províncias Magmática de Somuncurá (PMSC), desenvolvida durante o Cenozoico, com a subdução andina, levando em consideração os derrames basálticos e, posteriormente, os magmas diferenciados de caráter traquítico e riolítico na *Sierra de Apas*.

Estabelecer, ao final das interpretações, a gênese e evolução das sucessões aflorantes no intuito de modelar a fusão da fonte, a mistura magmática e o processo de cristalização fracionada usando os métodos de Shaw (1979).

Para produzir tais conclusões, diferentes investigações são propostas, dentre elas, a identificação e caracterização das diferentes litofácies que integram a *Sierra de Apas*, petrografia, litogeоquímica e geocronologia, além disso, explicar o magmatismo bimodal que se desenvolveu na província do Oligoceno ao Mioceno.

## 2 GEOLOGIA

A geologia da Patagônia é complexa, marcada por uma variedade de processos geológicos distintos, gerando litologias variadas em um intervalo de tempo abrangente. Segundo Aradolino et al. (2008), os primeiros trabalhos reconhecidos na área com estudos geológicos são datados das primeiras décadas do século XX, investigadores como Windhausen (1918 e 1921) e Wichmann (1927), onde este último publicou o primeiro mapa da área na escala 1:500.000 (Figura 1), realizaram as primeiras observações sobre os principais lineamentos geológicos da região da *Sierra de Apas*, em busca de água e bens minerais.

Figura 1 - Mapa produzido por Wichmann (1927).



Legenda: Primeiro mapa produzido na escala 1:500.000 da Província Magmática de Somuncurá produzido por Wichmann em 1927.

Fonte: Pachá, G. (2022).

A evolução eruptiva da Província Magmática de Somuncurá (PMSC) foi marcada por distintas fases vulcânicas. Inicialmente, observou-se um vulcanismo

alcalino depletado em Nd-Sr, seguido por rochas maficas toleíticas (ca. 29 - 25 Ma). Posteriormente, ocorreu uma transição para rochas alcalinas (ca. 24 - 17 Ma), caracterizadas pela abundância de elementos incompatíveis e empobrecimento em Sr-Nd (Kay et al. 2007).

Segundo Kogarko (2021), o magmatismo alcalino, está relacionado com regiões estáveis da crosta, sendo controlado por riftes e zonas de afinamento crustal. As rochas alcalinas estão associadas a depósitos de metais raros como Nb, Ta, Zr, Sr, Ba, P, Al, elementos terras raras e radioativos. Desse modo, com o início da tectônica de placas, a subdução de crosta oceânica oxidada enriquecida em voláteis e do metassomatismo do manto, gerando um reservatório enriquecido como fonte do magmatismo alcalino.

Rochas alcalinas aparecem no final do Arqueano e não foram abundantes no Proterozóico, pequenos registros ocorrem no final do Proterozoico Médio, com picos de magmatismo alcalino em 550, 400 e 250 Ma, e principalmente entre 200 e 190 Ma, alcançando seu máximo no Eoceno. Kogarko (2021) justifica esse aumento sendo causado por um possível envolvimento gradual de horizontes do manto mais profundo no processo de convecção, aumentando a troca de material durante a reciclagem.

A Província Magmática de Somuncurá (PMSC) se desenvolveu sobre um embasamento composto de rochas ígneas e metamórficas, com idades do Pré-Cambriano até o Jurássico Inferior (Ardolino et al. 2008).

Segundo Ignacio (2001), o plateau de Somuncurá corresponde ao maior derrame basáltico da Argentina e um dos maiores do mundo, possuindo mais de 20.000 km<sup>2</sup>. Alguns autores, como Kay et al. (1992), e Tebbens & Cande (1997), sugerem que o magmatismo foi gerado por um *hotspot* transitório, causado pela reorganização das placas de Nazca - Farallon durante o Neógeno.

## 2.1 Hipóteses de formação da Patagônia

Diversos autores apresentaram propostas para a Patagônia ser um paleocontinente, dentre eles Windhausen (1921), que considerou o maciço patagônico como um continente Patagônico-Antártico. Nur e Ben Avraham (1977) e

Ben Avraham (1981) sugeriram que os fragmentos da América do Sul possuem origens diferentes.

Ramos (1984) propôs duas hipóteses: (1) a primeira considerando a margem Patagônica passiva e a margem do Gondwana ativa, no entanto acabou sendo dificultada pelos escassos registros magnéticos na margem do Gondwana. (2) A segunda hipótese, a margem Patagônica ativa e a do Gondwana passiva, reúne um número maior de evidências, sendo a Patagônia um continente à deriva até se colidir com o Gondwana.

O autor então sugere o setor Norte da Patagônia como sendo uma margem ativa, iniciada no Carbonífero, com desenvolvimento de arco magmático, formado por granitoides do Carbonífero, que evoluem de granodioritos a granitos de composição cálcio-alcalinas e metaluminosa, que gradam para rochas mais jovens peraluminosos. Essas rochas são geradas pela subdução da crosta oceânica da placa Gondwânica, tendo fim com a colisão no Permiano Superior ao Triássico. A colisão ocasionou um intenso magmatismo representado por rochas ácidas plutônicas e vulcânicas.

A zona de sutura pode ser interpretada através de anomalias gravimétricas, porém podem não mostrar necessariamente a zona de sutura, e sim, afinamento crustal e ascensão da astenosfera. Outra alternativa é utilizar complexos ultramáficos transversais, a oeste, no Chile, que foram mencionados por Alfaro et al. (1983). No entanto, a ausência de maiores evidências torna a sutura o principal problema para validação da Patagônia alóctone.

## 2.2 Embasamento pré-mesozoico

O embasamento paleozoico da PMSC , segundo Ardolino et al. (2008) é composto de rochas ígneas e metamórficas, do Pré-Cambriano até o Cretáceo, sendo a primeira pouco expostas, juntamente com intrusões do Paleozoico ao Jurássico. Vulcões triássicos, jurássicos e terciários cobrem amplamente as sucessões mais antigas (Gosen, 2003). O desenvolvimento e a tectônica geradora dessas rochas são motivos de discussões, interpretações e dúvidas.

O magmatismo paleozoico foi descrito por Nuñez et al. (1975), Ramos (1975) e Caminos e Llambias (1984), marcado como um intenso plutonismo orogênico, rochas tonalíticas e graníticas, associado a um intenso metamorfismo regional cuja idade remete ao Pré-Cambriano-Paleozoico Inferior. Os eventos magmáticos estão associados aos eventos deformacionais correspondentes ao Ciclo Famatiniano.

De acordo com Von Gosen (2003), o Maciço Patagônico Norte (MPN) foi afetado por eventos tectônicos compressivos dícteis e rúpteis. O primeiro estágio seria marcado por empurrões S-SW, durante o Proterozoico Superior ao Devoniano, combinado com a formação de milonitos e intrusão dos granodioritos Navarrete. Em um segundo estágio, marcado com compressão NW-SE, Devoniano ao Permiano, gerando dobras, falhas reversas e o pulso intrusivo final do Complexo de Navarrete.

As litologias, segundo Von Gosen (2003), que compõem a sequência paleozoica, têm início com a Orogenia Pampeana (Ediacarano - Cambriano), correspondendo à Formação *Complejo El Jaquélito*, sendo uma unidade metassedimentar composta de metapelitos e xistos que se desenvolveram em ambiente marinho amplamente espalhado nas porções centrais e nortes da Argentina, assim como nas costas das províncias argentinas de *Rio Negro* e *Chubut*.

Posteriormente, o Ciclo Famatiniano desenvolvido entre o Cambriano e Devoniano Superior, apresenta uma distribuição regional similar ao ciclo anterior na porção norte da Patagônia. Os registros mais antigos deste ciclo consistem de escassos granitos e granodioritos tipo I de idade Ordovíciana atribuídos ao Complexo Plutônico *Punta Sierra*. O Ciclo Famatiniano também está caracterizado por importantes sucessões sedimentares marinhas correspondentes à Formação *Sierra Grande*. Esta unidade, cujos principais afloramentos se localizam a 170 km da área de estudo, é portadora de níveis de ferro sedimentar e também foi interpretada sob a placa basáltica em trabalhos de interpretação e modelagem gravimétrica (Gosen, 2003).

Da mesma forma, o Ciclo Gondwânico constitui um dos ciclos mais extensos, sendo representado principalmente por granitos não foliados do tipo I e granitos foliados do tipo S. Ambos tipos de corpos ígneos se associam à Orogenia Gondwânica, a qual constitui uma das orogenias paleozoicas mais distribuídas na região patagônica, durante o período Permiano.

Após este ciclo, inicia-se no Triássico Superior, uma tectônica extensional que reativa falhas dos ciclos tectônicos anteriores causando o rifteamento e quebra do Gondwana.

A Tabela 1 sintetiza a evolução e os eventos tectônicos que afetaram o embasamento da PMSC.

Tabela 1 - Síntese dos eventos tectônicos ígneos e metamórficos Paleozoicos da PMSC.

Era	Período	Evento	Formação	Rocha
Mesozoico	Jurássico Inferior	Início do rifteamento	Formação Marifil	<i>Coulées</i> , brechas e tufos
	Triássico superior	Início da tectônica extensional		
Paleozoico	Permiano	Orogenia Gondwânica		Granito tipo I e S
	Carbonífero			
	Devoniano superior		Formação Sierra Grande	Sucessões sedimentares marinhas
	Siluriano			
	Ordoviciano	Ciclo Famatiniano	Complexo Plutônico Punta Sierra	Granitos tipo I e granodioritos
Neo- Proterozoico	Cambriano			
	Ediacarano	Orogenia Pampeana	Complexo El Jaquélito	Metapelitos e xistos

Legenda: Evolução do embasamento Paleozoico da PMCS.

Fonte: Pachá, G., 2022.

## 2.3 Embasamento mesozoico

No Jurássico Médio-Cretáceo Inferior, teve início o rifteamento governado por múltiplos e polifásicos episódios de deformação orogênica que afetou o extremo sul da América do Sul.

De acordo com Pavón Pivetta et al. (2020), o sistema deformacional do Gondwana que teve início no Triássico Superior, influenciou diretamente o vulcanismo Jurássico na região. A autora divide o magmatismo na região em dois estágios: (1) o primeiro estágio (V0) foi condicionado por falhas normais leste-oeste que conectaram a câmara magmática à superfície, com um típico vulcanismo Pliniano, tendo estruturas em *coulées* e litologias como brecha e *lapilli* tufo,

presentes em seis litofácies, numeradas de I a VI, tendo a litofácie II zircão datado em  $192,6 \pm 2,5$  Ma. (2) Posterior à erosão e discordância angular, segundo a mesma autora, as litofácies VII a X representam o segundo estágio (V1) (Pankhurst et al. 2000), relacionadas aos grandes centros eruptivos, com vulcanismo volumoso, de baixa viscosidade, anidro e com alta concentração de elementos do grupo dos halogênios, tendo como litologias ignimbrito de composição riolítica, *lapilli* tufo maciço e riolitos, semelhante ao vulcanismo do tipo *snake river*.

Sendo assim, a autora e seus colaboradores definiram o primeiro estágio (V0) relacionado à margem continental ativa e arco vulcânico, enquanto o segundo estágio (V1) tem relação com ambiente continental intraplaca com plumas mantélicas ou riftes continentais.

Inicialmente, efusões extensionais significativas, que prenunciaram a abertura do Oceano Atlântico, afetaram o embasamento e formaram uma região deprimida ou bacia intracontinental, nomeada como bacia de *Somuncurá Canadón Asfalto*.

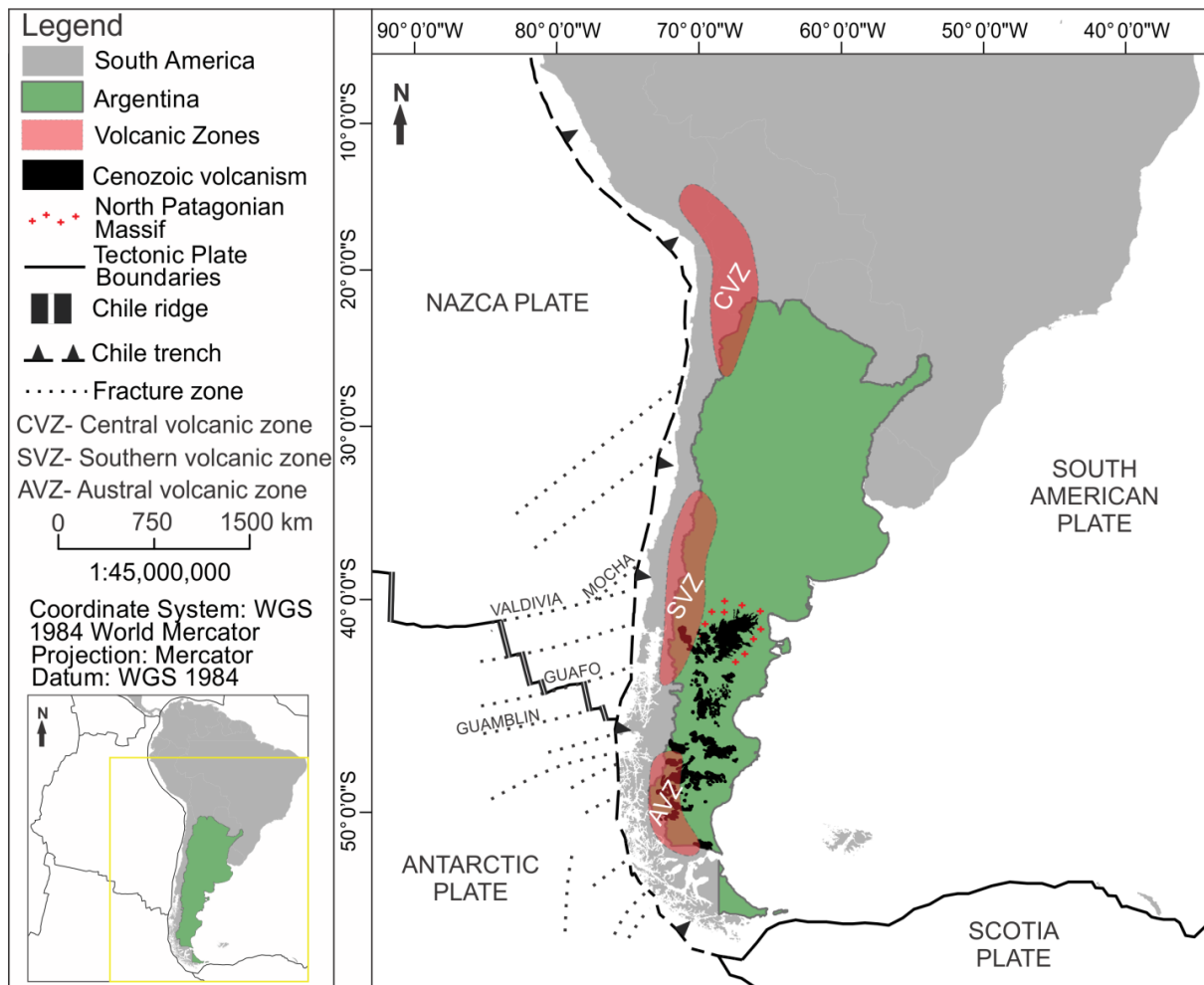
A bacia foi preenchida principalmente por rochas vulcânicas de distintas composições, entre o Triássico Superior até o Jurássico médio, e foram agrupadas em várias unidades como: Complexo Vulcânico *Los Menucos* e *Marifil*, a Formação *Garamilla* e o Grupo *Lonco Trapial* (Figari et al. 2005).

No Jurássico Superior, se instalou um ambiente lacustre e fluvial com acumulação de sedimentos intercalados com lavas basálticas, este conjunto é conhecido como Formação *Cañadón Asfalto* (Silva Nieto et al. 2003).

Segundo a coluna estratigráfica, o Cretáceo é marcado pelo Grupo *Chubut* constituído de sedimentos de origem fluvial com aporte de cinzas vulcânicas, contendo abundantes fósseis de dinossauros e troncos de árvores.

No Cretáceo Superior ocorreu uma mudança nas condições ambientais, à região foi inundada pelo mar, e no leito se acumularam sedimentos pelíticos que cobriram as rochas do Grupo *Chubut*, originando as Formações *La Colonia*, *Los Alamitos*, *Puntudo Chico* e *Coli Toro*, e outras de menor distribuição.

Figura 2 - Mapa esquemático com a localização dos principais magmatismos cenozoicos e as zonas magnáticas da Patagônia Argentina.



Legenda: Mapa representando as províncias magnáticas da patagônia argentina, as zonas vulcânicas e a zona de subducção na borda oeste da Placa Sul-Americana.

Fonte: Mapa modificado e adaptado de De Ignacio et al. (2000) e Navarrete et al. (2020).

## 2.4 Província Magmática de Somuncurá (PMSC)

A evolução da Província Magmática de Somuncurá (PMSC) é marcada por mudanças litológicas. A única evidência tectônica contemporânea, que pode ser associada à província, coincide com a quebra da placa de *Farallon*, que ao se colidir com a Placa Sul Americana no Paleógeno, causou, segundo Aragón et al. (2013), a abertura de uma janela na astenosfera, resultando em uma extensão e elevação do

*back-arc*, bem como a subida do manto, desenvolvendo-se, assim, o Platô Somuncurá.

Segundo Søager et al. (2021), o vulcanismo que ocorreu do final do Oligoceno ao início do Mioceno no norte da Patagônia, que desenvolveu a Província Magmática de Somuncurá, tem relação com uma anomalia térmica transitória e ascendência do manto quente do tipo EM1 (do inglês *Enriched Mantle*, e do português manto enriquecido 1), semelhante às composições encontradas nos basaltos do *Walvis Ridge* e *Etendeka*.

Os basaltos da Patagônia tiveram erupções de forma descontínua em um vulcanismo *back-arc* aproximadamente 450 km atrás da *Southern Volcanic Zone* (SVZ) ou da *Austral Volcanic Zone* (AVZ), do Eoceno até o Pleistoceno. Atualmente, a Placa de Nazca em subdução mergulha cerca de 30º E abaixo de SVZ e alcança uma profundidade de 200 km no *back-arc* a 38º S. Da mesma forma, na Placa Antártica, a subdução abaixo de AVZ pode ser rastreada a 200 km de profundidade no manto. Entre essas duas zonas, SVZ e AVZ, a dorsal do Chile está em subdução formando uma grande janela na região de 46 – 48º S (Figura 2).

O Paleógeno é marcado pela permanência do mar na região, cujos registros são os sedimentos de praia formados por grandes quantidades de organismos marinhos calcários, areias grossas e algumas argilas, dando origem aos estratos da Formação *Roca*.

Durante o Eoceno, a região da Província Magmática de Somuncurá sofreu sua última inundação, Formação *El Buitre*, sendo assim, todos os processos vulcânicos posteriores se desenvolveram sobre o continente em uma altitude próxima do nível do mar.

Já durante o Oligoceno e o Mioceno, um vulcanismo com acúmulos de espessas camadas de cinzas vulcânicas esbranquiçadas provenientes do vulcanismo andino, que são conhecidas como Formação *Sarmiento*, havendo, na região, mudanças ambientais marcadas pelo desenvolvimento de inúmeras espécies de mamíferos e depósitos de cinzas.

Simultaneamente com este vulcanismo se produziram extensos derrames de lava basáltica que lentamente se intercalam com as camadas de cinza, as quais foram totalmente cobertas pelas lavas basálticas. Essas lavas constituem a parte superior da *Meseta de Somuncurá*. A espessura do derrame basáltico é variável, onde nas bordas se encontram camadas de 20 a 30 metros.

Em regiões mais restritas ocorreram efusões traquíticas e riolíticas que atualmente constituem as zonas serranas, as áreas mais elevadas dentro na meseta.

Ao final do Neógeno, movimentos de ascensão elevaram boa parte da Patagônia, expondo à erosão grande parte da Bacia *Somuncurá Cañadón Asfalto*. As unidades e formações cobertas pelas rochas basálticas sofreram uma erosão lenta, produzindo um fenômeno chamado de inversão do relevo.

A tabela 2 apresenta de forma sintetizada o desenvolvimento da PMSC, ao longo do Cenozoico, através das descrições de Ardolino et al. (2008).

Tabela 2 - Síntese da formação da Província Magmática de Somuncurá (PMSC) e do embasamento Mesozoico.

Era	Péodo	Época	Formação	
Cenozoico	Neogeno	Mioceno	Superior Médio Inferior	Superunidade Quiñela
		Oligoceno	Superior	
			Médio	
	Paleogeno	Inferior	Grupo Sarmiento	
		Eoceneo	Médio	
		Paleoceno	Superior	
			Inferior	
			Fm. El Buitre	
			Fm. Roca	
	Mesozoico	Cretáceo	Superior	
		Médio		
		Inferior		
		Fm. La Colonia		
		Fm. Pundo Chico		
		Grupo Chubut		

Legenda: A tabela apresenta a evolução geológica da Província Magmática Somuncurá, as principais formações e a idade de formação das mesmas.

Fonte: Adaptado de Ardolino et al. (2008) e Pavón Pivetta et al. (2020).

Nos últimos anos, a Província Magmática de Somuncurá (PMSC) vem sendo estudada pontualmente, sendo realizadas campanhas de pesquisas em afloramentos e perfis específicos, ao passo que a área superficial da província corresponde a 55 mil km<sup>2</sup>, o que também dificulta a correlação de camadas e unidades, majoritariamente pela escassez de trabalhos na região, ocasionando na criação de unidades locais.

Kay et al. (2007), desenvolveram uma nomenclatura que subdivide a PMSC em três terminologias (Tabela 3): *Pré-Plateau*, *Plateau* e *Pós- Plateau*. Os autores consideram a Formação Somuncurá como sendo o *Plateau*, dessa forma todos os episódios anteriores ao basalto Somuncurá, ocorridos no Cenozoico, são considerados *Pré-Plateau*, enquanto que todos os eventos posteriores são considerados *Pós- Plateau*.

Tabela 3 - Divisão proposta por Kay et al. (2007) para classificar o magmatismo da Província Magmática de Somuncurá.

<b>Idade</b>	<b>Terminologia (Kay et al. 2007)</b>	<b>Unidade</b>	<b>Idade <math>^{40}\text{Ar}/^{39}\text{Ar}</math> em Ma (Kay et al. 2007)</b>
Mioceno Superior/ Médio	Pós – Plateau	Formação Quiñelaf	$16.6 \pm 0.4$ $20.6 \pm 0.63$
Mioceno Inferior Oligoceno Superior	Plateau	Formação Somuncurá	$26.9 \pm 0.78$
Oligoceno Inferior Eoceno	Pré – Plateau	Formação Sarmiento	$29.2 \pm 1.53$

Legenda: As idades foram obtidas por análise  $^{40}\text{Ar}/^{39}\text{Ar}$  em amostras coletadas em localidades distintas na PMSC, sendo subdivididas em três terminologias e representadas pelas formações características.

Fonte: Adaptado de Kay et al. (2007).

A *Sierra de Apas*, objeto de estudo neste trabalho, faz parte das efusões jovens intraplaca geradas durante o Paleógeno e o Neógeno que sobrepõem as rochas basálticas, no norte da Patagônia extrandina, sendo assim classificada como *Pós-Plateau* e com suas rochas pertencendo à Formação Quiñelaf, outras sierras também fazem parte desse conjunto: *Alta de Somuncurá*, *Chacays*, *Negra de Telsen* e *Talagapa* (Remesal et al. 2004).

De acordo com Remesal (1988), o segundo ciclo eruptivo, conhecido como *Pós-plateau*, exibe variedades petrográficas e relações estruturais menos complexas na região da *Alta Sierra de Somuncurá*. Por outro lado, as regiões de *Sierras de Apas*, *Chacays*, *Negra de Telsen* e *Talagapa* demonstram características mais evoluídas, apresentando rochas como basanitos, basaltos alcalinos, hawaiitos, mugearitos, benmoreitos traquitos, fonolitos e comenditos.

### 3 MATERIAIS E MÉTODOS

#### 3.1 Campo

No desenvolvimento deste projeto, um trabalho de campo foi realizado pelo orientador e pelo coorientador, Leonardo Benedini, em abril/maio de 2019.

No decorrer da expedição, procedeu-se à descrição de afloramento, bem como à captura de fotografias e coleta de amostras representativas. Esses elementos foram reunidos com o objetivo de classificar, interpretar e analisar os diferentes litotipos presentes na *Sierra de Apas*. Esse processo detalhado de documentação e coleta de dados é fundamental para uma compreensão abrangente da geologia da região.

A coleta dessas amostras durante a excursão proporcionou uma base sólida e direta para as análises subsequentes, contribuindo significativamente para a confiabilidade e representatividade dos dados utilizados no estudo, permitindo uma análise mais aprofundada das características e composição dos estratos rochosos na *Sierra de Apas*.

#### 3.2 Preparação de amostras

As amostras foram criteriosamente escolhidas com o intuito de caracterizar todas as litologias observadas em campo. Posteriormente, foram identificadas e preparadas no Laboratório Geológico de Processamento de Amostras (LGPA) da Universidade do Estado do Rio de Janeiro (UERJ).

O processo de preparação das amostras no laboratório seguiu padrões técnicos e científicos rigorosos, aderindo estritamente às normas laboratoriais estabelecidas. As diferentes etapas desse procedimento foram conduzidas com supervisão direta do autor e sob a orientação dos técnicos responsáveis, garantindo a integridade e qualidade dos resultados obtidos.

### 3.3 Petrografia

Foram preparadas sete lâminas petrográficas seguindo um processo detalhado. As etapas incluíram o corte da amostra e a colagem, seguida de cortes adicionais para atingir uma espessura mínima em relação ao vidro. Posteriormente, o polimento foi realizado utilizando a politriz de polimento múltiplo Arotec, visando alcançar uma espessura final de 30 nm.

Este procedimento garante que as lâminas sejam preparadas de forma consistente e atendam aos padrões necessários para análises petrográficas detalhadas e precisas.

### 3.4 Litogeocquímica

Além das lâminas petrográficas, quinze amostras foram submetidas ao processo de análise litogeocquímica de elementos maiores e traços em rocha total. Essas amostras foram trituradas na bigorna e, em seguida, processadas em um moinho de bolas de tungstênio, resultando em um pó fino. Posteriormente, as amostras foram enviadas para o laboratório *Australian Laboratory Services* (ALS)

Os elementos maiores,  $\text{SiO}_2$ ,  $\text{TiO}_2$ ,  $\text{Al}_2\text{O}_3$ ,  $\text{Fe}_2\text{O}_3^t$ ,  $\text{MnO}$ ,  $\text{MgO}$ ,  $\text{CaO}$ ,  $\text{Na}_2\text{O}$ ,  $\text{K}_2\text{O}$ ,  $\text{P}_2\text{O}_5$ , foram medidos como óxidos em porcentagem em peso (wt. %) utilizando o método *Inductively Coupled Plasma Atomic Emission Spectrometry* (ICP-AES), um método que utiliza ionização em altas temperaturas para excitar os elementos, permitindo assim identificar e quantificar.

Os elementos traços, Cr, V, Ba, Rb, Sr, Y, Nb, Zr, Hf, Ta, U, Th e os elementos terras raras, foram medidos em partes por milhão (ppm) através do método *Inductively Coupled Plasma Mass Spectrometry* (ICP- MS). Este método envolve a fusão da amostra com borato de lítio, permitindo a análise de um amplo conjunto de elementos. Esse processo analítico sofisticado proporciona uma compreensão abrangente da composição química das amostras, contribuindo para uma interpretação mais completa e precisa do contexto geológico estudado.

### 3.5 Microssonda

A química mineral foi determinada no Laboratório de difração de raios X e microssonda eletrônica (Labsonda) na Universidade Federal do Rio de Janeiro (UFRJ), Brasil, usando o equipamento JEOL JXA-8230, microssonda eletrônica de cinco espectrômetros. As análises por dispersão de comprimento de onda foram realizadas com uma tensão de aceleração de 15 kV e corrente de feixe de 20 nA para minerais silicatados, e 20 kV e 20 nA para minerais opacos.

### 3.6 Geocronologia

Simultaneamente, foram processadas três amostras para análise geocronológica. O processo começou com a limpeza das amostras, removendo qualquer vestígio visível de alteração. Em seguida, as amostras foram trituradas em um moinho de mandíbula e passadas por uma mesa hidráulica para separação dos minerais leves e pesados. As frações leves foram preservadas, enquanto as pesadas seguiram para a próxima etapa, passando por separação magnética com imã de mão e pelo separador magnético Frantz.

As porções não atraídas foram submetidas a líquidos densos, inicialmente usando bromofórmio, seguido pelo iodeto, para separação dos minerais mais densos. Após esses procedimentos, as amostras foram observadas sob lupa e microscópio eletrônico de varredura (MEV).

A etapa seguinte foi a preparação dos *mounts* no Multilab UERJ, e a análise MEV-EDS foi conduzida no Centro de Tecnologia Mineral (CETEM). Durante essa análise, foi constatada a presença de apatitas e raros zircões nas amostras, fornecendo informações essenciais para a análise geocronológica das mesmas.

Os dados U-Pb foram obtidos no Laboratório de Estudos Geodinâmicos, Geocronológicos e Ambientais da Universidade de Brasília, Brasil, nos cristais de apatita. As massas de interesse foram medidas num ICP-MS de alta resolução Thermo Fanning Element XT de campo setorial com múltiplos coletores acoplados a um sistema de ablação por laser Teledyne Analyte Excite de 193 nm. O sistema de

ablação por laser está equipado com uma câmara de duplo volume HelEx II. O espectrômetro de massa foi ajustado para melhorar a sensibilidade do U e do Pb, minimizando a produção de óxido antes de cada sessão analítica. Cada análise consistiu em 10 s de medição de ,seguidos de 30 s de aquisição de amostras. Cada massa ( $^{202}\text{Pb}$ ,  $^{204}\text{Pb}$ ,  $^{206-208}\text{Pb}$ ,  $^{232}\text{U}$ ,  $^{238}\text{U}$ ) foi medida simultaneamente utilizando uma combinação de detectores Faraday, SEM e CDD. As condições do laser incluíram um diâmetro de ponto de 65  $\mu\text{m}$ , 20 Hz e 7,5 J  $\text{cm}^{-2}$ . Os dados brutos foram processados no Iolite 4.0 (Paton et al. 2011) como sinal resolvido no tempo e a inspeção individual do sinal foi feita com a ajuda do VizualAge (Petrus e Kamber 2012). A redução dos dados foi realizada utilizando o UComPbine DRS, que tem em conta o avanço inicial variável no calibrador (Chew et al. 2014), e as correções incluíram a subtração do branco, a correção do fundo do furo utilizando um modelo exponencial mais linear e a normalização pela apatita Durango (Chew et al. 2011; McDowell et al. 2005). O avanço inicial usado para ancorar os dados foi de 0,835 (Chew et al. 2011). A apatita Sumé (Lana et al. 2022) foi utilizada para o controle de qualidade. O excesso de variação no calibrador primário foi propagado em cada ponto analítico. A incerteza sistemática de cerca de 1% é propagada em cada idade final. Não foi aplicada qualquer correção de chumbo comum. As idades são cotadas a 2s.

### 3.7 Isótopos

As composições isotópicas de Sr e Nd foram minuciosamente analisadas no Laboratório de Geocronologia e Isótopos Radiogênicos (LAGIR) da Universidade do Estado do Rio de Janeiro (UERJ). Para essa análise, sete amostras de rocha total em pó foram utilizadas, empregando o espectrômetro de massa de ionização térmica (TIMS) de multi-coletor TRITON.

As razões isotópicas foram normalizadas para  $^{146}\text{Nd}/^{144}\text{Nd} = 0.7219$ ;  $^{147}\text{Sm}/^{152}\text{Sm} = 0.5608$ ; e  $^{88}\text{Sr}/^{86}\text{Sr} = 8.3752$ . Durante o estudo, as análises dos materiais de referência padrão NBS-987 (NIST) ( $n = 140$ ) e JNd-1 ( $n = 214$ ; Tanaka et al. 2000) resultaram em médias de  $^{87}\text{Sr}/^{86}\text{Sr}$  de  $0.710239 \pm 0.000007$  ( $2\sigma$ ) e

$^{143}\text{Nd}/^{144}\text{Nd} = 0.512100 \pm 0.000006$  ( $2\sigma$ ; Valeriano et al. 2009; Neto et al. 2009). As razões isotópicas medidas foram normalizadas para a razão de  $^{86}\text{Sr}/^{88}\text{Sr} = 8.3752$ .

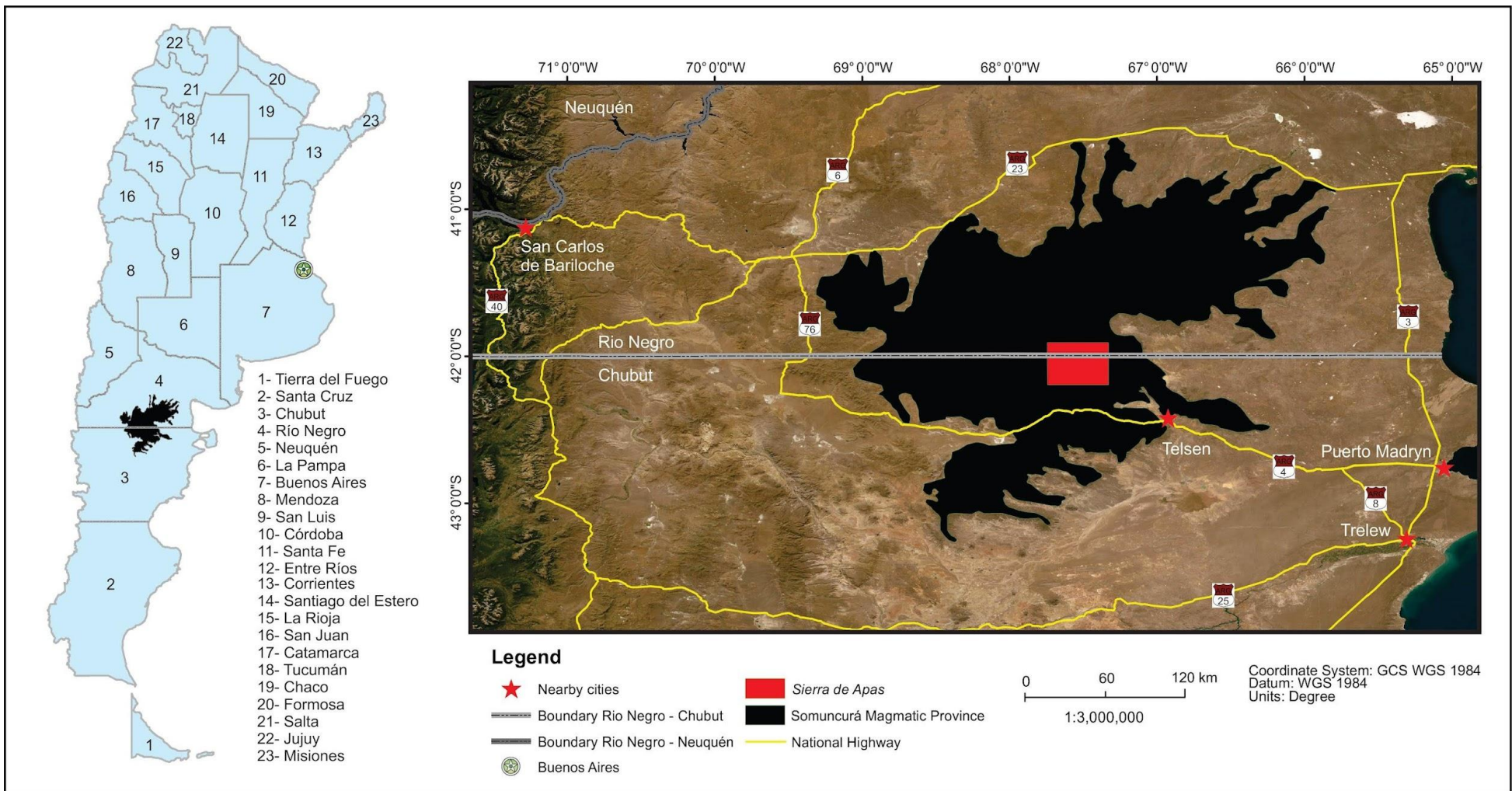
Análises repetidas do material de referência NBS-987 (NIST) resultaram em uma média de  $^{87}\text{Sr}/^{86}\text{Sr}$  de  $0.706012 \pm 0.000009$  ( $2\sigma$ ). Os brancos analíticos para Sm e Nd são inferiores a 70 pg e 200 pg, respectivamente, enquanto o valor de Sr não foi obtido. Essas medidas proporcionam uma base para a compreensão dos processos geológicos envolvidos.

## 4 LOCALIZAÇÃO

A Província Magmática de Somuncurá (PMSC) está localizada na parte central e sul da província de *Río Negro* - Argentina, estendendo-se até o centro-norte da província de *Chubut*. O derrame basáltico mais volumoso, que nomeia a província, recebe o nome de Formação Somuncurá (Ardolino et al. 2008) localizado entre 40°30' - 43°20'S e 65°50'- 69°20'W (Figura 3).

As vias de acesso na região da *Sierra de Apas* são escassas, sendo constituída majoritariamente por vias não pavimentadas. A vila de *Telsen* é a comunidade mais próxima da área de estudo, distante cerca de 60 km. As cidades mais próximas de *Telsen* são *Puerto Madryn* que dista 170 km e *Trelew* a 180 km, aproximadamente 4 horas de carro. A Rota Provincial 4 (RP4) liga *Telsen* com *Puerto Madryn*, e a RP4 juntamente com a Rota Provincial 8 (RP8) com *Trelew*. Ambas cidades se conectam com o restante do país pela Rota Nacional 3 (RN3), outras rodovias importantes, (Figura 1), como a Rota Nacional 6 (RN6), Rota Nacional 40 (RN40), Rota Provincial 23 (RP23) e Rota Provincial 25 (RP25) percorrem as Províncias de *Chubut* e *Rio Negro* próximas a Província Magmática de Somuncurá.

Figura 3 - Mapa de localização da Província Magmática de Somuncurá, *Sierra de Apas*, estradas e cidades.

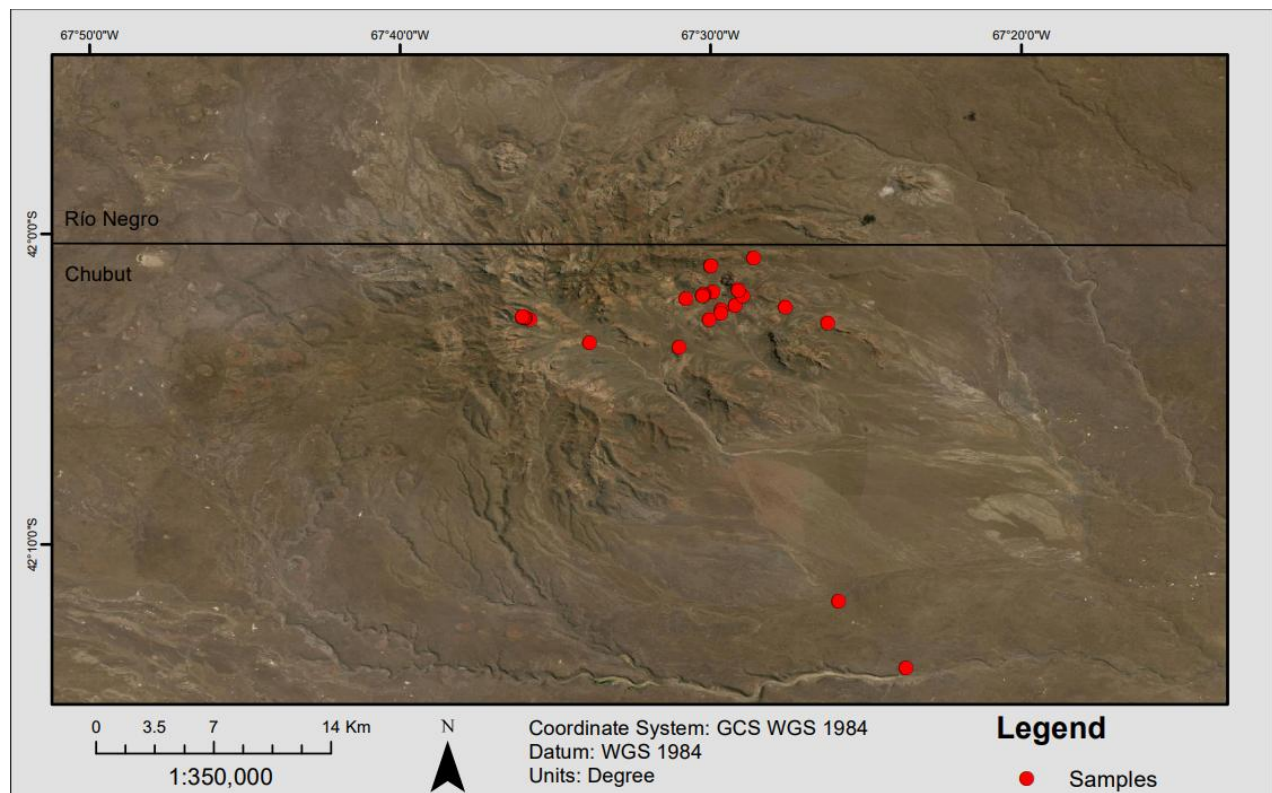


Legenda: Mapa destacando a Província Magmática de Somuncurá (destacada em preto), onde se encontra a *Sierra de Apas*, Argentina (destacada em vermelho e ampliada na Figura 2, as principais vias de acesso em amarelo e as cidades próximas.

Fonte: O autor.

A *Sierra de Apas*, área de estudo no presente trabalho, localiza-se no limite da Província de *Río Negro* e *Chubut*, Argentina entre os paralelos  $41^{\circ}55'$  e  $42^{\circ}15'$  de latitude Sul,  $67^{\circ}45'$  e  $67^{\circ}20'$  de longitude Oeste, com aproximadamente  $1.500\text{ km}^2$  (extensão máxima de 40 km no sentido Norte-Sul e 35 km no sentido Leste-Oeste; Figura 4), região na qual foram coletadas as amostras utilizadas neste trabalho. O Anexo A apresenta um mapa em detalhe dos pontos e amostras.

Figura 4 - Imagem de satélite da *Sierra de Apas* e a localização das amostras utilizadas.



Legenda: Imagem de satélite da *Sierra de Apas*, Argentina e as amostras estudadas no trabalho.  
Fonte: O autor.

## 5 RESULTADOS - Artigo

Os resultados do trabalho envolvem diferentes métodos de investigação, como a estratigrafia, petrografia, litogegeoquímica, isótopos e geocronologia. Os mesmos serão apresentados na forma de uma dissertação artigo, ao passo que ao final do mestrado um artigo precisa ser submetido.

O primeiro artigo foi submetido em junho de 2024 para o Jounal of South America Earth Sciences., em um sessão focada na Patagônia. O periódico é classificado como A2 na última atualização da Qualis CAPES.

O segundo artigo foi submetido no *Journal of Petrology*, um periódico acadêmico mensal, publicado pela Oxford University Press, focado no campo de petrologia ígnea e metamórfica e petrogênese. O periódico é classificado como A1 na última atualização da Qualis CAPES.

### ANEXO A

#### **Artigo 1 - *Upper Oligocene Sierra de Apas Caldera volcanism, Northpatagonian Massif, Argentina***

Gilmar Pachá Corrêa dos Santos da Silva, Leonardo Benedini, Anderson Costa dos Santos, Mauro Geraldes, Daniel A. Gregori, Guilherme Gonçalves, Tiago Jalowitzki

### ANEXO B

#### **Artigo 2 - *Sierra de Apas volcanic successions analysis and the relation with the evolution of the Somuncurá Magmatic Province, Argentina***

Gilmar Pachá Corrêa dos Santos da Silva, Anderson Costa dos Santos, Leonardo Benedini, Cecília Pavón Pivetta, Daniel Gregori, Julio Mendes, Claudio de Morisson Valeriano, Mauro Geraldes, Guilherme Gonçalves, Tiago Jalowitzki

## 6 CONCLUSÃO

A evolução magmática da Sierra de Apas, situada na Província Magmática de Somuncura, revela uma história vulcânica complexa que abrange desde fases pré-colapso até pós-colapso. Este estudo identificou uma vasta gama de litologias, desde basaltos até riolitos altamente evoluídos, e caracterizou onze litofácies distribuídas em cinco unidades principais. Esses achados refletem um sistema dinâmico moldado por uma variedade de composições magmáticas e estilos de erupção distintos.

A diversidade mineralógica e os diagramas ternários indicam um ambiente dinâmico na câmara magmática, onde a cristalização fracionada e a mistura de magma desempenham papéis cruciais. As composições minerais híbridas observadas em diferentes tipos de rochas sugerem injeções frequentes de magma em uma câmara em evolução, corroborando a hipótese de mistura de magma.

A análise litogeocímica destaca a evolução dos magmas alcalinos, que têm origem em fontes ultrabásicas basaníticas e são modificados principalmente pela cristalização fracionada sob condições variáveis de pressão e temperatura. As distintas características compostionais, como altos teores de sílica, zircônio e elementos terras raras, indicam a influência da subdução andina e o papel dos fluidos supercríticos ricos em solutos na mobilização de elementos de alta força de campo.

As evidências isotópicas na Província Magmática de Somuncura, com foco na Sierra de Apas, revelam um sistema magmático influenciado tanto pela atividade de pluma do manto quanto por processos relacionados à subdução. As assinaturas isotópicas variadas, incluindo índices radiogênicos de Nd e razões variáveis de Sr, apontam para uma origem multi-fontes, com contribuições de uma pluma do manto empobrecida, manto litosférico enriquecido e crosta continental. Estes resultados estão alinhados com o ambiente geodinâmico complexo da região, onde o magmatismo intraplaca é modificado por processos crustais associados à subdução andina.

Em resumo, esta pesquisa fornece conhecimentos fundamentais sobre os processos magmáticos da Sierra de Apas, enriquecendo a compreensão da atividade vulcânica Oligoceno-Mioceno na região. Ela estabelece uma base sólida

para futuros estudos e correlações com sistemas vulcânicos adjacentes, avançando significativamente o entendimento da história vulcânica e tectônica da área.

## REFERÊNCIAS

- ALFARO, G., FRUTOS, J., COLLAO. S., HELLE, S., 1983. Los sulfurus masivos de la Cadena Andina paleozoica en la Cordillera de la Costa, sur de Chile. 11°Congr. Nac. Geol. Econ. Actas 11: 337-360, San Juan.
- AMEGHINO FLORENTINO, 1898. Sinopsis geológico-paleontológica de la Argentina. "Segundo Censo de la República Argentina" (mayo 10 de 1895), t. I, Territorio. Buenos Aires.
- ARAGÓN, E., PINOTTI, L., D'ERAMO, F., CASTRO, A., RABBIA, O., CONIGLIO, J., DEMARTIS, M., HERNANDO, I., CAVAROZZI, C.E., AGUILERA, Y.E., 2013. The Farallon-Aluk ridge collision with South America: Implications for the geochemical changes of slab window magmas from fore- to back-arc. *Geosci. Front.* 4, 377–388.
- ARDOLINO, A.A., 1981. El volcanismo cenozoico del borde suroriental de la meseta de Somuncurá. Provincia del Chubut. 8°Congreso Geológico Argentino. Actas 1:65 y3:7-23.
- ARDOLINO A.A. Y FRANCHI, M.R, 1993. El volcanismo cenozoico de la Meseta de Somún Cura Provincias de Río Negro y Chubut. 12° Congreso Geológico Argentino y 2° Congreso de Exploración de Hidrocarburos, Actas 4:225-235.
- ARDOLINO, A. A., FRANCHI, M., REMESAL, M. B., & SALANI, F. M., 2008. La Meseta de Somún Curá: los sonidos de la piedra.
- BARBIERI, M. Y CORBELLA, H., 1987. Relaciones  $^{87}\text{Sr}/^{86}\text{Sr}$  de las rocas alcalinas de la sierra de los Chacays y edad de las volcanitas potásicas del cerro Planluán, Patagonia Extrandina, Chubut, Argentina. 10° Congreso Geológico Argentino, Actas 4:186-187.
- BEN-AVRAHAM, Z. V. I. et al. 1981. Continental accretion: from oceanic plateaus to allochthonous terranes. *Science*, v. 213, n. 4503, p. 47-54.

BUSTEROS, A., GIACOSA, R. Y LEMA, H., 1998. Hoja geológica 4166- IV, Sierra Grande, provincia de Río Negro. Instituto de Geología y Recursos Minerales. Boletín 241:I-75.

LLAMBÍAS, E.J., CAMINOS, R. RAPELA, C.W., 1984. Las plutonitas y vulcanitas del ciclo eruptivo Gondwánico. In: Ramos,V.A. (Ed.), Geología y recursos naturales de la provincia de Río Negro, 9 Congreso Geológico Argentino (Bariloche), Relatorio, Buenos Aires, p. 85–118

CAMINOS, R., 1999. Hoja geológica 4166- 1, Valcheta, provincia de Río Negro. Instituto de Geología y Recursos Minerales, inédito.

CHEW, D. M., SYLVESTER, P. J., & TUBRETT, M. N., 2011. U–Pb and Th–Pb dating of apatite by LA-ICPMS. *Chemical Geology*, 280(1-2), 200-216.

CHEW, D. M., PETRUS, J. A., & KAMBER, B. S, 2014. U–Pb LA–ICPMS dating using accessory mineral standards with variable common Pb. *Chemical Geology*, 363, 185-199.

CORBELLA, H., & LINARES, E., 1977. Acerca de la naturaleza peralcalina y la edad de algunos afloramientos volcánicos de la Sierra de Apas y de la Sierra Negra de Telsen, Macizo o Nordpatagónico, provincias de Río Negro y Chubut, Argentina. Revista de la Asociación Geológica Argentina, 32(2), 152.

CORBELLA, H., 1982. Naturaleza litológica del complejo alcalino sierra de Queupuniyeu, Patagonia Extraandina norte, Argentina. V Congreso Latinoamericano de Geología, Actas II, 197-211. Buenos Aires.

CORDENONS, P. D., 2017. *Geología y petrología del Complejo Volcánico Sierra de los Chacays, Provincia de Chubut, Patagonia extraandina* (Doctoral dissertation, Universidad de Buenos Aires. Facultad de Ciencias Exactas y Naturales).

CUCCHI, R., BUSTEROS, A. Y LEMA, H., 1999. Hoja geológica 4169- II, Los Menucos, provincia de Río Negro. Instituto de Geología y Recursos Minerales, inédito.

- DE IGNACIO, C., LÓPEZ, I., OYARZUN, R., & MÁRQUEZ, A., 2001. The northern Patagonia Somuncura plateau basalts: a product of slab- induced, shallow asthenospheric upwelling?. *Terra Nova*, 13(2), 117-121.
- DOERING, A., 1882. Informe oficial de la Comisión científica agregada al Estado Mayor General de la expedición al Río Negro. Entrega, 3, 401-430.
- FIGARI, E.G., 2005. Evolución Tectónica de la Cuenca de Cañadón Asfalto. Tesis Doctoral 3896, Facultad de Ciencias Exactas y Naturales, Universidad Nacional de Buenos Aires. Biblioteca Digital FCEN-UBA, 198 pp.
- FLORES, M. A., 1956. Perfiles en el Chubutiano y observaciones geológicas en parte central y norte de Chubut. YPF, Informe inédito, Buenos Aires.
- FLORES, M. A., 1957. Perfiles En El Chubutiano (II Parte). YPF, Informe Inédito, Buenos Aires.
- FRANCHI, M. R., & SEPÚLVEDA, E. G., 1983. Descripción geológica de la hoja 41h Cona Niyeu, provincia de Río Negro. Servicio Geológico Nacional., Informe inédito. Buenos Aires.
- FRANCHI, M., REMESAL, M. Y ARDOLINO, A., 1998. Hoja geológica 4166- III, Cona Niyeu, provincia de Río Negro. Instituto de Geología y Recursos Minerales, inédito.
- Herron, E. and Heitzler, J., 1967. Sea-floor spreading near the Galapagos. *Science*, 158: 775-780.
- KAY, S.M., ARDOLINO, A.A., FRANCHI, M.R., RAMOS, V.A., 1992. The Somuncura Platean: An Oligo-Miocene «Baby-Hotspot» in Extra-Andean Patagonia. American Geophysical Unión, Spring meeting. Abstracts.
- KAY, S. M., ARDOLINO, A.A., FRANCHI, M.R., RAMOS, V.A., 1993. El origen de la Meseta de Somun Cura: distribución y geoquímica de sus rocas volcánicas mañas. 12º Congreso Geológico Argentino y 2º Congreso de Exploración de Hidrocarburos, Actas: 4: 236-248.
- KAY, S. M., ARDOLINO, A. A., GORRING, M. L., AND RAMOS, V. A., 2007. The Somuncurá Large Igneous Province in Patagonia: interaction of a transient mantle thermal anomaly with a subducting slab. *Journal of Petrology*, 48, 1, 43-77.

KOGARKO, L. N., 2021. Enriched Mantle Reservoirs as a Source of the Largest Apatite and Rare-Metal Deposits. In: Alkaline Rocks, Kimberlites and Carbonatites: Geochemistry and Genesis. Springer, Cham. p. 1-14.

LANA, C., GONÇALVES, G. O., MAZOZ, A., BUICK, I., KAMO, S., SCHOLZ, R., WANG, H., MOREIRA, H., BABINSKI, M., & QUEIROGA, G., 2022. Assessing the U-Pb, Sm-Nd and Sr-Sr Isotopic Compositions of the Sumé Apatite as a Reference Material for LA-ICP-MS Analysis. *Geostandards and Geoanalytical Research*, 46(1), 71-95.

MAGNI, V., 2019. The effects of back-arc spreading on arc magmatism. *Earth and Planetary Science Letters*, 519, 141-151.

MCDOWELL, F. W., MCINTOSH, W. C., & FARLEY, K. A., 2005. A precise 40Ar–39Ar reference age for the Durango apatite (U–Th)/He and fission-track dating standard. *Chemical Geology*, 214(3-4), 249-263.

NAKAYAMA, C., 1975. Informe geológico preliminar del área que comprende sierra de los Chacays, cañadón Trapaulco, cerro Ponte y parte del curso inferior del arroyo perdido. YPF inédito. Buenos Aires.

NAVARRETE, C., GIANNI, G., MASSAFERRO, G & BUTLER, K., 2020. The fate of the Farallon slab beneath Patagonia and its links to Cenozoic intraplate magmatism, marine transgressions and topographic uplift. *Earth-Science Reviews*, 210, 103379.

NETO, C.C.A., VALERIANO, C.M., VAZ, G.S., MEDEIROS, S.R, RAGATKY, C.D., 2009. Composição Isotópica do Sr no padrão NBS987 e nos padrões de rocha do USGS BCR-1, AGV-1, G-2 e GSP-1: Resultados Preliminares Obtidos por TIMS no Laboratório de Geocronologia e Isótopos Radiogênicos – LAGIR – UERJ, RIO DE JANEIRO. In: Boletim de Resumos Expandidos do Simpósio 45 Anos de Geocronologia no Brasil, IGc-USP, CPGeo –Centro de Pesquisas Geocronológicas, CD-ROM.

NUÑEZ, E.; E. W. BACHMANN; I. RAVAZZOLI; A. BRITOS; M. FRANCHI; A. LIZUAIN y E. SEPULVEDA., 1975. Rasgos geológicos del sector oriental del Macizo de Somuncurá, provincia de Rio Negro, República Argentina. II Congr. Iberoamericano de Geología Económica IV: 247-266.

- NUR, AMOS; BEN-AVRAHAM, Z. V. I., 1977. Lost Pacifica continent. *Nature*, v. 270, n. 5632, p. 41-43.
- Pankhurst, R. J., Riley, T. R., Fanning, C. M., & Kelley, S. P., 2000. Episodic silicic volcanism in Patagonia and the Antarctic Peninsula: chronology of magmatism associated with the break-up of Gondwana. *Journal of Petrology*, 41(5), 605-625.
- PATON, C., HELLSTROM, J., PAUL, B., WOODHEAD, J., HERGT, J., 2011. Iolite: freeware for the visualisation and processing of mass spectrometric data. *J. Anal. At. Spectrom.* 26, 2508–2518
- PAVÓN PIVETTA, C., GREGORI, D., BENEDINI, L., GARRIDO, M., STRAZZERE, L., GERALDES, M., DOS SANTOS, A. C., & MARCOS, P., 2020. Contrasting tectonic settings in Northern Chon Aike Igneous Province of Patagonia: subduction and mantle plume-related volcanism in the Marifil formation. *International Geology Review*, 62(15), 1904-1930.
- PEARCE, J. A., & STERN, R. J., 2006. Origin of back-arc basin magmas: Trace element and isotope perspectives. *Back-arc spreading systems: Geological, biological, chemical, and physical interactions*, 166, 63-86.
- PETRUS, J. A., & KAMBER, B. S., 2012. VizualAge: A novel approach to laser ablation ICP- MS U- Pb geochronology data reduction. *Geostandards and Geoanalytical Research*, 36(3), 247-270.
- RAMOS, V. A., 1975. Geología del sector oriental del macizo Nordpatagónico entre Aguada Capitán y la Mina Gonzalito, provincia de Río Negro. *Revista de la Asociación Geológica Argentina* 30(3): 274-285.
- RAMOS, V. A., 1984. Patagonia: un continente paleozoico a la deriva?. In: 9º Congreso Geológico Argentino, SC Bariloche, Buenos Aires, 1984. p. 311-325.
- REMESAL, M. B., 1988. *Geología y petrología de los basaltos de la meseta de Somuncurá* (Doctoral dissertation, Universidad de Buenos Aires. Facultad de Ciencias Exactas y Naturales).

- REMESAL, M., GAGLIARDO, M., Y MÉNDEZ, M.J., 1996. Estructura, petrografía y geoquímica de las coladas basálticas en el límite noreste de la meseta de Somuncura. 12° Congreso Geológico Boliviano, Actas 2:473-482.
- REMESAL, M., SALANI, F., FRANCHI, M. Y ARDOLINO, A., 1999. Hoja geológica 4169-IV, Maquinchao, provincia de Río Negro. Instituto de Geología y Recursos Minerales, inédito.
- REMESAL, M., SALANI, F. M., MASSAFERRO, G. I., & CERREDO, M. E., 2004. Stratigraphy and petrology of the Northeastern sector of Sierra de Apas. Chubut Province. Revista de la Asociación Geológica Argentina, 59(4), 578-590.
- SHAW, D. M., 1979. Trace element melting models. Physics and Chemistry of the Earth, 11, 577-586.
- SILVA NIETO, D.; CABALERI, N. & SALANI, F., 2003. Estratigrafía de la Formación Cañadón Asfalto (Jurásico Superior), provincia del Chubut, Argentina. Ameghiniana, Vol 40 :p. 46R.
- SØAGER, N., HOLM, P. M., MASSAFERRO, G. I., HALLER, M., & TRAUN, M. K., 2021. The Patagonian intraplate basalts: A reflection of the South Atlantic convection cell. Gondwana Research, 91, 40-57.
- TANAKA, T., TOGASHI, S., KAMIOCA, H., AMAKAWA, H., KAGAMI, H., HAMAMOTO, T., YUHARA, M., ORIHASHI, Y., YONEDA, S., SHIMIZU, H., KUNIMARU, T., TAKAHASHI, K., YANAGI, T., NAKANO, T., FUJIMAKI, H., SHINJO, R., ASAHIARA, Y., TANIMIZU, M., DRAGUSANU C., 2000. JNd-1: a neodymium isotopic reference in consistency with LaJolla neodymium. *Chemical Geology*, v. 168, p. 279–281.
- TEBBENS, S.F., CANDE, S.C., KOVACS, L., PARRA, J. C., LABRECQUE, J. L., & VERGARA, H., 1997. The Chile ridge: A tectonic framework. *Journal of Geophysical Research: Solid Earth*, 102(B6), 12035-12059.
- VALERIANO, C.M., MEDEIROS, S.R., VAZ, G.S., NETO, C.C.A., 2009. Sm-Nd isotope dilution TIMS analyses of BCR-1, AGV-1 and G-2 USGS rock reference materials: first results from the LAGIR laboratory at UERJ, Rio de Janeiro. In:

Boletim de Resumos Expandidos do Simpósio 45 Anos de Geocronologia no Brasil, IGc-USP, CPGeo –Centro de Pesquisas Geocronológicas, CD-ROM.

VON GOSEN, W., 2003. Thrust tectonics in the North Patagonian Massif (Argentina): implications for a Patagonia plate. *Tectonics*, v. 22, n. 1.

WICHMANN, R., 1927. Resultados de un viaje de estudios geológicos en los territorios del Río Negro y del Chubut. Ministerio de Agricultura. Dirección General de Minas, Geología e Hidrología.

WINDHAUSEN, A., 1918. The problem of the Cretaceous-Tertiary boundary in South America and stratigraphic position of the San Jorge Formation in Patagonia. *American Journal of Science*, 4(265), 1-53.

WINDHAUSEN, A., 1921. Ein Blick auf Schichtenfolge und Gebirgsbau im südlichen Patagonien. *Geologische Rundschau*, 12(3), 109-137.

YLLAÑEZ Y LEMA., 1979. Estructuras anulares y geología del noroeste de Telsen (provincia del Chubut). 7º Congreso Geológico Argentino. Actas 1:445-454.

## APÊNDICE A – Artigo 1

### ***Upper Oligocene Sierra de Apas Caldera volcanism, North Patagonian Region, Argentina***

Gilmar Pachá Corrêa dos Santos da Silva<sup>a</sup>, Leonardo Benedini<sup>b,c</sup>, Anderson Costa dos Santos<sup>a,d</sup>, Mauro Geraldes<sup>a</sup>, Daniel A. Gregori<sup>b,c</sup>, Guilherme O. Gonçalves<sup>e</sup>, Tiago Jalowitzki<sup>e</sup>

<sup>a</sup>Universidade do Estado do Rio de Janeiro (UERJ), Faculdade de Geologia, Departamento de Mineralogia e Petrologia Ígnea, Rio de Janeiro, Brazil.

<sup>b</sup>Dpto. de Geología, Universidad Nacional del Sur (UNS), Bahía Blanca, Argentina

<sup>c</sup>Instituto Geológico del Sur (INGEOSUR), Universidad Nacional del Sur (UNS)-CONICET, Bahía Blanca, Argentina

<sup>d</sup>Tektos Group, UERJ - Brazil/GeoBioTec Group, Aveiro University - Portugal. ORCID: 0000-0003-2526-8620.

<sup>e</sup>Universidade de Brasília, Instituto de Geociências, Programa de Pós-Graduação em Geologia, Brasília, Distrito Federal, Brazil,

#### **Abstract**

The *Sierra de Apas* Caldera constitutes a trachytic volcano underlain by a high-level magma chamber, represented by the frequent participation of gabbros in the volcano stratigraphy. The volcanic activity started shortly before the latter Oligocene, with a low-angle trachyte lava shield growing over widespread basaltic lava belonging to the *Somuncurá* Formation. Internal Upper Oligocene collapse formed a 90 km<sup>2</sup> caldera. The eruption of ash-flow tuffs generated an important amphitheater structure at the SE caldera flank. During the collapse stage, a considerable amount of magma erupted, primarily as lava flows covering the caldera floor, and consolidating the caldera rim. The new U-Pb geochronological data from the post-caldera episode that both principal magmatic events (*Somuncurá* Formation and *Quiñelaf* Complex) were developed during a polygenetic Upper Oligocene short-term magmatic episode.

**Keywords:** Sierra de Apas; Volcanic Stratigraphy; North Patagonian Region; Oligocene magmatism; Alkaline magmatism

## 1 Introduction

The Upper Paleogene to Lower Neogene intraplate magmatism in the northern region of Patagonia stands out as one of the most significant accumulations of mafic lavas in southern South America (Navarrete et al. 2019). This magmatic activity was characterized by extensive basaltic plateaus, including the *Somuncurá* Large Igneous Province (Kay et al. 2007) and a series of polygenetic and bimodal volcanic complexes (Cordenons et al. 2020). Diverse tectonic origins have been proposed to explain the origin of this intraplate magmatism, supported by geochemical, isotopic, and geophysical modeling (e.g., Espinoza et al. 2005; Aragon et al. 2013; Ramos and Kay, 1992; Gorring et al. 1997; Gianni et al. 2018; Navarrete et al. 2019). However, despite regional studies, significant uncertainties persist regarding the temporal constraints and stratigraphic evolution.

The *Sierra de Apas* Volcanic Complex (Franchi et al. 2001) constitutes one of the most significant volcanic structures associated with this magmatic activity in the North Patagonian Region. Our current study aims to advance our understanding of the temporal and stratigraphic constraints that governed the growth and evolution of this individual polygenetic and bimodal volcanic structure. The temporal and stratigraphic features of these volcanic structures are also essential for understanding the tectonic evolution of the region, providing insights into the processes that drive the formation of the bimodal volcanic rocks within a single volcanic province.

This contribution presents a novel volcanic model and evolutionary framework that complements previous work by Ardolino (1981), Remesal et al. (2004), Franchi et al. (2001), and Salani et al. (2022). Based on recent observations, we provide detailed descriptions and interpretations of lithofacies. New U-Pb ages obtained from apatite have also been conducted to establish a precise age for the *Sierra de Apas* Volcanic Complex (Fig. 1a), further enhancing the stratigraphic characterization.

## 2 Tectonic setting during the Paleogene to Neogene transition

The *Somuncurá* Large Igneous province extends across the northern portion of Patagonia, between 40° and 43°S, covering an area of over 20,000 km<sup>2</sup> (Fig. 1; Corbella, 1984; De Ignacio et al. 2001). The region experienced two distinct magmatic events during the Oligocene and Miocene periods (Ardolino, 1981; Orgeira

and Remesal, 1993). The Somuncurá Formation comprised the massive basaltic effusions of the first event, whereas *Quiñelaf* Superunit (Franchi et al. 2001) represents the subsequent episodic trachytic and alkaline magmatic event. Several mechanisms have been proposed to explain the formation of the *Somuncurá* Plateau, including rifting processes with or without lithospheric thinning, plume activity, slab-window phenomena, and an asthenospheric (OIB-like) corner effect, which could have produced a transient thermal anomaly above the subducting plate (Kay et al. 2007). The first consists of massive basaltic effusions, included in the Somuncurá Formation, whereas the subsequent event involved trachytic and alkaline volcanic episodes, recorded in the *Quiñelaf* Superunit (Franchi et al. 2001).

In the North Andean Patagonian and extra-Andean areas, a Late Oligocene to Early Miocene extensional subduction characterizes the geodynamic scenario of the entire north Patagonian continental lithosphere (Folguera and Ramos, 2002; Giacosa et al. 2005; Aragón et al. 2013; Orts et al. 2015). These subduction processes promote intense inner crust stretching linked to widespread continental magmatism during this interval (De Ignacio et al. 2001). Notably, the extensional event separates two contractional periods associated with the Middle Cretaceous and Late Miocene phases (Orts et al. 2015; Gianni et al. 2018). The last contractional stage coexists with an eastward foreland expansion of the late Miocene magmatic arc, whose roots are presently exposed as minor granitic stocks and volcanic piles subordinate to the main Andes, east of the present arc. As a consequence of this orogenic stage, a foreland basin has developed, having progressed from 18 Ma in the North Andean Patagonian, the base of the *Nirihuau* Formation, to 11 Ma in the foreland area (Santonja et al. 2021).

The cannibalization of the foreland basin occurred initially in the hinterland and then progressed to the foreland zone. Blind structures formed a broken foreland at the frontal zone inferred from growth strata geometries (Santonja et al. 2021). During the Pliocene to Quaternary times, most of the contractional deformation was dissipated in the orogenic wedge when the arc front retracted to its present position. Early to mid-Tertiary igneous activity in the Cordilleran Series (CS) of the Andean Patagonian between 40°-42° 30' S shows spatial variation and temporal trends that can be correlated with crustal thickness and slab depth (Orts et al. 2015).

Arc volcanism is concentrated in two subparallel belts, the *Pilcaniyeu* Belt to the east and the *El Maitén* Belt to the west (Iannelli et al. 2018, 2020; Litvak et al. 2018;

Butler et al. 2020 and references therein). Compilation of available U-Pb, K-Ar, and paleogeographic data suggest three significant periods of volcanic activity. The first is a Paleocene-Eocene (60-42 Ma) event that developed primarily in the *Pilcaniyeu* Belt; the second (Oligocene, 33-23 Ma) event is now exposed mainly along the *El Maitén* Belt (Salani et al. 2022). Finally, the Miocene volcanism occurs in the northern sector of the *El Maitén* Belt (16-11 Ma). After an overall decline in the magnitude of volcanism, the third period of volcanic activity reached a new maximum during the Pliocene-Pleistocene along the North Patagonian Cordillera (Butler et al. 2020). Temporal variations in the lower Tertiary CS, determined by superposition in selected cross-sections, indicate that the major episodes begin with silicic associations (ignimbrite, plinian, and obsidian rhyolitic facies) and end with intermediate and basic lava flows (stratovolcanoes and monogenetic cones). K<sub>2</sub>O and total alkalis decrease southward for a given silica content in the *Pilcaniyeu* and *El Maitén* Belts (Santonja et al. 2021).

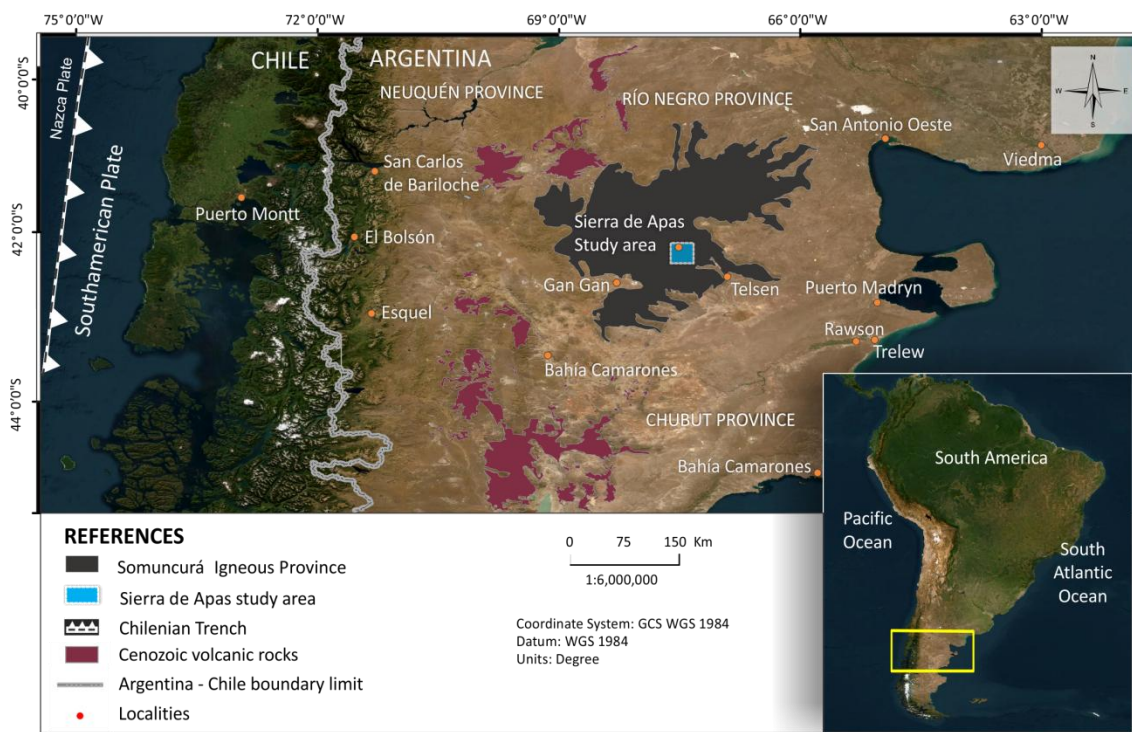


Figure 1. Satellite image showing the outcrops of extra-Andean Tertiary basic rocks. The blue square indicates the location of the studied area. Modified from Ardolino (1981) and Corbella (1984).

### 3 Materials and methods

The current research is based on fieldwork mapping, profiling of six stratigraphic sections, petrographic description, and U-Pb geochronology. Early

collected comprehensive data allows us to unravel *Sierra de Apas Volcanic Complex* stratigraphy. The lithofacies description of the volcanic deposits considers the structure, texture, internal organization, and geometry, following the Branney and Kokelaar (2002) and McPhie et al. (1993) criteria. The lithofacies were further organized into facies associations, representing groups of facies with shared environmental implications. The geological map of the identified units was created using SAS Planet, Google Earth, and ArcGIS 10.3 software.

The sample preparation at the *Laboratório Geológico de Preparação de Amostras (LGPA)* at the *Universidade do Estado do Rio de Janeiro (UERJ)* in Brazil include crushing in a jaw mill, and light and heavy minerals separation by hydraulic table and manual magnet and a Frantz. The non-magnetic fraction was subsequently processed with dense liquids, firstly with iodide and then with bromoform. Apatite minerals were later hand-picked and mounted in an epoxy mount.

U-Pb data was obtained from the flow-banded trachyte CAP 5 sample located at 42° 2' 21.12" S, 67° 27' 35.99" W on the eastern border of the *Sierra de Apas* crater rim. We analyzed the sample at the Multilab laboratory of the *Universidade do Estado do Rio de Janeiro*, Brazil (UERJ) and *Laboratório de Estudos Geodinâmicos, Geocronológicos e Ambientais* of the *Universidade de Brasília*, Brazil (UNB). The sample was prepared and analyzed using the SEM-EDS (Scanning Electron Microscopy-Energy Dispersive Spectroscopy) at Multilab. The isotope measures were obtained at UNB. (Supplementary Material, Appendix A) on a Thermo Finnigan Neptune XT high-resolution multi-collector sector field ICP-MS coupled to a 193 nm Teledyne Analyte Excite laser ablation system. Each isotope mass ( $^{202}\text{Pb}$ ,  $^{204}\text{Pb}$ ,  $^{206}\text{Pb}$ ,  $^{208}\text{Pb}$ ,  $^{232}\text{Th}$ ,  $^{238}\text{U}$ ) was measured simultaneously using a combination of Faraday, SEM, and CDD detectors. Data reduction was performed using the UComPbine DRS, which accounts for variable initial lead on the calibrant (Chew et al. 2014), and the corrections included blank subtraction, downhole fractionation using an exponential plus linear model, and normalization by the Durango apatite (Chew et al. 2011; McDowell et al. 2005). The initial lead for anchoring the data was 0.835 (Chew et al. 2011). Sumé apatite (Lana et al. 2022) was used for quality control. The apatite ages were calculated using Isoplot R 6.1.5 (Vermeesch, 2018).

#### 4 Sierra de Apas Caldera Volcanic Stratigraphy

Early studies into the *Sierra de Apas* Volcanic Complex have identified a broad compositional spectrum within the volcanic sequence, encompassing trachyte, trachy-basalts, and basalts (Croce, 1963; Corbella, 1975; Corbella and Linares, 1977; Remesal, 1988; Ardolino, 1981; Franchi et al. 2001). The *Quiñelaf* Complex comprises the majority of bimodal volcanic complexes in northern Patagonia, with the *Sierra de Apas* as a prominent example. Franchi et al. (2001) proposed an evolutionary sequence for the construction of the *Sierra de Apas* volcanic edifice, beginning with an explosive phase marked by extensive pyroclastic deposits. The trachytic lava flow follows this phase. Later, the occurrence of monogenic centers characterized by circular fractures allowed for the eruption of new lavas and the emplacement of trachytic domes. It concludes with basaltic and trachy-basaltic lavas. However, our field observations preserve some differences concerning the previous stratigraphic schemes of Ardolino (1981) and Franchi et al. (2001); see Table 1.

Ardolino (1981)	Franchi et al. (2001)	This contribution	
4- Final basic lava facies	Basalts and trachy-basalts	3. Pos-Caldera stage	11- Crater-Rim Olivine Basalts (Basalts III).
			10-Alkaline Gabbro Dikes.
3- Intrusive facies	Alkaline trachytic porphyries (Domes)		9-Intra and extra crater Commenditic Mesa Lavas and Lava Domes.
3- Intrusive facies (Dykes)	Alkaline trachytic porphyries (Dikes)		8- Trachytic Dikes.
	Alkaline trachytic porphyries (Domes)		7- Crater-Rim Lava Domes or Coulees.
2- Lava facies (Rhyolites and andesites and trachytes)	Light and dark trachytic lavas		6-Crater-Rim Trachytic Lava Flows.
			5-Intra-Crater Basaltic Lava Flows (Basalt II).
1- Pyroclastic facies	Pyroclastic rocks (Trachytic tuff, breccia, lapillites)	2. Syn-Caldera stage	4- Intra-Crater Trachytics Lavas and Lava Domes
			3-Intra-Crater Pyroclastic Density Current Deposits (PDC): Massive and Stratified Pyroclastic Deposits
			1. Pre-Caldera stage
			2-Intra and Extra-Crater Basalts (Somuncurá Formation, Basalt I).
			1- Intracrater Massive Gabbro

Table 1: Stratigraphic chart correlation of the *Sierra de Apas* volcanic system, using Ardolino (1981), Franchi et al. (2001), and this contribution.

The *Sierra de Apas* volcanic structure is 60 km northwestward of *Telsen* town in the *Chubut* Province. It constitutes a massive volcano, similar to the biggest calderas of the world (e.g., Menengai Crater, Great Rift Valley Kenia). It exhibits an amphitheater-shaped volcanic structure with a crater of 10 km radius and 88 km<sup>2</sup> area. The crater rim slopes extend over 15 km from the central area, reaching a maximum diameter of 27 km. The morphology facilitates the interpretation of basic stratigraphy and enables comparisons with other large polygenetic trachytic calderas, e.g., *Payún Matru* in Argentina (Hernando et al. 2012; 2019), and Menegai Kenia rift; Cameroon (Leat 1984). These formations typically feature a central block delineated by a prominent scarp with almost vertical walls up to 300 m high. In this context, internal records predate those in the caldera crater rim.

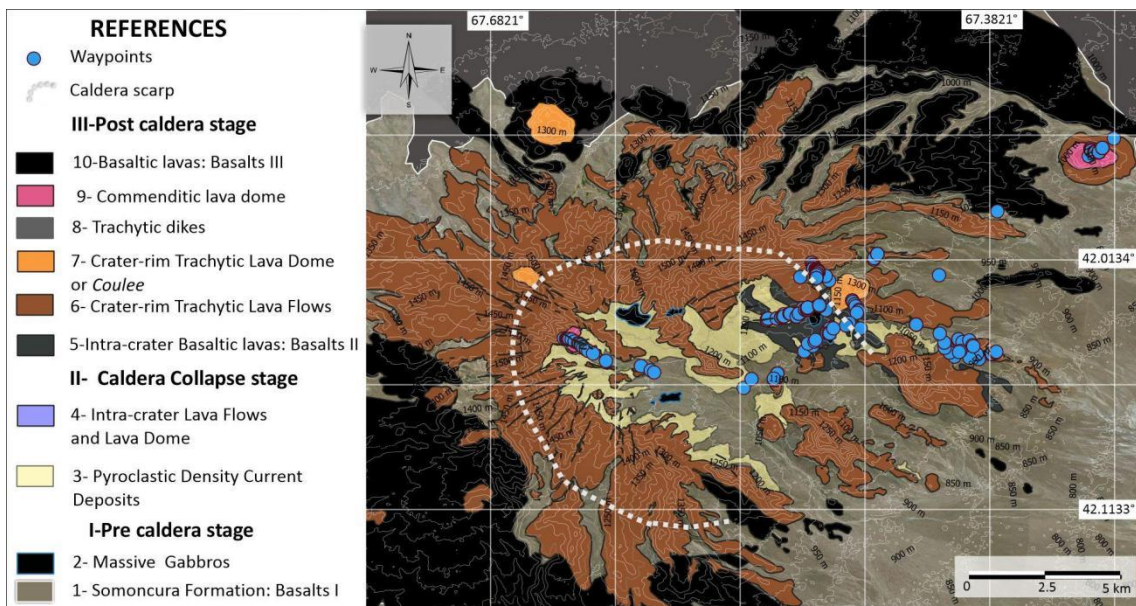


Figure 2. Geological map of the *Sierra de Apas* Caldera, modified from Ardolino (1981) using own observations. Units are described in the text.

#### 4.1 Pre-Caldera stage

##### 4.1.1 Intra-crater massive gabbros

Previously, Salani et al. (2022) recognized micro gabbros in the *Sierra de Apas* in the proximity of Puesto San Pedro (Fig. 3A). The outcrops described here had not been either identified or described; they crop out within the internal zone of the

volcanic caldera, about 4.7 km NE to the Puesto San Pedro. Gabbros form continuous outcrops ranging from 0.5 to 1.5 kilometers in diameter, corresponding to coherent facies. The outcrops are typically massive and dense, with a fine to medium-grained texture and a rounded morphology. The gabbros are greenish to dark-colored and contain varying percentages of pyroxene, plagioclase, and olivine, presenting equigranular and hypocrystalline ophitic texture. The jointed gabbros develop a preferential E-W orientation and occur at the same topographic level as intra-caldera trachytes, basalts, and pyroclastic deposits. The stratigraphic relationship with the host rocks is unclear due to the Quaternary cover.

#### **4.1.2 Intra and extra-crater volcanism (Somuncurá Formation, Basalt I)**

The *Somuncurá* Formation basalts have been described in several works (e.g., Corbella, 1984; Remesal, 1988) and consist of reddish to brown rocks due to the alteration of mafic minerals. They are olivine-rich, formed by one to six lava flow units (Ardolino et al. 1987). In the vicinity of the *Sierra de Apas* volcanic structure, these basalts are notably vesiculated and exhibit subrounded shapes with pronounced curved or cordate fluidity, interpreted as pahoehoe-type lavas (Fig. 3B). They have a reduced thickness, typically only a few tens of meters.

### **4.2 Syn-Caldera stage**

#### **4.2.1.a Intra-crater Pyroclastic Density Current (PDC) deposits**

Massive pyroclastic density current (PDC) facies are not welded and present a variable content of juvenile and basalt fragments. It comprises moderately poorly sorted massive ash to lapilli-tuff granulometry (< 0.2 to 0.5 with directional fabric (Fig 3E; see Table 2). Include K-feldspar, pyroxene, quartz, opaque free crystals, and carbonate alteration (Fig 3D).

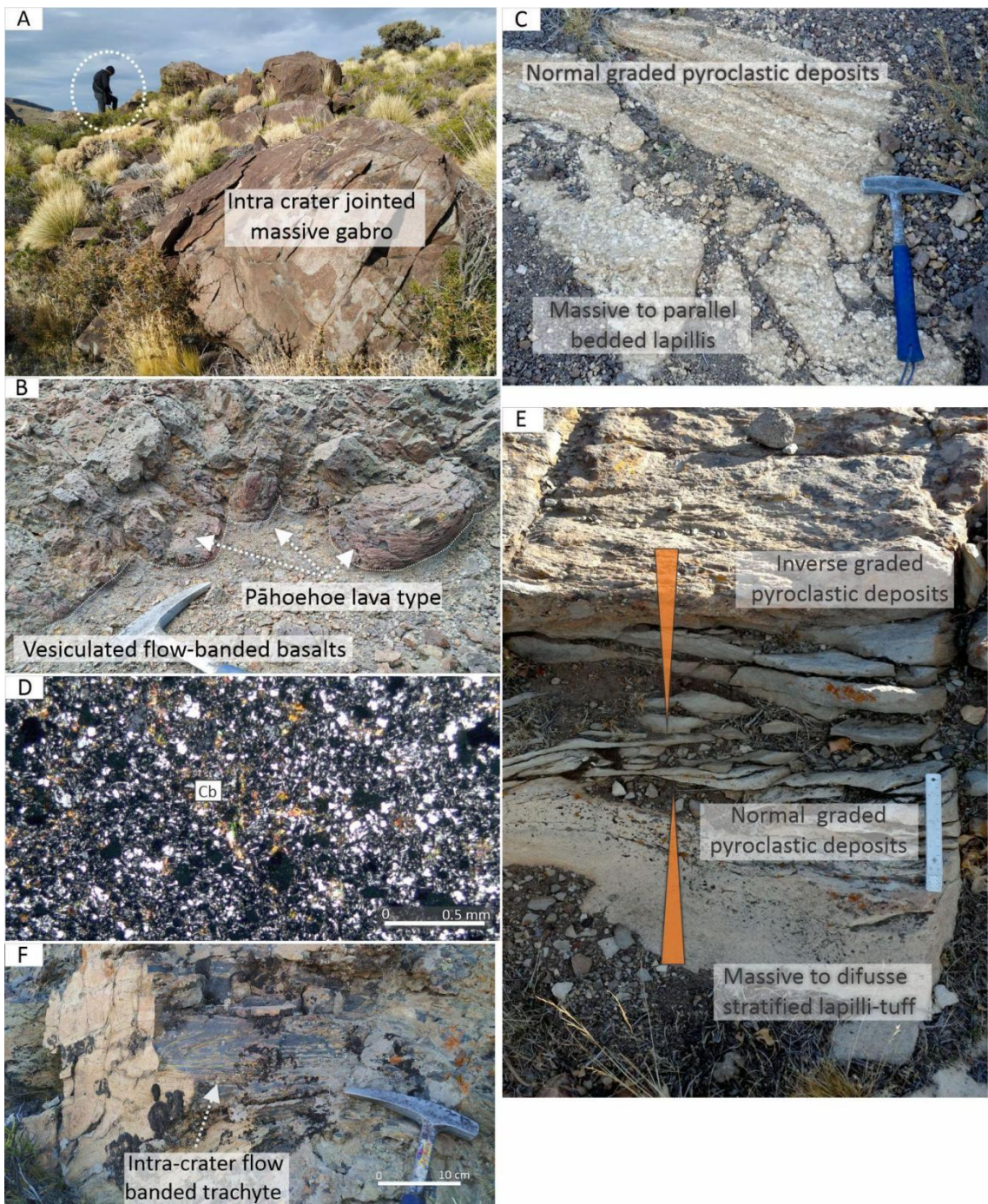


Figure 3. Pre and syn-caldera stage. A) Intra crater jointed massive gabbro outcrops; B) Upper section of basaltic Pāhoehoe lava type of the Somuncurá Formation; C) Stratified graded Pyroclastic fall-out deposits. D) Thin section of the Pyroclastic density current deposits showing a uniform granular lithology with carbonate (Cb) cementation. E) Massive to diffused stratified normal and inverse graded Pyroclastic deposits. F) Flow-banded glassy dark-colored, 250 m thick lava dome trachyte.

The massive lapilli tuffs (mLT) around the crater area are strongly scattered and eroded, presenting a white to light orange color, forming easily recognizable levels in satellite images. The thickness can't be measured, although it is inferred,

according to the altimetry of the outcrops, to be more than 125 m. It consists of crystals (2-10 %, 2-5 mm) and juvenile fragments 1-25 mm in diameter (25-40%). The basalt fragments constitute 2-5 % of samples and are 10-50 mm in size. The ash matrix is vitroclastic and composed of non-altered and partially oxidized glass shards. Some varieties are components. Distal mLT are interpreted in satellite images outside the caldera rim covering more than 400 km<sup>2</sup>, extending 40 km in an N120° direction, coinciding with the amphitheater location (S 42°12'40.05"-W 67°11'41.15"). Primarily depleted in lithic fragments and concentrated the highest populations of juveniles.

#### **4.2.1.b Fall out deposit**

The pyroclastic levels related to fall-out deposition consist of two main lithofacies, fine-grained well-sorted massive tuff (L5) and juvenile-rich well-sorted massive to parallel-bedded lapilli (L6) (see Table 2). They generally configure one discrete level underlain by the granular PDC deposits (L4) and the intra-crater trachytes (L2). The lateral continuity of the deposits is limited, and continuing the outcrops along the crater walls is challenging. Parallel bedding tuffs and lapilli (/T and //L) are well-selected and light gray. They form 5 to 300-cm thick individual strata, characterized by a flat, non-erosive arrangement. The parallel stratification varies between 0.5 to 10 cm thick. Deposits are usually graded, with a variable concentration of volcanic fragments, 8-15% free crystals, 59-87% pumice and glass fragments, and low concentrations of basalt fragments (1-5%). Tuffs and lapilli show a well-defined pyroclastic texture with vesicular pumice and glass fragments (Fig 3C).

These facies are considered to be deposited by ash falls in sub-air environments, constituting plinian or sub-plinian pumice fall layers. The good sorting of the deposits, the subparallel arrangement of the layers, and the relative abundance of vesiculated glass fragments are diagnostic characteristics of this type of deposit. Lateral continuity of the parallel beds, including normal grading, suggests unstable but almost uniform deposition (Branney and Kokelar, 2002). On the other hand, contents of juvenile fragments are occasionally more significant than 85% vol., suggesting a magmatic-driven fragmentation related to a shallow-setting explosion, with more juvenile ejection and limited presence of basaltic fragments. (e.g., Tchamabé et al. 2015).

#### 4.2.2 Intra-Crater Trachytic Lava Flows and Lava Dome

Trachytic magmatism was initially defined and recognized by Ardolino (1981), Ardolino (1987), and Remesal et al (2004). Trachytic lava flows, and domes occur in the intra-crater portion as small-size lava bodies concerning those developed in the crater rim portion (Fig. 3F). At the beginning of the volcanic activity, the intra-crater lavas had limited development and occupied the subsidized internal block showing two pulses. They are massive, coherent, coarse-grained rocks and crystal-rich facies or partially aphyric, glassy, and flow-banded, showing autoclastic breccias development. Intra-crater trachytic deposits typically show truncated morphologies obscured by later pyroclastic and lava records.

The lava flows in this sector typically range from 10 to 50 meters in thickness, particularly along the northern scarp. These rocks often display columnar joints, vesicles, and amygdales with vitreous textures, suggesting subaerial cooling. Lava domes are significantly thicker than trachytic lavas and can reach 250 meters. The internal structure of the trachytic lava domes predominantly features dark-colored flow-banded facies and minor autoclastic breccias. To the northwest of *Puerto Ibañez*, a prominent profile records one of these lava bodies ( $42^{\circ} 2'41.44''S$ ;  $67^{\circ}36'0.37''W$ ) and illustrates the stratigraphic relationships between three intracrater deposits. This profile reveals fine-grained gabbros at the base ( $42^{\circ} 2'57.25''S$ ;  $67^{\circ}35'32.02''O$ ) overlain by pyroclastic deposits and the mentioned trachytic lava dome. Crater rim trachytes crowned the intracrater succession, and trachytic dikes intruded the entire profile.

### 4.3 Post-Caldera stage

#### 4.3.1 Intra-crater basaltic lava flows (Basalt II)

Intra-crater basalts are intensely oxidized, a characteristic concern of basalts II and III. Basalts II vary from aphyric to porphyritic in texture, often exhibiting flow banding with local development of breccias. Their thickness is reduced (c.a. 10-25 m) and forms non-uniform outcrops that generally overlay the intra-crater trachytic facies covered by the caldera rim, trachytic lavas and are considered as previous to the final basic lava facies described by Ardolino (1981).

#### 4.3.2 Crater-Rim Trachytic Lava Flows

Trachytic lava flows constitute the most significant geological element of the Sierra de Apas caldera, reaching 13 km of lateral extension along their strike. It consists of elongated tabular, partially inclined, and asymmetric trachytic bodies. Lavas build up the caldera rim, showing a diverging flow arrangement from a subcircular ring fracture, and comprise a set of polycyclic effusions, constituting patterns of 2 to 7 overlapping flows (Fig. 4A).

The individual flows are 20 to 80 m thick and are composed of lithofacies 8, constituting a typical stacking pattern (Table 2). The trachytic lavas present trachytic and porphyritic textures, with aphanitic groundmass and variable crystal groundmass ratios between 30/70 and 40/60. Groundmass is hypocrystalline, equigranular, and aphanitic (less than 0.1 mm). The most outstanding characteristic of the trachytic rocks is the orientation of the minerals in the groundmass that contours the phenocrysts. The mineralogy comprises K-feldspar crystals, quartz, clinopyroxene, augite and aegirine, apatite, and opaque minerals (Figs. 4B and C).

The contractional curved ridges constitute another common feature, as well as the frequent folding of flow bands due to the effect of longitudinal flow compression and external resistance to the advancement of trachytic lava (Fig. 4D). These features mark the flow direction and characterize most of the lava flows.

#### 4.3.3 Crater-Rim Lava Domes or Coulees

Two trachytic lava domes or coulees were recognized in the study area, characterized by a sub-circular shape in plan view, partially elongated in the NNE direction. Each covers a 2.5 to 3 km<sup>2</sup> area, 250 to 400 m above the adjoining surface. The bodies have concave-shaped roofs and a central upward flow banding that is progressively horizontal laterally. One of them is located at 42°01'28" S, 67°29'15" W, coinciding with the caldera crater rim location, with the second one at 41°57'30"S 67°36'30"W over the crater rim lava flows.

The first consists of coherent lithofacies and massive flow banding with columnar joints, displaying a markedly porphyritic to glomeroporphyritic texture with feldspar crystals that reach 3 cm. The trachytic flow bands dip at a moderate to high angle from the central zone and coincide with exogenous lava growth where magma is located at the dome roof (Fig. 4E). The banding is generally 20 to 150 cm thick. It

is truncated by strong vertical cleavage 0.5 to 4 meters thick in an N 287° predominant direction. The southeast face of the body reveals an asymmetrical profile linked to a differential development characterized by an SW projection. Monomictic massive trachytic breccias occur at the top of the lava domes. They are primarily fine-grained, dark-colored, and easily identified in the field. Occasionally, in the contact between lava flows, magma injection is recognized through discrete fissures of 0.5 m to 2 m thick (Fig. 5A).

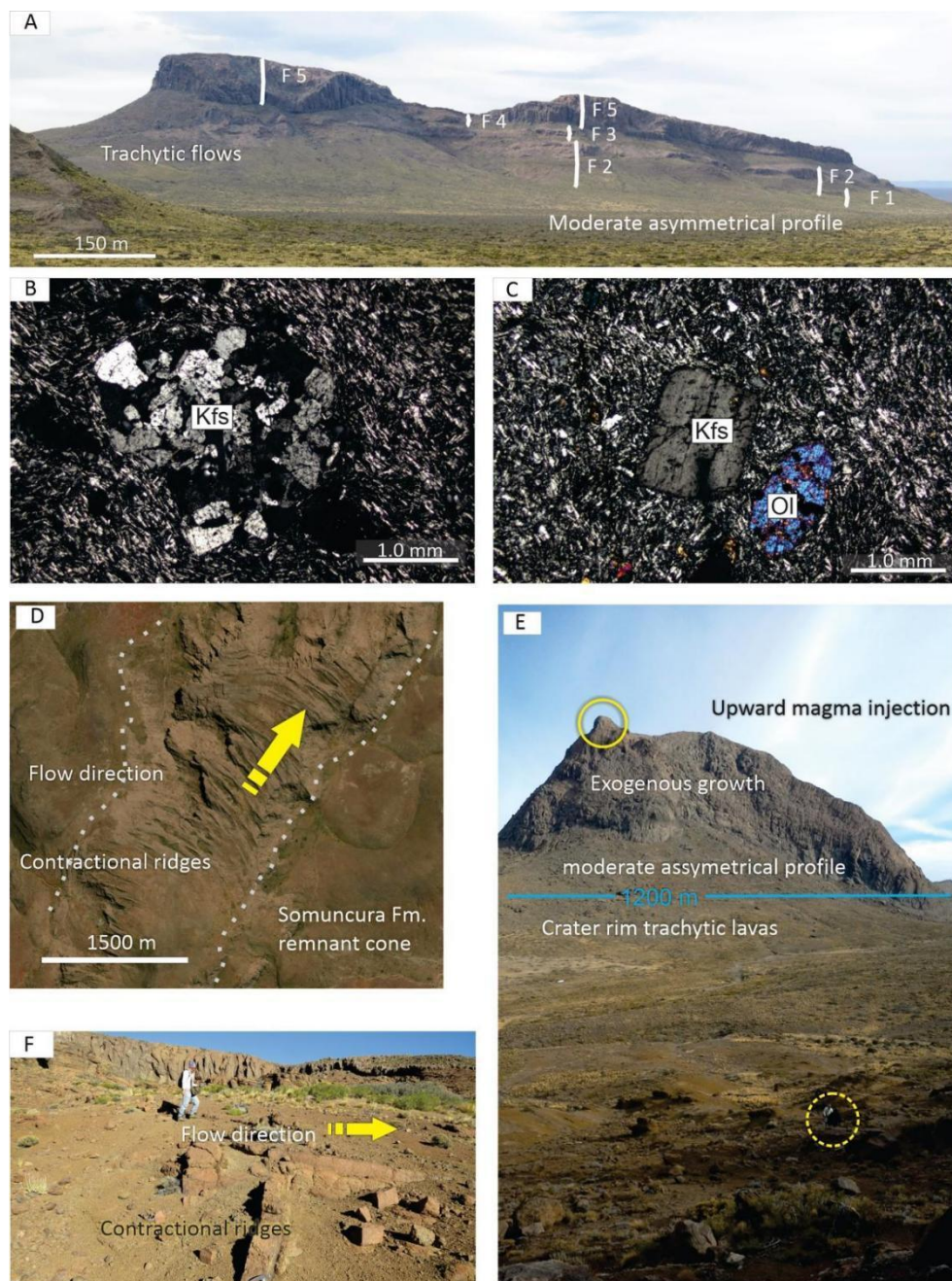


Figure 4. Post-Caldera stage. A) Set of crater rim dominated trachytic lithofacies, showing a moderate asymmetric profile; B) and C) Microphotographs of trachytic lithofacies; D) Aerial view of the Somuncura Fm. remnant cone; E) Upward magma injection; F) Flow direction and contractional ridges.

lavas and domes displaying "sieve" texture, with an abundance of K-feldspar glomerulus and olivine crystals. D) Satellite image of contractional ridges indicating the flow direction. E) Intra-crater jointed massive gabbro, rim trachytic lavas, and lava dome outcrops. F) Field picture showing contractional ridges.

#### 4.3.5 Trachytic Dikes

The dikes range from 2 to 10 m thick, 1 to 4 kilometers long. Exhibit textural and mineralogical characteristics comparable to the crater rim trachytic lavas. Characteristically, the dikes display a radial arrangement (Corbella, 1975), which characterizes most of the large volcanic edifices (see Acocella, 2008) and serve as feeders for the trachytic lava along the caldera rim structure (Fig. 5B).

The dikes also cut the trachytic lavas and consist of massive facies with pronounced jointing, typically perpendicular to the thermal gradient or the contacts with the bedrock. The dikes are markedly coarse-grained and predominantly massive, exhibiting locally intense upward flow banding (Fig. 5C).

#### 4.3.6 Intra and Extra Crater Commenditic Mesa Lavas and Lava Domes.

Remarkably, these rocks occupy a clearly defined stratigraphic position in the evolution of the volcanic system and overlay the crater rim trachytic lava flows. They are composed of massive lavas with dominant flow banding. This facies forms small mesa lavas in the intra-crater area ( $42^{\circ} 3'45.64''$  S;  $67^{\circ}31'4.94''$  W) and the *Cerro Colorado*, on the northeastern flank of the volcano crater rim (Fig. 5D and E, respectively). The *Cerro Colorado* commenditic lava body is 220 m thick and has an elliptical shape in plan view, with axes measuring 3 and 2 kilometers, elongated in an east-west direction. The internal and external lava bodies are gray-colored commendites with prominent horizontal flow banding that indicates fluidity. A significant growth of vesicles characterizes these rocks, particularly in the *Cerro Colorado* area. Finally, both sectors exhibit substantial vertical columnar jointing arrangements.

Mesa lavas and lava domes have similar macroscopic features, with a porphyritic texture and aphanitic groundmass. The mineralogy in a holocrystalline matrix includes K-feldspar, quartz, aegirine, augite, apatite and opaque minerals (Fig. 6A and B). The K-feldspars are mainly composed of sanidine and anorthoclase; augite and aegirine crystals also display a sieved texture. The phenocryst-to-

groundmass ratio ranges from 10/90 to 20/80. The microphenocrysts grade, defining a serial texture. The felsitic, granophytic, and micro granular intergrowth textures composed of quartz and K-feldspars occur frequently.



Figure 5. Post-Caldera stage. A) Magma injection through discrete fissures of 0.5 m to 2 m in the crater rim trachytes. B) Trachytic dikes showing thermal joints and upward flow bands. C) Crater rim trachytes, partially intruded by radial dikes of the same composition. D) Well-developed vertical columnar joints in the intracrater commenditic mesa lava. E) The commenditic lava dome is located in the external portion of the crater, showing near horizontal flow bands and vesicle distribution.

#### 4.3.7 Alkaline Gabbro Dikes

The alkaline gabbro intrusions are rare in the *Sierra de Apas* geological records. It crops out at coordinates  $42^{\circ} 2'12.57''\text{S}$  and  $67^{\circ}31'12.98''\text{W}$ , where they cut the trachyte dikes (Fig. 6C). These syn-volcanic intrusions, together with the commenditic facies, are considered the final volcanic phases of the system. Alkaline gabbro intrusions are 400 m long and 30 m thick (Fig. 6D and E). The gabbros are characterized by their massive medium- to fine-grained texture (0.8-4 mm) and moderate jointing (Fig 7A). They are gray, with the intergranular plagioclase filling the spaces between the pyroxene and olivine. The dominant mineralogy is olivine, clinopyroxene, amphibole (kaersutite), plagioclase, opaque minerals, and quartz (Fig 7B and C).

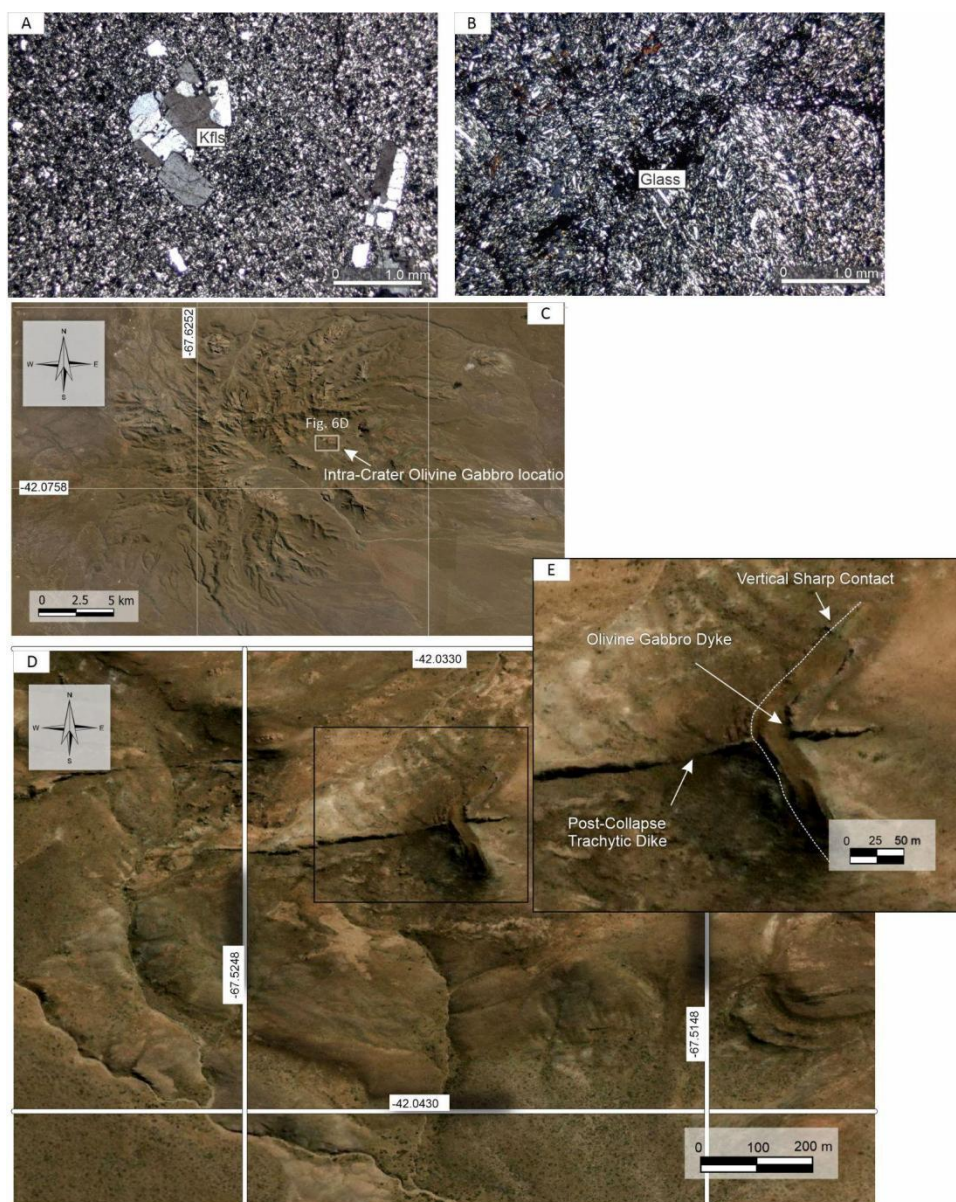


Fig. 6. A) Microscope photograph of the mesa lavas showing a trachytic texture with K-feldspar glomerulus. B) Idem for lava domes, displaying the presence of isotropic glass. C) Satellite image showing the location of Intra-crater gabbro. D and E) Idem, showing relationships between gabbro dike and Post-collapse trachytic dike.

#### 4.3.8 Crater-Rim Olivine Basalts (Basalts III).

Post-caldera Basalts III have darker colors in satellite images, exhibit markedly flat morphology, and constitute the external portion of the crater rim structure. Related outcrops have not been identified during the confection of the stratigraphic sections; however, they are easily recognized on satellite images and assigned as the upper basalts defined by Ardolino (1981) and Remesal et al. (2004).

The samples exhibit porphyritic to glomeroporphyritic textures with a pilotaxitic groundmass, inequigranular, and hypocrystalline (Fig 7D and E). The predominant minerals include olivine, iddingsite, clinopyroxene (augite), plagioclase, and opaque minerals. Differences between the analyzed outcrops include crystal size variations, olivine concentration, and oxidation degree.

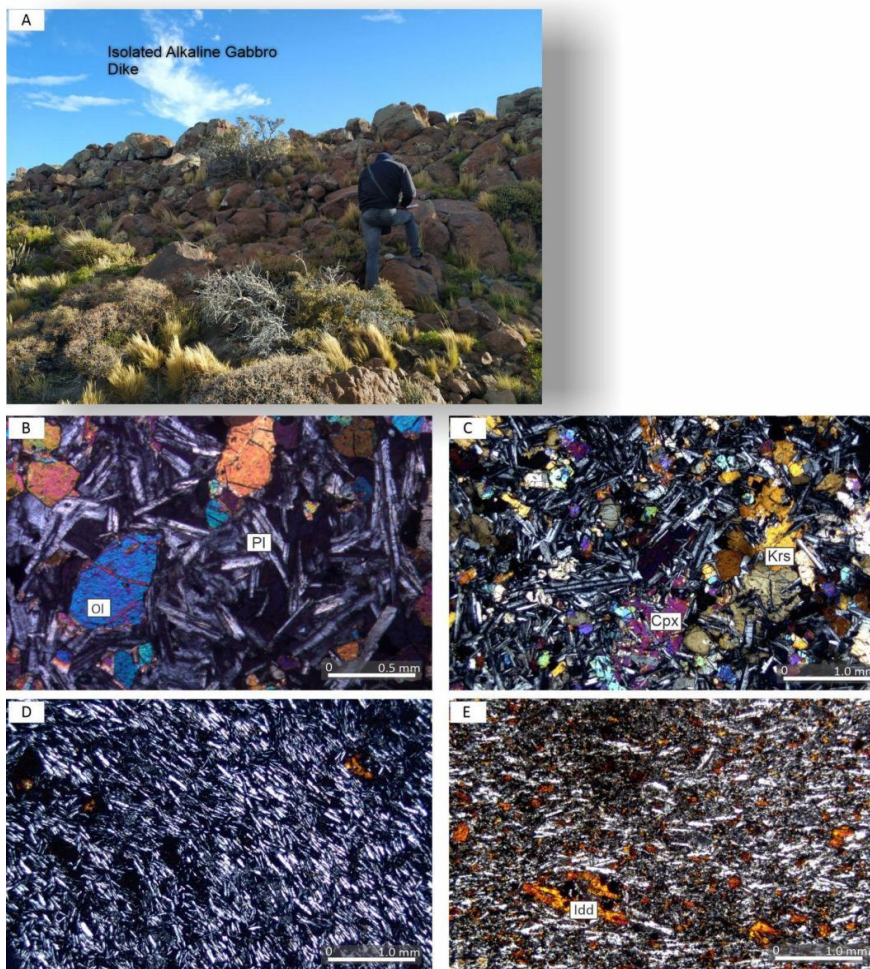


Figure 7. Post-Caldera stage. A) Outcrop of alkaline gabbro dike. B) Microphotograph of alkaline gabbro showing olivine (Ol) and plagioclase (Pl) forming an ophitic texture. C) Microphotograph of Intra-crater massive gabbro with clinopyroxene (Cpx) and kaersutite (Krs). D) Microphotograph flow banded vesiculated olivine basalts with alteration of olivine to iddingsite (Idd). E) Likewise, but considerably more altered, with iddingsite.

## 5 Apatite U-Pb age of the crater rim trachytic lava flows

From the crater rim trachytic lava flow, we obtain two U-Pb ages in apatite (Fig. 8). The sample is located at  $42^{\circ} 2' 21.12''$  S,  $67^{\circ} 27' 35.99''$  W. Thirty grains were analyzed, and isotopic ratios data are in Supplementary Table 3. The sample has two groups of apatite, colorless (Fig. 8A) and yellow-brown (Fig. 8B). The colorless grains are transparent and have a vitreous luster, and the yellowish-brown ones are translucent. The size of the crystals ranges from 60 to 250 m. In addition, the images showed several sets of rough fractures and irregular boundaries in the crystal structure. To avoid possible differences between the apatite, the colorless and yellow-brown apatite ages were also calculated separately.

U-Pb isotopic data define a Concordia array that scatters between radiogenic and non-radiogenic components on the Tera-Wasserburg diagram. The lower intercept ages are 25.95 ± 1.89 Ma and 25.74 ± 1.73 Ma for the colorless and yellowish-brown grains, respectively. U contents and Th/U ratio are similar between both groups of apatite, 5-10 ppm and 0.5-0.8, respectively. The combined data represents the trachytic lava flow crystallization age, with a lower intercept age of  $26.5 \pm 1.3$  Ma ( $n = 28$ ; MSWD = 0.98).

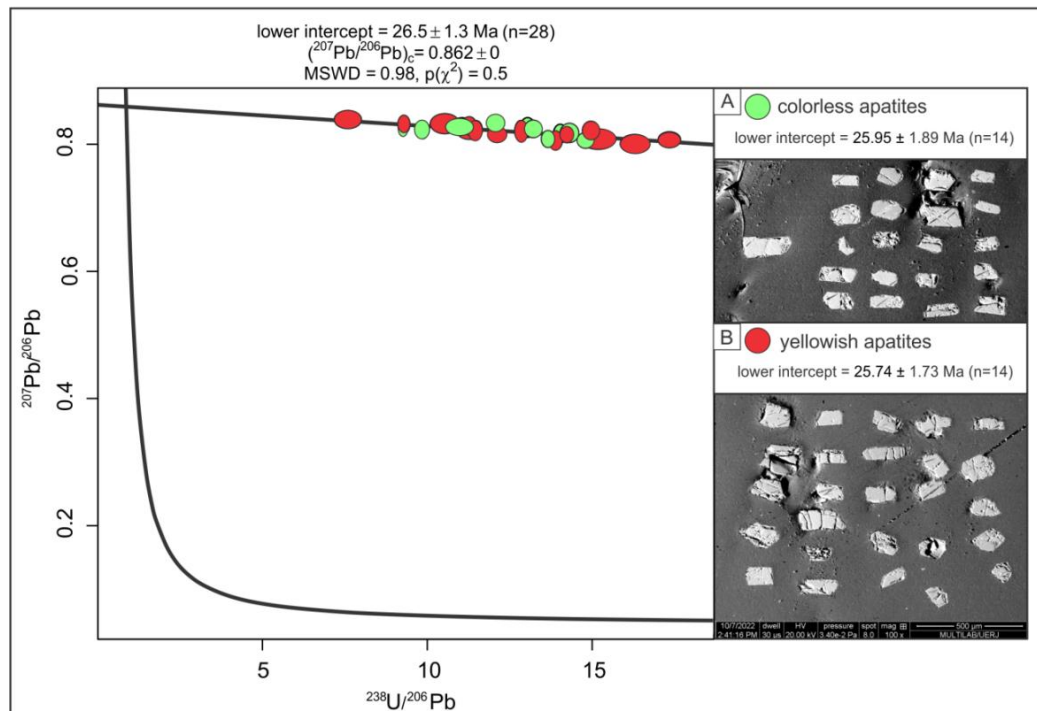


Figure 8. Tera-Wasserburg diagram showing the lower intercept age of the colorless and the yellowish apatite of the *Sierra de Apas* caldera trachyte lava flow. A) Colorless apatite cathodoluminescence image, marking the related intercept age. B) Yellowish apatite cathodoluminescence images with the related intercept age.

## 6 Discussion: an evolutionary model of the *Sierra de Apas* Caldera

### 6.1 Pre-caldera stage

The pre-caldera stage in the *Sierra de Apas* volcanic system involves three primary deposits exposed along the floor and the NE inner slopes of the caldera. They are the massive gabbros, the basalts I, and the intra-crater trachyte lava flow and lava dome. These three types of records are part of the floor of the volcanic caldera and probably constituted the first records of the crater, being recognized from profiles 1 to 6 (Fig. 9). Massive gabbros possibly constitute the superficial chambers of the Somuncura Formation basalts (Basalts I). This stage wasn't described by Ardolino et al. (1981), Franchi (2001), and Salani et al. (2022).

Regarding the age of this stage, there are no ages in the *Sierra de Apas* zone, but Kay et al. (2007) indicated Ar/Ar ages for pre-plateau rocks of  $29 \pm 1.5$  Ma in the *Ranquil Huao* sequence, located 90 km south. For the case of plateau rocks, K/Ar ages are between 33 and 22 Ma, with an  $^{40}\text{Ar}/^{39}\text{Ar}$  of  $26.9 \pm 0.8$  Ma (Kay et al. 2007). Shield volcanoes, in general, both of basaltic and trachytic compositions, constitute

evolutionary systems that are generally short-lived (e.g., Suswa volcano; Menengai caldera; Payun Matru caldera; White et al. 2012; Leat 1984; Germa et al. 2010) covering near to 0.1-0.5 Ma.

## 6.2 *Syn-caldera stage*

The intra-caldera massive pyroclastic density current, including fall-out and granular deposits, represents this stage, limited to the caldera interior (Fig. 9). This process significantly deforms and erodes the Pre-caldera records, exposing the upper portions of the shallow gabbros. In addition, these records occurred before the post-collapse stage and the main crater rim growing phase. These deposits were described by Ardolino et al. (1981) and Fanchi et al. (2001) as pyroclastic rocks. Because these rocks cover the Pre-caldera deposits with an age of 29 Ma (Kay et al. (2007) and are covered by rock here dated 26 Ma, this pyroclastic event must be short, in the range of 3Ma. A similar interval was considered by Remesal (1988), based on K/Ar data, for the Somuncura province volcanism. Based on paleomagnetic data, Orgeira and Remesal (1993) proposed that the interval from 27.5 to 25 Ma was from flows in the northeastern *Meseta de Somuncurá*.

## 6.3 *Post-collapse stage*

After the collapse, the volcanic activity of the *Sierra de Apas* Caldera was mainly effusive, starting with the eruption of intermediate to basic lavas (Basalts II, and crater rim trachytic lava flows, (Fig. 9, profiles 6 and 7). These records dominate the post-collapse deposits. Lava domes and dikes represent subvolcanic and intrusive events. During this phase, the volcano growth shows a polycyclic compositional shift from less to more evolved compositions without showing textural evidence of mingling and mixing processes between basaltic and trachytic magmas. The crater rim trachytic lava has a U-Pb age of  $26.5 \pm 1.3$  Ma, which is also in the range of the interval proposed by Orgeira and Remesal (1993). An Ar/Ag age of  $28 \pm 1$  Ma was also obtained by Salani (1999) for the El Buitre Formation.

The Somuncurá Formation ages (Ardolino, 1981) and the new Upper Oligocene U-Pb geochronological data of the rim trachytes allow us to constrain the caldera collapse interval to the Upper Oligocene. This significant eruption presents a clear direction towards the southeast and is considered responsible for the amphitheater

and the ring scarp formation. Characteristically, the SE caldera flank is strongly bisected, and the pyroclastic records extend more than 20 km beyond their limit. The authors believe that the *Sierra de Apas* volcanic system was built up entirely during the upper Oligocene (26 Ma).

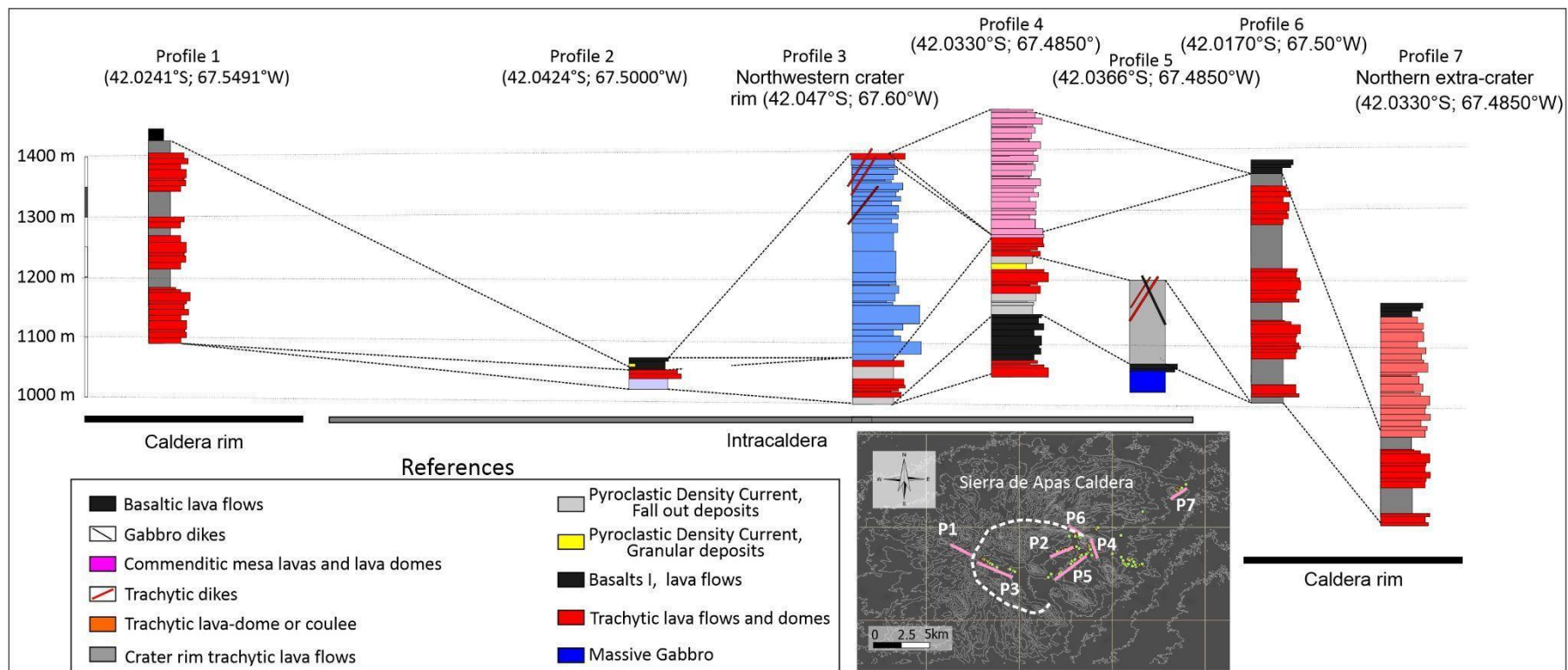


Figure 9. The correlation of the *Sierra de Apas* caldera's stratigraphic succession shows the locations of the intracrater and crater rim volcanic deposits.

## 7 Conclusions

The *Sierra de Apas* Volcanic Complex constitutes a 10 km diameter bimodal collapse caldera. Recognizing 11 volcanic elements supports characterizing a volcanic structure that evolves during three main evolutionary stages: Pre-collapse, Syn- and Post-collapse. The Somoncurá basalts and intra-caldera massive gabbros represent the pre-caldera stage. The inside crater's massive and stratified pyroclastic deposits and minor trachytes lavas represent the syn collapse stage. Finally, the post-collapse lavas, lava domes, and dikes -trachytic, gabbro/basalt, and commenditic composition- mark the crater rim consolidation.

The new U-Pb age in apatite minerals shows that post-collapse crater rim trachytes of *Sierra de Apas* Caldera erupted during the Upper Oligocene (26.5 Ma, Chattian Stage). This geochronological data supports the existence of a brief and constrained time interval between pre-collapse and post-collapse magmatism. In this sense, the present contribution proposes a common origin and a very short duration interval for gabbros, basalts, and trachytes, which show diverse and pulsating shear relationships in the *Sierra de Apas* area (including *Somuncura* Fm, *El Buitre* Gabbros, and *Sierra de Apas* trachytes or *Quiñelaf* Complex trachytes).

## Funding and Acknowledgments

The authors thank the CONICET (PIBAA 2022- 2023 N°100399) and AGENCIA (PICT-2021-I-INV1-00388 for supporting this research. The major of Telsen Leonardo Bowman and Carlos Mirantes, the Pto Curaqueo Ranch Owner, are responsible for providing logistic support and access. This work was supported by the CNPq (Pro Trindade Program) [Process No. 557,146/2009-7]; the MCT/CNPq project [no 26/2009]; the Universidade do Estado do Rio de Janeiro for PROCAD Program (Capacitation Program) leave and CAPES [Process 88.881.177228/2018-01] for the postdoctoral fellowship, to execute part of this research at Aveiro University and Lisboa University, Portugal, and FAPERJ [Entidades Estaduais 2018 n° 210.297/2018; APQ1 2019 n° 210.179/2019; JCNE 2022 n° 201.469/2022]. Msc. Gilmar Pachá would like to thank the cooperation with the laboratory and the laboratory technician who helped me to develop the analyses, Gabriela from LGPA/UERJ; Wagner from Multilab/UERJ; Carla Neto LAGIR/UERJ; Dr. Guilherme Gonçalves and Dr.Tiago Jalowitzki from LEGGA/UNB; and Laboratorio de Petrotomía INGEOSUR-UNS. Dr. Anderson Santos would like to thank CNPq PQ 2021 Process nº 304837/2021-0 for all support. Dr. Anderson Santos would like to thank the research groups from which he has developed several partnerships, such as GeoBioTec (Aveiro University, Portugal), Dom Luiz Institute (Lisboa University,

Portugal), Tektos Group, and GeoAtlantic Institute (Rio de Janeiro State University, Brazil).

### **Author Statement**

Gilmar Pachá Corrêa dos Santos da Silva: conceptualization, methodology, development, validation, formal analysis, investigation, writing - original draft, visualization, project administration; Anderson Costa dos Santos: conceptualization, methodology, validation, formal analysis, investigation, resources, data curation, writing – original draft, supervision, project administration, and funding acquisition; Leonardo Benedini: conceptualization, methodology, validation, formal analysis, investigation, resources, writing – original draft, supervision, project administration, funding acquisition; review, corrections; Guilherme Gonçalves: methodology, writing, validation, resources, writing – review and editing; Mauro Geraldès: resources and funding acquisition; Daniel A. Gregori: writing, conceptualization, resources, project administration, and funding acquisition, review; corrections; Tiago Jalowitzki: methodology, writing, validation, resources, writing – review and editing;

### **References**

- Acocella, V., 2008. Activating and reactivating pairs of nested collapses during caldera-forming eruptions: Campi Flegrei (Italy). *Geophysical Research Letters*, 35(17).
- Aragón, E., Pinotti, L., D'Eramo, F., Castro, A., Rabbia, O., Coniglio, J., Demartis, M., Hernando, I., Cavarozzi, C.E., Aguilera, Y.E., 2013. The Farallon-taluk ridge collision with South America: Implications for the geochemical changes of slab window magmas from fore- to back-arc. *Geosci. Front.* 4, 377–388. <https://doi.org/10.1016/j.gsf.2012.12.004>
- Ardolino, A.A., 1981. El Vulcanismo Cenozoico del borde sudoriental de la Meseta de Somuncurá, provincia de Chubut. 8º Congreso Geológico Argentino. Abstracts 2, 7–23.
- Ardolino, A. A., 1987. Descripción geológica de la Hoja 42f, Sierra de Apas. Dirección Nacional de Minería y Geología.
- Branney, M. J., Kokelaar, B. P., 2002. Pyroclastic density currents and the sedimentation of ignimbrites. *Geological Society of London. Memoir* 27, 152 pp.
- Butler, K. L., Horton, B. K., Echaurren, A., Folguera, A., & Fuentes, F., 2020. Cretaceous-Cenozoic growth of the Patagonian broken foreland basin, Argentina: Chronostratigraphic framework and provenance variations during transitions in Andean subduction dynamics. *Journal of South American Earth Sciences*, 97, 102242. <https://doi.org/10.1016/j.jsames.2019.102242>

- Chew, D. M., Sylvester, P. J., Tubrett, M. N., 2011. U–Pb and Th–Pb dating of apatite by LA-ICPMS. *Chemical Geology*, 280(1-2), 200-216. <https://doi.org/10.1016/j.chemgeo.2010.11.010>
- Chew, D. M., Petrus, J. A., Kamber, B. S., 2014. U–Pb LA–ICPMS dating using accessory mineral standards with variable common Pb. *Chemical Geology*, 363, 185-199. <https://doi.org/10.1016/j.chemgeo.2013.11.006>
- Corbella, H., 1975. Diseño radial de diques traquíticos en la sierra de Apas, Macizo Nordpatagónico, provincia de Río Negro, Argentina. *Revista de la Asociación Geológica Argentina*, 30(1), 110-11.
- Corbella, H., Linares, E., 1977. Acerca de la naturaleza peralcalina y la edad de algunos afloramientos volcánicos de la Sierra de Apas y de la Sierra Negra de Telsen, Macizo Nordpatagónico, provincias de Río Negro y Chubut, Argentina. *Revista de la Asociación Geológica Argentina*, 32(2), 152.
- Corbella, H., 1984. El vulcanismo de la Altiplanicie del Somuncurá. En *Geología y Recursos Naturales de la Provincia de Río Negro*. Relatorio del IX Congreso Geológico Argentino p. 267-300.
- Cordenons, P. D., Remesal, M. B., Salani, F. M., Cerredo, M. E., 2020. Temporal and spatial evolution of the Somuncurá magmatic province, northern extra-andean Patagonia, Argentina. *Journal of South American Earth Sciences*, v. 104, p. 102881. <https://doi.org/10.1016/j.jsames.2020.102881>
- Croce, R., 1963. El sistema del Somuncura. Las Altas Sierras del Somuncura y sus aledaños. *Revista del Museo Argentino de Ciencias Naturales Bernardino Rivadavia, Ciencias Geológicas* 6: 303-321.
- De Ignacio, C., López, I., Oyarzun, R., Márquez, A., 2001. The northern Patagonia Somuncura plateau basalts: a product of slab-induced, shallow asthenospheric upwelling?. *Terra Nova*, 13(2), 117-121. <https://doi.org/10.1046/j.1365-3121.2001.00326.x>
- Espinoza, F., Morata, D., Pelleter, E., Maury, R.C., Suárez, M., Lagabrielle, Y., Polvé, M., Bellon, H., Cotten, J., De la Cruz, R., Guivel, C., 2005. Petrogenesis of the Eocene and Mio-Pliocene alkaline basaltic magmatism in Meseta Chile Chico, southern Patagonia, Chile: evidence for the participation of two slab windows. *Lithos* 82, p. 315–343. <https://doi.org/10.1016/j.lithos.2004.09.024>
- Folguera, A., & Ramos, V. A. (2002). Partición de la deformación durante el Neógeno en los Andes Patagónicos Septentrionales (37-46 S). *Revista de la Sociedad Geológica de España*, 15(1-2), 81-93.
- Franchi, M., Ardolino A.A. Remesal, M., 2001. Hoja Geológica N° 4166-III, Cona Niyeu. Provincia de Río Negro. Instituto de Geología y Recursos Minerales, Servicio Geológico Minero Argentino. Boletín 262: 1-114, Buenos Aires.

- Germa, A., Quidelleur, X., Gillot, P. Y., Tchilinguirian, P., 2010. Volcanic evolution of the back-arc Pleistocene Payun Matru volcanic field (Argentina). *Journal of South American Earth Sciences*, 29(3), 717-730. <https://doi.org/10.1016/j.jsames.2010.01.002>
- Giacosa, R. E., Afonso, J. C., Heredia, N., & Paredes, J. (2005). Tertiary tectonics of the sub-Andean region of the North Patagonian Andes, southern central Andes of Argentina (41–42° 30' S). *Journal of South American Earth Sciences*, 20(3), 157-170. <https://doi.org/10.1016/j.jsames.2005.05.013>
- Gianni, G.M., Pesce, A., Soler, S.R., 2018. Transient plate contraction between two simultaneous slab windows: insights from Paleogene tectonics of the Patagonian Andes. *J. Geodyn.* 121, 64–75. <https://doi.org/10.1016/j.jog.2018.07.008>
- Gorring, M. L., Kay, S. M., Zeitler, P. K., Ramos, V. A., Rubiolo, D., Fernandez, M. I., Panza, J. L. 1997. Neogene Patagonian plateau lavas: continental magmas associated with ridge collision at the Chile Triple Junction. *Tectonics*, 16(1), 1-17. <https://doi.org/10.1029/96TC03368>
- Hernando, I. R., Llambías, E. J., González, P. D., Sato, K., 2012. Volcanic stratigraphy and evidence of magma mixing in the Quaternary Payún Matrú volcano, Andean backarc in western Argentina. *Andean Geology*, 39. <https://doi.org/10.5027/andgeoV39N1-a08>
- Hernando, I. R., Petrinovic, I. A., D'Elia, L., Guzmán, S., Paez, G. N., 2019. Post-caldera pumice cones of the Payún Matrú caldera, Payenia, Argentina: Morphology and deposits characteristics. *Journal of South American Earth Sciences*, 90, 453-462. <https://doi.org/10.1016/j.jsames.2018.12.017>
- Iannelli, S. B., Fernández Paz, L., Litvak, V. D., Jones, R. E., Ramos, M. E., Folguera, A., & Ramos, V. A., 2018. Paleogene arc-related volcanism in the southern central Andes and north Patagonia (39–41° S). *The Evolution of the Chilean-Argentinean Andes*, 343-359. [http://dx.doi.org/10.1007/978-3-319-67774-3\\_14](http://dx.doi.org/10.1007/978-3-319-67774-3_14)
- Iannelli, S. B., Fennell, L., Fernández Paz, L., Litvak, V. D., Encinas, A., & Folguera, A. (2020). Late Cretaceous to Oligocene magmatic evolution of the Neuquén basin. Opening and closure of the Neuquén Basin in the southern Andes, 397-416. [http://dx.doi.org/10.1007/978-3-030-29680-3\\_16](http://dx.doi.org/10.1007/978-3-030-29680-3_16)
- Kay, S. M., Ardolino, A. A., Gorring, M. L., Ramos, V. A. 2007. The Somuncura Large Igneous Province in Patagonia: Interaction of a Transient Mantle Thermal Anomaly with a Subducting Slab. *Journal of Petrology*, 48(1), 43-77. <https://doi.org/10.1093/petrology/egl053>
- Lana, C., Gonçalves, G. O., Mazoz, A., Buick, I., Kamo, S., Scholz, R., Wang, H., Moreira, H., Babinski, M., Queiroga, G., 2022. Assessing the U-Pb, Sm-Nd, and Sr-Sr Isotopic Compositions of the Sumé Apatite as a Reference Material for LA-ICP-MS Analysis. *Geostandards and Geoanalytical Research*, 46(1), 71-95. <https://doi.org/10.1111/ggr.12413>

- Leat, P. T., 1984. Geological evolution of the trachytic caldera volcano Menengai, Kenya Rift Valley. *Journal of the Geological Society*, 141(6), 1057-1069. <https://doi.org/10.1144/gsjgs.141.6.1057>
- Litvak, V. D., Poma, S., Jones, R. E., Fernández Paz, L., Iannelli, S. B., Spagnuolo, M., ... & Ramos, V. A. (2018). The late Paleogene to Neogene volcanic arc in the southern Central Andes (28–37 S). *The Evolution of the Chilean-Argentinean Andes*, 503-536. [http://dx.doi.org/10.1007/978-3-319-67774-3\\_20](http://dx.doi.org/10.1007/978-3-319-67774-3_20)
- McDowell, F. W., McIntosh, W. C., Farley, K. A., 2005. A precise 40Ar–39Ar reference age for the Durango apatite (U–Th)/He and fission-track dating standard. *Chemical Geology*, 214(3-4), 249-263. <https://doi.org/10.1016/j.chemgeo.2004.10.002>
- McPhie, J., Doyle M, Allen, R.L., 1993. Volcanic textures: a guide to the interpretation of textures in volcanic rocks. University of Tasmania. 196 pp.
- Navarrete, C., Gianni, G., Encinas, A., Márquez, M., Kamerbeek, Y., Valle, M., Folguera, A. 2019. Triassic to Middle Jurassic geodynamic evolution of southwestern Gondwana: From a large flat-slab to mantle plume suction in a rollback subduction setting. *Earth-science reviews*, 194, p. 125-159. <https://doi.org/10.1016/j.earscirev.2019.05.002>
- Orgeira, M. J., Remesal, M., 1993. Estudio paleomagnético del Complejo Volcánico de Somuncura, Argentina. *Rev. Asoc. Geol. Argentina*, 48, p. 257-264.
- Orts, D., Folguera, A., Giménez, M., Ruiz, F., Rojas Vera, E., Lince Klinger, F., 2015. Cenozoic building and deformational processes in the north Patagonian Andes. *J. Geodyn.* 86, 26–41. <https://doi.org/10.1016/j.jog.2015.02.002>
- Ramos, V., Kay, S.M., 1992. Southern Patagonian plateau basalts and deformation: back-arc testimony of ridge collision. *Tectonophysics* 205, 261–282. [https://doi.org/10.1016/0040-1951\(92\)90430-E](https://doi.org/10.1016/0040-1951(92)90430-E)
- Remesal, M. B., 1988. Geología y petrología de los basaltos de la Meseta de Somuncurá (Doctoral dissertation, Universidad de Buenos Aires. Facultad de Ciencias Exactas y Naturales).
- Remesal, M., Salani, F. M., Massaferro, G. I., Cerredo, M. E., 2004. Stratigraphy and petrology of the Northeastern sector of Sierra de Apas. Chubut Province. *Revista de la Asociacion Geologica Argentina*, 59(4), 578-590.
- Salani, F. M., Remesal, M., Cordenons, P.D., Cerrado, M.E., 2022. El magmatismo de Somún Curá en la Provincia del Chubut. *Actas del XXI Congreso Geológico Argentino*: 430-456.
- Santonja, C., Bechis, F., Suriano, J., Falco, J. I., Encinas, A., Olaizola, E. R., Valencia, V. A., Litvak, V. D., Ramos, V. A., 2021. Tectono-stratigraphic evolution of the northeastern sector of the Nirihuau basin, North Patagonian Andes, Argentina: Insights from sedimentology and geochronology data of the Nirihuau Formation.

Journal of South American Earth Sciences, 111, 103487.  
<https://doi.org/10.1016/j.jsames.2021.103487>

Tchamabé, B. C., Ohba, T., Keresztri, G., Németh, K., Aka, F. T., Youmen, D., Issa, Miyabuchi, Y., Ooki, S., Tanyileke, G., Hell, J. V., 2015. Towards the reconstruction of the shallow plumbing system of the Barombi Mbo Maar (Cameroon) Implications for diatreme growth processes of a polygenetic maar volcano. Journal of Volcanology and Geothermal Research, 301, 293-313.  
<https://doi.org/10.1016/j.jvolgeores.2015.06.004>.

Vermeesch, P., 2018. IsoplotR: A free and open toolbox for geochronology. Geoscience Frontiers, 9(5), 1479-1493. <https://doi.org/10.1016/j.gsf.2018.04.001>

White, J. C., Espejel-García, V. V., Anthony, E. Y., and Omenda, P, 2012. Open system evolution of peralkaline trachyte and phonolite from the Suswa volcano, Kenya rift. Lithos, 152, 84-104. <https://doi.org/10.1016/j.lithos.2012.01.023>

## APÊNDICE B - Artigo 2

### *Volcanic evolution of the Sierra de Apas: the influence of mantle plume and subduction in the Somuncurá Magmatic Province, Patagonia, Argentina*

Gilmar Pachá Corrêa dos Santos da Silva<sup>1</sup>, Anderson Costa dos Santos<sup>1,2</sup>, Leonardo Benedini<sup>3,4</sup>, Eduardo Reis Vianna Rocha-Júnior<sup>5</sup>, Guilherme Gonçalves<sup>6</sup>, Cecília Pavón Pivetta<sup>3,4</sup>, Mauro Geraldès<sup>1</sup>, Daniel Gregori<sup>3,4</sup>, Tiago Jalowitzki<sup>6</sup>, Julio Mendes<sup>7</sup>

<sup>1</sup>Universidade do Estado do Rio de Janeiro (UERJ), Faculdade de Geologia (UERJ), Departamento de Mineralogia e Petrologia Ígnea (DMPI). São Francisco Xavier Street, 524 – 4033A, 20550-900, Rio de Janeiro (RJ), Brazil;

<sup>2</sup>Tektos Group and GeoAtlântico Institute (UERJ)/Geobiotec, Departamento de Geociências, Universidade de Aveiro, 3810-193;

<sup>3</sup>Dpto. de Geología, Universidad Nacional del Sur (UNS), Bahía Blanca, Argentina;

<sup>4</sup>Instituto Geológico del Sur (INGEOSUR), Universidad Nacional del Sur (UNS)-CONICET, Bahía Blanca, Argentina;

<sup>5</sup>Universidade Federal da Bahia (UFBA), Instituto de Física, Departamento de Física da Terra e do Meio Ambiente. Rua Barão de Jeremoabo, s/n, 40170-115, Salvador (BA);

<sup>6</sup>Universidade de Brasília, Instituto de Geociências, Programa de Pós-Graduação em Geologia, Brasília, Distrito Federal, Brazil;

<sup>7</sup>Universidade Federal do Rio de Janeiro, Instituto de Geociências, Departamento de Geologia. Av. Athos da Silveira Ramos, 274, 21941-916, Rio de Janeiro (RJ), Brasil. Orcid: 0000-0002-4332-8802.

#### Abstract

The Somuncurá Magmatic Province (SCMP) consists of a sequence of volcanic deposits that formed in the northern part of Argentina during the Neogene. The deposits are characterized into six lithofacies: massive trachyte, trachyte with flow banding, tuff, commendite with flow banding, vesicular basalt, and gabbro. Furthermore, the study included two U-Pb geochronological analyses in apatites from trachytic samples, with an average of  $26.19 \pm 1.54$  Ma. and seven  $^{147}\text{Sm}/^{144}\text{Nd}$  isotopic analyses. Results indicated  $^{147}\text{Sm}/^{144}\text{Nd(m)}$  ratios of 0.1390 for the gabbro, 0.1369 for the trachyte, and 0.1009 for the commendite, as well as  $^{87}\text{Sr}/^{86}\text{Sr(m)}$  ratios of 0.900385 for the commendite and 0.704059 for the gabbro, both in total rock., where intermediate rocks are noticeably lacking. Moreover, the presence of negative alkaline tendency identified in the rocks under investigation is a distinctive feature in places characterized by bimodal magmatism ( $\text{SiO}_2$  43.1 - 77.4%), anomalies of Sr, Ba, and P in the acidic rocks, alongside the positive anomaly of Zr in the commendites, further contributing to the complexity of the geochemical patterns observed. Furthermore, the placement of basic rocks near Ocean Island Basalts

(OIB) in tectonic interpretation and provenance diagrams, as opposed to acidic rocks within the region of crustal contamination, illustrates the variety of geological processes. The Sierra de Apas is an intriguing example of intraplate magmatism affected by subduction processes. The geochemical and isotopic data suggest significant subduction-related influences, especially through incorporating sediments from the subduction in the Chile Trench. These sediments contribute to the mantle source and modify the composition of the magmas, leading to hybrid geochemical signatures.

**Keywords:** Alkaline magmatism; Bimodal magmatism; Intraplate magmatism; Fractional crystallization; Magmatic evolution

## 1 INTRODUCTION

The Somuncurá Magmatic Province (SCMP), formed during the transitional period between the Oligocene and Miocene, represents one of the most extensive back-arc mafic volcanic fields on Earth and the largest in Patagonia, Argentina, covering an area of approximately 50,000 km<sup>2</sup> (Fig. 1). The lack of a strong correlation with Andean subduction, hotspot, and metasomatism is a defining feature of the basaltic plateau (Navarrete *et al.* 2020), since the Somuncurá Formation, composed of olivine basalts (Ardolino 1981; Ardolino & Franchi 1993), constitutes one basaltic plateau. Local thermal instability in the mantle was initially considered to contribute to the formation of these basalts (Kay *et al.* 1992, 1993a).

In the back-arc region, magmatism can be associated with subduction zones, presenting compositions and physical properties different from arc magmatism. The thinning of the lithosphere, in conjunction with extensional forces, facilitates mantle upwelling. The geochemistry of back-arc magmas exhibits a subduction signature when analyzing trace elements and water content (Pearce and Stern, 2006). It is crucial to consider the effects of changes in subduction dynamics, possible plate rotation, rupture, and their association with mantle flow (Magni, 2019).

The historical context of the Nazca-South American plates plays a crucial role in understanding the evolution of the PMSC. Following the rupture of the Farallon plate into the Nazca, Cocos, and Juan de Fuca plates between 26-28 Ma (Herron and Heitzler, 1967), the convergence rate of the Nazca plate with the South American plate increased from 5-6 cm/year to 14 cm/year between latitudes 37°-42°S (Cordenons, 2017). This process of plate reorganization, with changes in

subduction angle and speeds, is intrinsically linked to the magmatism that occurred during the Oligo-Miocene period (De Ignacio et al. 2001).

Since the late 19<sup>th</sup> and early 20<sup>th</sup> centuries, the area has been the subject of research, e.g., de Doering (1882), Ameghino (1898), and Windhausen (1921). During the last 30 years, some authors carried out morphological, petrological, and tectonic studies related to the plateau development, such as Remesal et al. (1996); Franchi et al. (1998); Busteros et al. (1998); Caminos (1999); Remesal et al. (1999); Cucchi et al. (1999); De Ignacio et al. (2001); Kay et al. (2007); Remesal et al. (2012); Navarrete et al. (2020). Other authors, such as Flores (1956 and 1957), Nakayama (1975), Corbella and Linares (1977), conducted studies recognizing and dating new units in the region.

Initially, the volcanic flows were considered to have developed between 33 and 17 Ma (Ardolino and Franchi 1993). Based on this period, the significant volcanic eruptions began around 33 Ma, during the Oligocene. In general, there are two primary peaks in the plateau igneous activity: one occurred between 33 and 31 Ma, while the other occurred between 27 and 25 Ma, according to <sup>40</sup>K/<sup>40</sup>Ar dating (Ardolino, 1981). Subsequently, an event that included significant alkaline magmatism occurred following the basaltic plateau's formation during the Miocene.

The alkaline complexes (Kay et al. 2007) represent some of the effusive expressions that emerged following the basaltic plateau. Silicic volcanic rocks temporally and spatially related to the mafic lavas include trachytic to comenditic rhyolite, domes, tuffs, and subvolcanic intrusive rocks (Navarrete et al. 2020). These include the *Sierra de Apas*, *Sierra de Telsen*, *Sierra de Talagapa*, *Alta Sierra de Somuncurá*, and *Sierra de Chacays*. Comprising minor, more differentiated intrusions and a collection of subsaturated alkaline basic rocks, they often form expansive, widely distributed polygenetic volcanic systems (Corbella 1982).

Franchi (1998) proposed that the alkaline volcanic complexes, primarily from the Miocene, belong to the *Quiñelaf* Super Unit. These volcanic rocks range between  $37 \pm 2$  Ma and  $11 \pm 2$  Ma, suggesting the possibility of stratigraphic inconsistencies. While basic and subvolcanic lavas originated from the Miocene ( $23 \pm 2$  Ma and  $15 \pm 1$  Ma; Ardolino 1981), intermediate lavas commonly fill a portion of the Oligocene (Franchi and Sepúlveda 1983).

The most recent trachytic effusions were found in *Sierra Negra de Telsen* and *Sierra de los Chacays*, with ages similar to the previous ones (  $22 \pm 2$  Ma;  $19.3 \pm 3$

Ma and  $18 \pm 2$  Ma; Yllañez and Lema (1979); Barbieri and Corbella (1987). Finally, in the middle Miocene, late manifestations with the intrusion of trachytic subvolcanic bodies aged  $12 \pm 1$  Ma and  $11 \pm 2$  Ma occurred in the *Alta Sierra de Somuncurá* (Ardolino and Franchi 1993).

Few projects have studied the *Sierra de Apas* region, and the lack of data on magmatic evolution and the connections between different igneous rock types underscores the need for detailed studies of these volcanic formations.

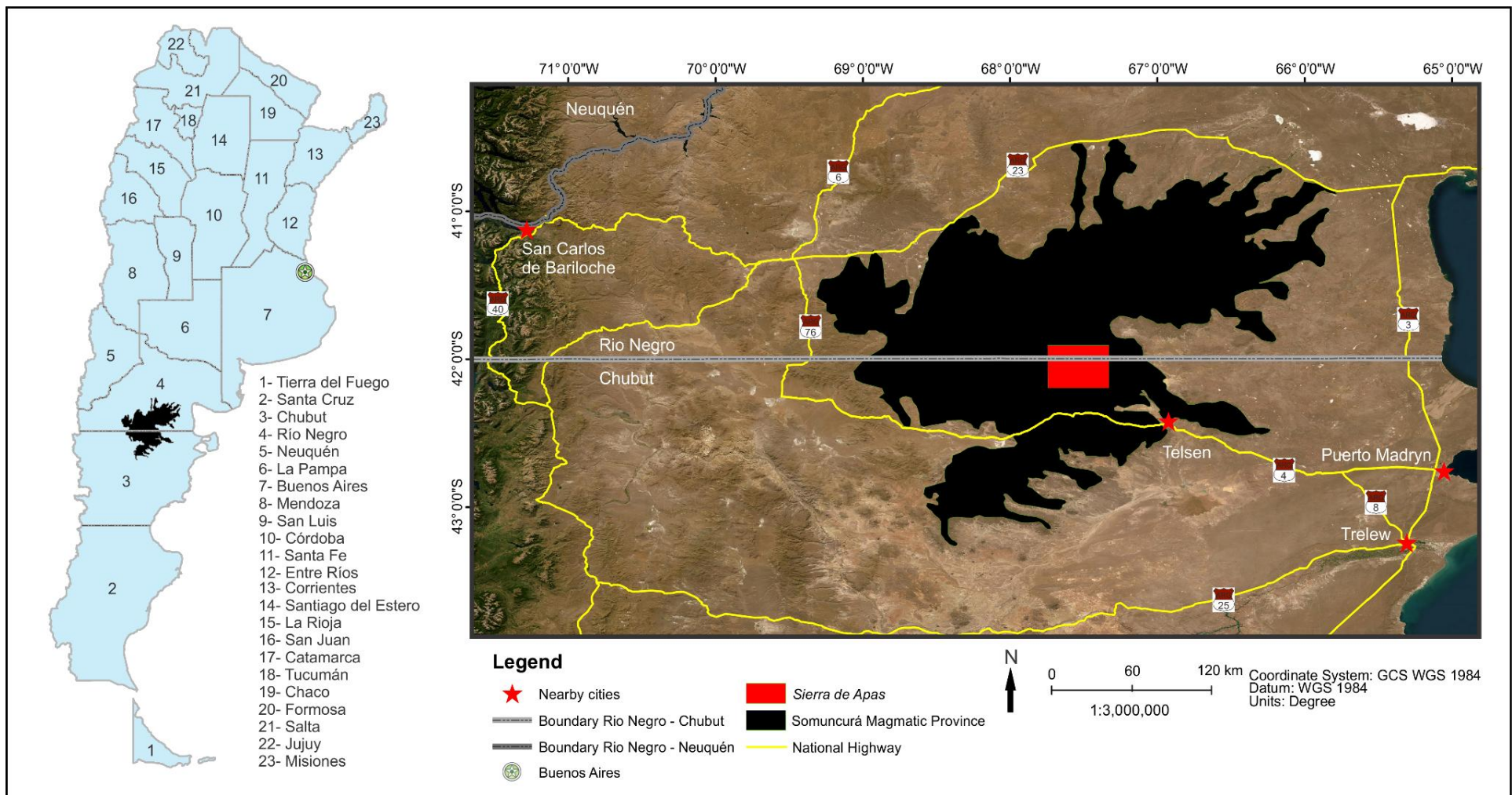


Figure 1- Location map indicating the Somuncurá Magmatic Province (black), where the *Sierra de Apas*, Argentina, is located (red), as well as the national highways in yellow (lines) and the nearby cities (colored stars).

## 2 GEOLOGICAL FRAMEWORK

### 2.1 Location

The Somuncurá Magmatic Province (SCMP) is situated in the center and southern regions of Río Negro, Argentina, and extends to the northwest and center of Chubut province. Situated between  $40^{\circ}30'$ -  $43^{\circ}20'$ S and  $65^{\circ}50'$ -  $70^{\circ}30'$ W (Figure 1), this geological province gets its name from the most extensive basaltic effusion, known as the Somuncurá Formation (Ardolino et al. 2008). Approximately 25,000 km<sup>2</sup> of basaltic rocks, overlain by younger effusions, are located 500-800 km from the active margin of Nazca, South America (Cordenons et al. 2020). These sets of *sierras* include *Alta de Somuncurá*, *Apas*, *Chacays*, *Negra de Telsen*, and *Talagapa*.

The research region for this study, the *Sierra de Apas*, is situated between parallels  $67^{\circ}45'$  and  $67^{\circ}20'$  W and  $41^{\circ}55'$  and  $42^{\circ}15'$  S, between the Provinces of *Río Negro* and *Chubut*.

The closest community to the study area is *Telsen*, which is around 60 kilometers distant. The nearest cities to *Telsen* are 170 km from *Puerto Madryn* and 180 km from *Trelew*. *Puerto Madryn*, *San Carlos de Bariloche*, *Telsen*, and *Trelew* are the main cities in the region accessed by national roads 3, 6, and 40 and provincial routes 4, 8, 23, and 25 that pass through the provinces of *Chubut* and *Río Negro*, close to the SCMP (Figure 1).

### 2.2 Pre-Mesozoic basement

Patagonia's complex geology is characterized by various diverse geological processes that have produced a wide range of lithologies over a long period. Studying the area's basement is necessary to better understand the SCMP's geology. Northern Patagonia's tectonic and geological development is summarized in Table 1.

According to Von Gosen (2003), the lithologies that constitute the Neoproterozoic sequence, with the Pampean Orogeny (Ediacaran—Cambrian), correspond to the *Complejo El Jaquérito* Formation, a metasedimentary unit made up of metapelites and shales that developed in a marine environment.

The PMSC's paleozoic basement consists of igneous and metamorphic rocks from the Precambrian to the Lower Jurassic. Nuñez et al. (1975), Ramos (1975), and Llambias et al. (1984) describe an intense orogenic plutonism with tonalitic and granitic rocks associated with intense regional metamorphism of Precambrian to Lower Paleozoic ages, with events associated with the Famatinian cycle.

The oldest records of this cycle consist of scarce granites and type I granodiorites of Ordovician age attributed to the *Punta Sierra* Plutonic Complex. The Paleogene is also marked by the permanence of the sea in the region, whose records are the beach sediments formed by large quantities of calcareous marine organisms, coarse sands, and some clays, corresponding to the *Sierra Grande* and *Roca* Formation. The earliest successions are covered mainly by Tertiary, Jurassic, and Triassic volcanoes (Von Gosen 2003).

The Gondwana Cycle is mainly represented by non-foliated type I granites and foliated type S granites. Both types of igneous bodies are associated with the Gondwana Orogeny, one of the most widespread Paleozoic orogenies in the Patagonian region during the Permian period.

The development of these rocks and their generation of tectonics are the subject of discussions, interpretations, and doubts. Several authors have hypothesized that Patagonia is a paleocontinent, including Windhausen (1931), who thought of the Patagonian massif as a Patagonian-Antarctic continent, and Nur and Ben Avraham (1977) and Ben Avraham (1981), who proposed that the various parts of South America have distinct origins.

Ramos (1984) suggested that the active Patagonian margin and the passive Gondwana margin bring together a large amount of evidence, with Patagonia being a drifting continent until it collided with Gondwana. Nevertheless, the lack of further evidence on the location, such as suture zones, is a problem for validating allochthonous Patagonia.

Table 1 - Synthesis of Proterozoic, Paleozoic, and Mesozoic tectonic events in the PMSC basement.

Era	Period	Event	Formation	Lithology
Mesozoic	Lower Jurassic	Beginning of break-up	<i>Marifil</i> Formation	<i>Coulées</i> , breccia and tuff
	Upper Triassic	Beginning of extensional tectonic		
Paleozoic	Permian	Gondwanan orogeny		Types I and S Granite
	Carboniferous			
	Upper Devonian		<i>Sierra Grande</i> Formation	Marine sediments
	Silurian	Famatinian Cycle		
	Ordovician		<i>Punta Sierra</i> Plutonic Complex	Granodiorite and type I granites
Neo-Proterozoic	Cambrian			
	Ediacaran	Pampean Orogeny	<i>El Jaquielito</i> Complex	Metapelites and shales

### 2.3 Mesozoic basement

After the Gondwanan orogeny, significant extensional effusions, which heralded the opening of the Atlantic Ocean, affected the basement and formed a depressed region or intracontinental basin named the *Somuncurá Canadón Asfalto*. The rifting began, governed by multiple and polyphase episodes of orogenic deformation that affected southern South America (Navarrete et al. 2019).

The basin was mainly filled by volcanic rocks of different compositions, from the Upper Triassic to the Middle Jurassic. It was grouped into various units such as the *Los Menucos* and *Marifil* Volcanic Complex, the *Garamilla* Formation and the *Lonco Trapial* Group (Figari et al. 2005).

According to Pavón Pivetta et al. (2020), the deformational system of Gondwana that began in the upper Triassic directly influenced Jurassic volcanism in the region. The author divides magmatism in the region into two stages. The first stage was conditioned by normal east-west faults that connected the magma chamber to the surface, with typical Plinian volcanism, with *coulée* structures and lithologies such as breccia and lapilli tuff, present in six lithofacies, numbered I to VI, with lithofacies II zircon dated at  $192.6 \pm 2.5$  Ma.

The second stage, related to large eruptive centers, with voluminous volcanism, ignimbrite with rhyolitic composition, massive tuff lapilli, and rhyolites, similar to Snake River type volcanism. In the Upper Jurassic, lacustrine and fluvial environments were established with the accumulation of sediments interspersed with basaltic lavas; this group is known as the *Cañadón Asfalto* Formation (Silva Nieto et al. 2003). Following the stratigraphic column, the Cretaceous is marked by the *Chubut* Group, made up of sediments of fluvial origin with volcanic ash, containing abundant dinosaur fossils and tree trunks. Environmental conditions changed in the upper Cretaceous, and the region was flooded by the sea, and pelitic sediments accumulated on the bed covering the rocks of the *Chubut* Group, giving rise to the *La Colonia*, *Los Alamitos*, *Puntudo Chico*, and *Coli Toro* Formations.

Table 2 - Synthesis of the formation of the Somuncurá Magmatic Province (PMSC) and the Mesozoic basement.

Era	Period	Epoch	Formation	
Cenozoic	Neogene	Miocene	Upper	Quinelaaf Superunit
			Medium	
			Lower	
	Oligocene		Upper	
			Medium	
			Lower	
	Paleogene		Sarmiento Group	
		Eocene	Medium	
			Upper	
	Mesozoic	Paleocene	Lower	
		Cretaceous	Upper	
			Fm. La Colonia	
		Medium	Fm. Puntudo Chico	
		Lower	Chubut Group	

## 2.4 Somuncurá Magmatic Province - A Cenozoic magmatism

During the Eocene, the region of the Somuncurá Magmatic Province suffered its last flood, so all subsequent volcanic processes developed over the continent at an altitude close to sea level. During the Oligocene and Miocene, the region experienced volcanism, with thick layers of whitish volcanic ash from Andean volcanism, known as the *Sarmiento* Formation. Environmental changes were marked by the development of numerous mammal species and ash deposits.

Simultaneously with this volcanism, extensive basaltic lava flows slowly interspersed with the ash layers completely covered by the basaltic lavas. These lavas form the upper part of the *Somuncurá* Plateau. The thickness of the basaltic effusion is variable, with layers of 20 to 30 meters at the edges.

Trachytic and rhyolitic effusions were found in more restricted regions, which currently comprise the highland zones, the highest areas within the plateau.

At the end of the Neogene, upward movements elevated much of Patagonia, exposing a large part of the *Somuncurá Cañadón Asfalto* Basin to erosion. The units and formations covered by the basaltic rocks were slowly eroded, producing relief inversion.

The lithologies of *Sierra de Apas*, included in the Oligocene and Miocene volcanism, are described in the earliest geological papers as predominantly trachytic with subordinate trachybasalt and basalts, according to the region's earliest geological references (Croce 1963). Studies which include the presence of subvolcanic intrusives, a radial network of peralkaline trachytic dikes, and the peralkaline characterization of the association of basalts, trachytes, and rhyolites that constitute the *Apas* increase knowledge (Corbella 1975; Corbella and Linares 1977). A comprehensive investigation of the *Somuncurá* massif was conducted by Remesal (1988, 1996), with petrological and stratigraphic research. Surveys of the *Telsen* (Ardolino and Franchi 1996), *Cona Niyeu* (Franchi et al. 2001), and *Maquinchao* (Remesal et al. 2001) geological maps contain regional works that involve partial studies of the *Sierra de Apas*.

The source of the Oligocene-middle Miocene magmatism, which produced the biggest and most abundant volcanic phases, continued to be particularly interesting. However, local and regional stratigraphic evaluations fail to consider the complexity of the involved volcanic systems or their stratigraphy. Numerous observations center on the *Somuncurá* basalts and correlative units, yet the region's monogenetic eruption evidence and the Quaternary magmatism of north-central Patagonia are still mysterious.

The origin of the igneous activity in north-central Patagonia during the Oligocene and middle Miocene has been explained by many different mechanisms in previous studies. These include i) the interaction between a mantle plume and the Aluk oceanic plate (Kay et al. 2007); ii) the ascent of the mantle transition zone caused by a decrease in the subduction angle and/or the convergence rate (Honda

et al. 2006; Orihashi et al. 2006, 2010); iii) a potential break-off of the Farallon-Nazca slab and following strong steepening of the Nazca slab (De Ignacio et al. 2001); and iv) lithospheric delamination (Remesal et al. 2012).

Since slab-derived components have been identified in the petrogenesis of these intraplate rocks, according to geochemical evidence (e.g., Kay et al. 2007), these hypotheses have attempted to explain the significance of subduction-derived fluids.

Nevertheless, there is limited geologic data to support these theories. Both the evidence for high mantle potential temperatures related to the presence of a thermal anomaly (ca. 1,100–1,405 °C for the Oligocene-middle Miocene magmatism, according to Menegatti et al. 2018) and a volcanic hotspot track resulting from the continent's migration over the stationary mantle plume do not exist (e.g., Condie, 2001; Ernst and Buchan, 2003; O'Connor et al. 2017; Harrison et al. 2017).

In terms of the changes in slab angle and convergence rate, there would have been a simultaneous slab steepening event (Encinas et al. 2016; Fernández Paz et al. 2019) and a sudden increase in the last one in the late Oligocene-early Miocene (Eagles and Scott 2014). No geophysical evidence of the Oligocene-middle Miocene slab gap is relevant to the slab break-off and subsequent slab rising concept (Aragón et al. 2011a; Van der Meer et al. 2018).

Finally, there is no geological proof of an intraplate pre-Oligocene shortening event that would have enabled the crust to reach a sufficient thickness (ca. 50 km; Kay 1993) to convert to eclogite the crust's mafic base and cause the Patagonian delamination that Remesal et al. (2012) hypothesized. In addition to the mentioned considerations, these hypotheses did not consider the several outcrops of Oligocene-middle Miocene basalts in southern Patagonia, which suggests that the genetic process of these magmas had to be larger-scale.

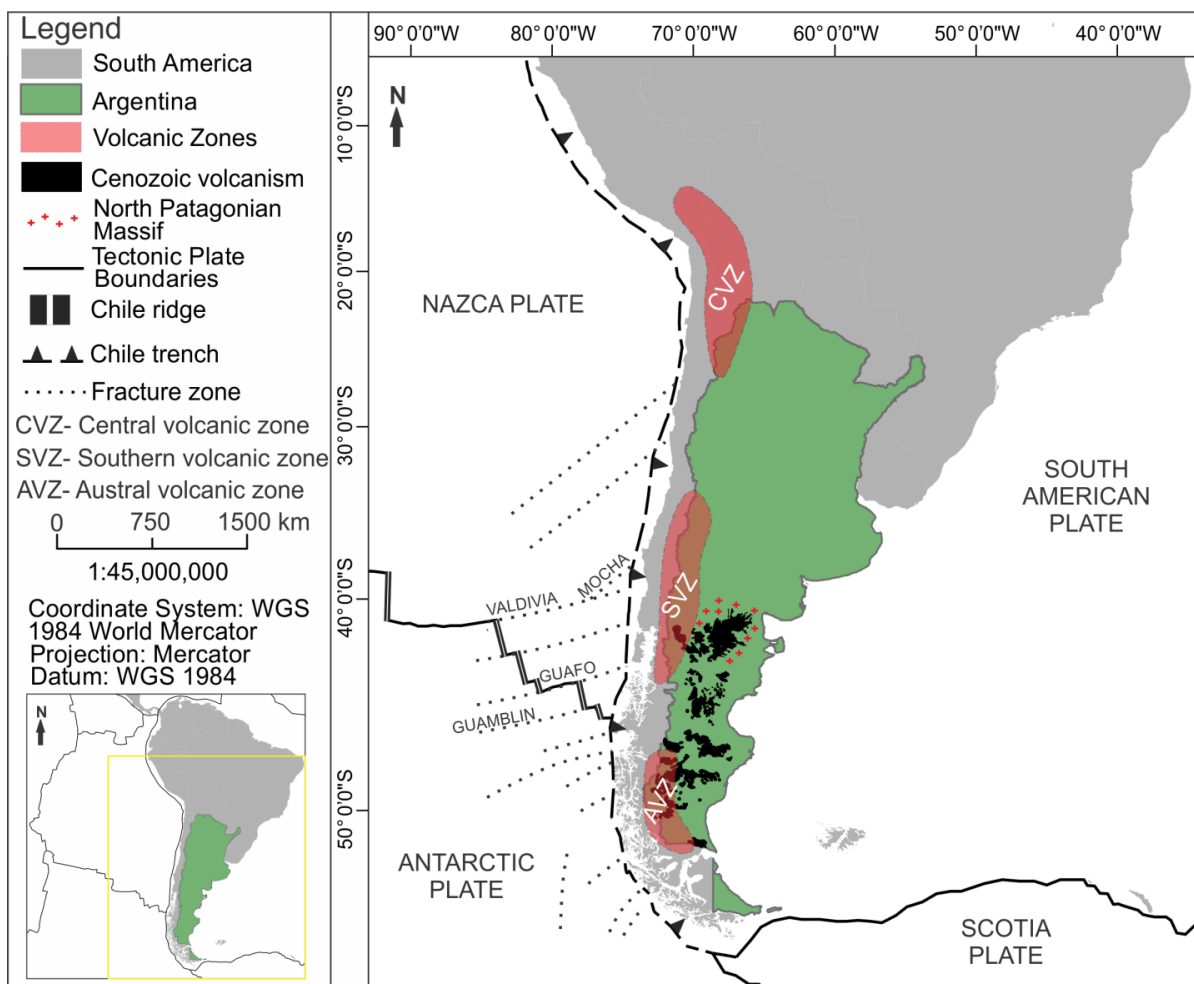


Figure 2 - Map showing the location of the main Cenozoic magmatism and the magmatic zones of Argentinian Patagonia.

### 3 MATERIALS AND METHODS

Representative samples were collected during the field trip to classify, interpret, and analyze the different lithotypes found in the *Sierra de Apas*. This detailed process is fundamental to comprehensively understanding the region's geology, providing solid and direct dates for subsequent analyses.

The lithologies were then recognized and prepared at the *Laboratório Geológico de Processamento de Amostras* (LGPA) at the Universidade do Estado do Rio de Janeiro (UERJ).

The lithofacies coding of volcanic facies was elaborated considering Branney and Kokelaar (2002) and McPhie (1993) criteria, whereas, for sedimentary rocks, we follow the bases described by Miall (1996). The lithofacies were grouped in

facies associations, corresponding to a group of facies genetically associated with environmental implications.

For the petrographic analysis, twenty-four thin sections were produced, and twenty-three samples were submitted for lithogeochemical analysis of major and trace elements in the whole rock. These samples were crushed on an anvil and then processed in a tungsten ball mill, resulting in a fine powder. The samples were then sent to the Australian Laboratory Services (ALS) laboratory. The significant elements,  $\text{SiO}_2$ ,  $\text{TiO}_2$ ,  $\text{Al}_2\text{O}_3$ ,  $\text{Fe}_2\text{O}_3\text{t}$ ,  $\text{MnO}$ ,  $\text{MgO}$ ,  $\text{CaO}$ ,  $\text{Na}_2\text{O}$ ,  $\text{K}_2\text{O}$ , and  $\text{P}_2\text{O}_5$ , were measured as oxides in weight percent (wt. %) using Inductively Coupled Plasma Atomic Emission Spectrometry (ICP-AES). The trace elements Cr, V, Ba, Rb, Sr, Y, Nb, Zr, Hf, Ta, U, Th, and the rare earth elements were measured in parts per million (ppm) using the Inductively Coupled Plasma Mass Spectrometry (ICP-MS) method.

In addition, electron microprobe investigations were conducted using the thin sections at the *Laboratório de Microssonda Eletrônica - Labsonda* at the *Universidade Federal do Rio de Janeiro* (UFRJ). The samples were metalized in the Jeol Jee - 420 Vacuum Evaporator, and the Joel JXA - 8230 Electron Probe Microanalyzer was used to test and obtain the results. The analyses performed at LabSonda had the analytical conditions of 15 KeV voltage, 20 nA filament current, and 1 mm diameter beam. Sanidine, olivine, clinopyroxene, magnetite, and ilmenite were the reference minerals used in the quantitative analyses.

Two samples were treated in parallel for U-Pb geochronological investigation. Apatite and rare zircons were confirmed in the samples via SEM-EDS at CETEM, and mounts were prepared at MultiLab-UERJ. U-Pb data were collected at *Laboratório de Estudos Geodinâmicos, Geocronológicos e Ambientais* at *Universidade de Brasília* (UNB) using a Thermo Finningan Element XT ICP-MS with laser ablation. Masses of interest ( $202\text{Pb}$ ,  $204\text{Pb}$ ,  $206\text{-}208\text{Pb}$ ,  $232\text{U}$ ,  $238\text{U}$ ) were measured simultaneously. Laser conditions were set at a spot diameter of 65  $\mu\text{m}$ , 20 Hz, and  $7.5 \text{ J cm}^{-2}$ . Data processing utilized Iolite 4.0 (Paton et al. 2011) for time-resolved signal and VizualAge for individual signal inspection. UComPbine DRS was employed for data reduction, accounting for variable initial lead on the calibrant (Chew et al. 2014). Corrections included blank subtraction, downhole correction, and normalization by Durango apatite (Chew et al. 2011; McDowell et al. 2005). The initial lead for data anchoring was 0.835 (Chew et al. 2011). Sumé

apatite (Lana et al. 2022) was used for quality control. Systematic uncertainty of ca. 1% was propagated on each final age, and ages are quoted at 2s. No common lead correction was applied.

The isotopic compositions of Sr and Nd were carried out in seven samples of total rock powder at the *Laboratório de Geocronologia e Isótopos Radiogênicos* (LAGIR) - UERJ. This investigation employed the TRITON multi-collector thermal ionization mass spectrometer (TIMS). The normalized isotope ratios were  $^{88}\text{Sr}/^{86}\text{Sr} = 8.3752$ ,  $^{147}\text{Sm}/^{152}\text{Sm} = 0.5608$ , and  $^{146}\text{Nd}/^{144}\text{Nd} = 0.7219$ . Throughout the study, investigations of the standard reference materials JNd-1 ( $n = 214$ ; Tanaka et al., 2000) and NBS-987 (NIST) ( $n = 140$ ) produced averages of  $0.710239 \pm 0.000007$  ( $2\sigma$ ) for  $^{87}\text{Sr}/^{86}\text{Sr}$  and  $0.512100 \pm 0.000006$  ( $2\sigma$ ) for  $^{143}\text{Nd}/^{144}\text{Nd}$  (Valeriano et al. 2009; Neto et al. 2009). After conducting several investigations on NBS-987 (NIST), the average ratio of  $^{87}\text{Sr}$  to  $^{86}\text{Sr}$  was determined to be  $0.706012 \pm 0.000009$  ( $2\sigma$ ). Less than 70 pg and 200 pg, respectively, are the analytical blanks for Sm and Nd, whereas the Sr value was not established. These measurements provide the framework for comprehending the relevant geological processes.

## 4 RESULTS

### 4.1 Facies Description

The descriptions of volcanic facies were classified into seven lithofacies and interpreted as five volcanic units. All the samples analyzed were classified using this interpretation (Table 3). The distribution of the volcanic facies is presented in Figure 3.

Table 3 - Classification of samples according to lithofacies and interpretation.

Number	Lithofacies	Samples	Interpretation
1	Porphyritic medium to coarse grained massive trachyte	CAP 05, CAP 26, CAP 31, CAP 40	
	Porphyritic flow-banded trachyte	CAP 13 A, CAP 15	1, 2 and 3-Trachyte coulees, lava
	Fine grained massive dark-coloured obsidian trachyte	CAP 54	domes, lavas and dikes
2	Monomictic massive trachyte breccia		
3	Fine grained well-sorted massive tuff	CAP 08 A	
	Juvenile-rich well-sorted massive to parallel bedded lapilli	CAP 45	4- PDCs deposits
	Moderately sorted with directional fabric massive lapilli-tuff	CAP 11	
5	Monomictic Jigsaw-fit commendite breccia	CAP 57A	
	Flow-banded microgranular commendite	CAP 18, CAP 19 CAP 53, CAP 55A, CAP 56 C	5- Commenditic lava-dome
	Massive to flow banded vesiculated olivine basalts	CAP 06, CAP 38	6- Basaltic mesa lava flows
7	Fine grained massive gabbro/diabase	CAP 14, CAP 39A, CAP 41, CAP 42	7- Subvolcanic bodies

#### 4.1.1 Trachytic lavas and coulées lavas

The Sierra de Apas primarily comprises coulées and lava flows, which form its most significant geological features. This facies comprises a series of polycyclic effusions, including seven distinct flows. The individual coulées range from 20 to 80 meters thick and typically exhibit slight profile asymmetry. Notable characteristics include the development of convex, curved crests along the flow direction, frequent folding of the flow banding, and the common occurrence of columnar jointing.

#### 4.1.2 Trachytic lava domes

Trachytic lava domes display a significant morphological difference from coulées despite being mostly made up of the same lithofacies. These domes vary in shape and relative abundance. They are typically sub-circular in plan view and

slightly elongated in the N 30° direction, predominantly featuring coherent lithofacies.

#### *4.1.3 PDCs deposits*

Three main lithofacies primarily represent pyroclastic levels in the Sierra de Apas. These levels are generally discrete and thin (5 to 80 meters thick), interbedded within lower effusive sequences. Their limited development indicates the predominance of effusive volcanic stages over eruptions associated with magmatic fragmentation. The lateral continuity of these deposits is often poor, making it challenging to trace associated outcrops.

These deposits commonly exhibit normal grading and contain variable concentrations of volcanic fragments: 8-17% free crystals, 49-67% pumice, and glass fragments, and very low concentrations of lithic fragments (1-5%). Both tuff and lapilli display a distinct vitroclastic texture characterized by glass fragments and vesiculated pumice. Field observations have documented syn-depositional deformation, including small local faults that form negative flower structures, displacing tuff layers without altering the overlying sequence.

#### *4.1.4 Commenditic lava domes*

Cerro Colorado represents these lithofacies in the northeasternmost part of the Sierra de Apas. This geological feature has an elliptical shape (with axes measuring 3 km and 2 km) elongated east-west. The dome primarily comprises gray rocks exhibiting prominent banding indicative of fluidity. Alkali feldspar is the dominant mineral, varying in size and contributing to a foliated texture.

#### *4.1.5 Basaltic lava flow*

The rocks are predominantly gray, exhibiting various oxidation levels and a variable proportion of phenocrysts. Typically, the ratio of phenocrysts to matrices is around 30/70, although this ratio decreases notably in some varieties (15/85).

Phenocrysts, sized between 0.5 to 2 cm, include iddingitized e olivine (easily identifiable even in hand samples), clinopyroxene, and plagioclase, sometimes forming clusters known as glomeruli. These phenocrysts often show signs of corrosion, indicating disequilibrium with the surrounding magma. Specifically, the lava flows overlaying the light-colored trachyte flows north of Contreras post comprise 20-25% olivine phenocrysts, ranging in size to microliths embedded within the matrix.

#### *4.1.6 Gabbro dikes and subvolcanic bodies*

The alkaline gabbro dikes are considered the final volcanic phases of the system, with approximately 400 meters along the strike, presenting a 60-meter thickness. The gabbros are characterized by their massive medium- to fine-grained texture and moderate jointing.

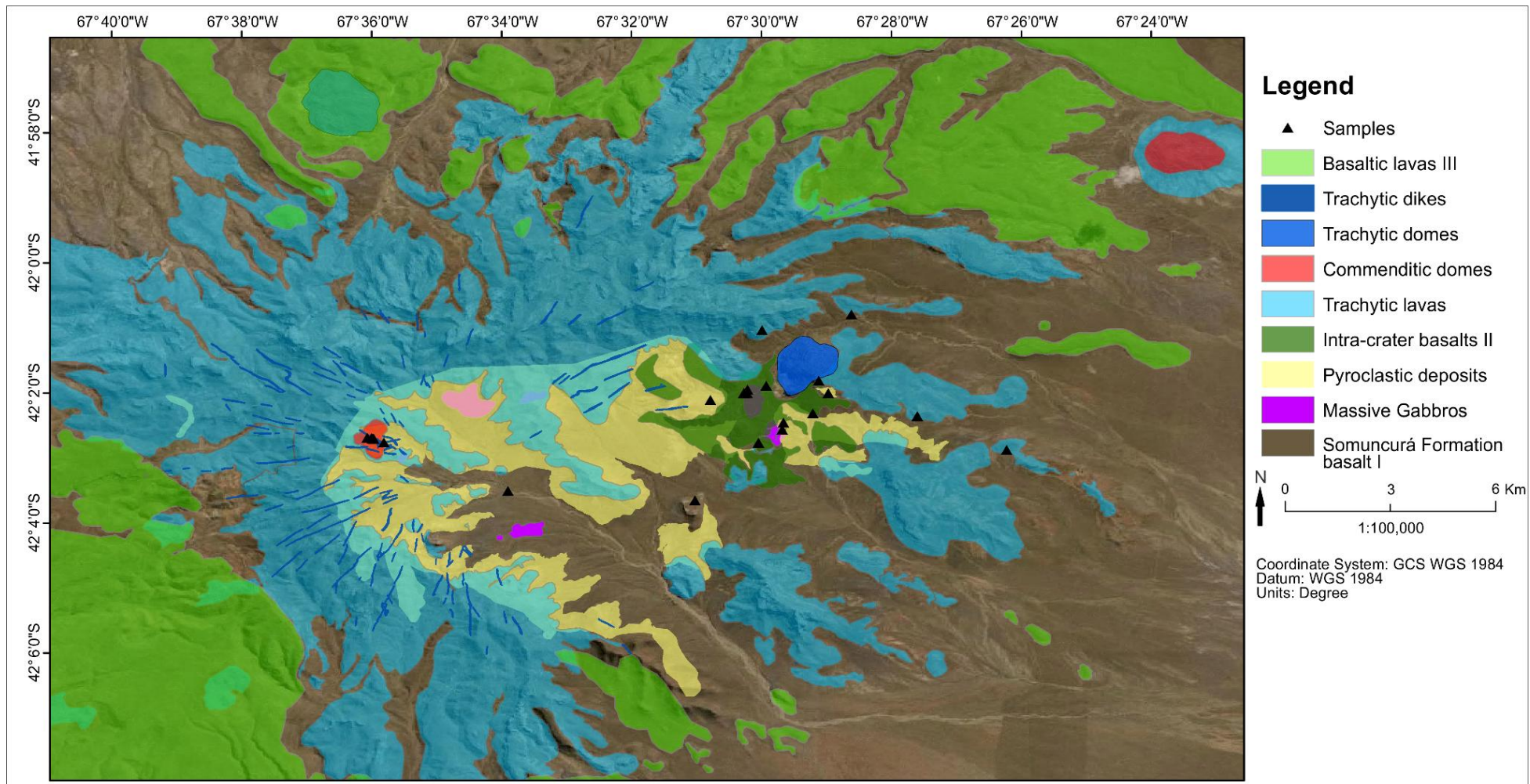


Figure 3 - Map showing the lithofacies distribution at the *Sierra de Apas* volcanic body.

## 4.2 Petrography

The microscopic petrographic analyses were carried out on 24 samples to interpret their lithofacies within the volcanic stratigraphy of the *Sierra de Apas*.

The lithotypes studied are basic rocks, such as basalt and gabbro; felsic rocks, such as trachyte and rhyolite; and pyroclastic rocks, such as tuffs.

Some macroscopic characteristics are shown, such as basaltic rocks with vesicles and reddish-brown color characterized by altering mafic minerals. The trachytes and commendites samples have similar macroscopic characteristics, such as color, aphanitic matrix, and presence of phenocrysts, but there is a notable difference in the ratio of phenocrysts to the matrix, ranging from 30/70 to 40/60 in the porphyritic samples of trachytes and 10/90 in the commendites.

Pyroclastic rocks, on the other hand, have a good selection of grains, with very fine to fine grain sizes and a yellowish-white color. The gabbroic rocks are aphanitic, with only a few olivine crystals visible and a grayish color.

As previously stated, the samples can be divided into 5 main groups, which will be described below.

### 4.2.1 Basaltic flow

The basalts studied are gray rocks porphyritic to glomeroporphyritic with oriented pilotaxitic matrix, inequegranular, and hypocrystalline, with varying degrees of oxidation and fine-grained, as shown in Figure 4. The oxidation mineral is iddingsite (5-15%), derived from the alteration of olivine (4A and 4D). The samples also contain olivine (5%), clinopyroxene – augite (15-30%), (4C) and plagioclase (50-55%) (4B) phenocrysts with *CarlsBad* twinning, the presence of opaque minerals (10%) as phenocrysts and dispersed in the matrix is also notorious. The phenocrysts sometimes form glomeruli and show corrosion features.

The samples have a very fine grain size (0.3 mm) and greater signs of oxidation, with matrix orientation indicated by tabular plagioclase. Sample CAP 58 has a fine grain size and lower oxidation and matrix orientation.

The augites and olivines are phenocrysts, with alteration, giving a relationship of formation before forming the matrix, which is mostly fine-grained and oriented.

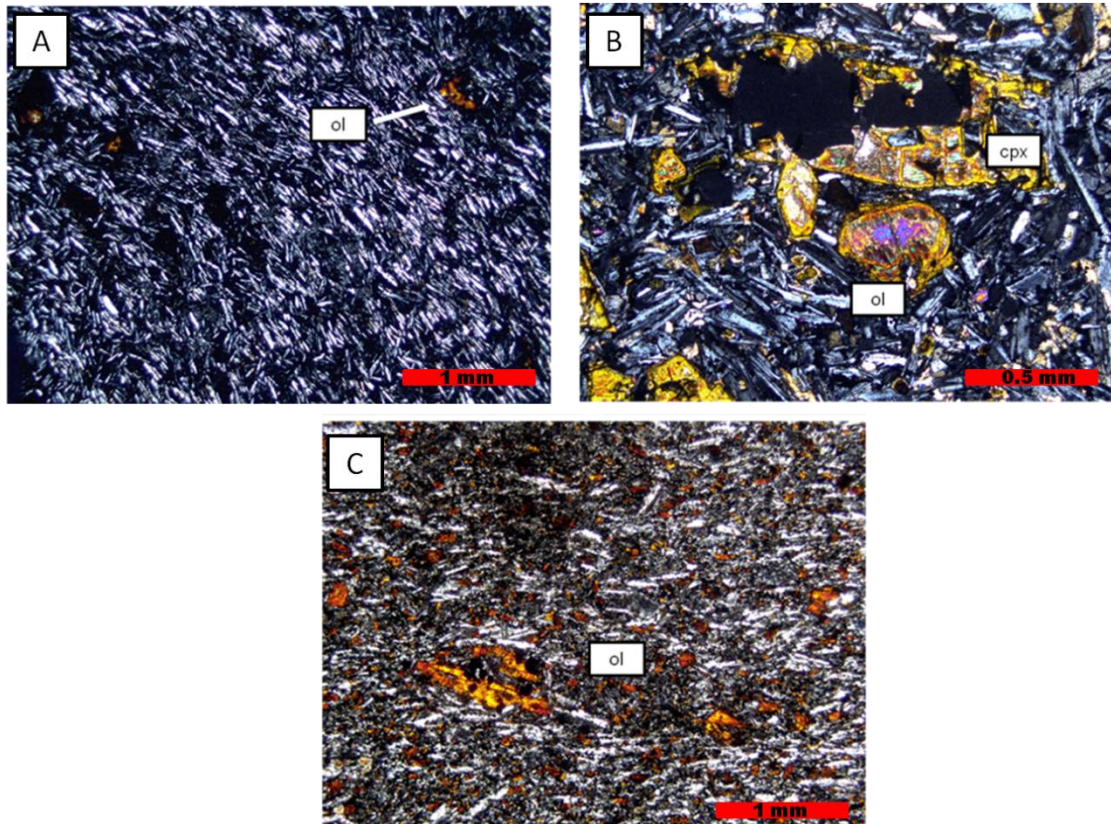


Figure 4 - Photomicrograph of samples A - CAP 06, B - CAP 58, and C - CAP 59, crossed polarizers, emphasizing the mineralogy, texture, and granulometry of the samples, with pyroxene (px), olivine (ol), and plagioclase (pl).

#### 4.2.2 Gabbro

The gabbros studied are coarse-grained rocks (0.8 mm) of gray color and ophitic texture, equigranular, hypocrystalline, as shown in Figure 5. They are composed of olivine (15-30%), clinopyroxene (15-30%; 5B), and plagioclase (40-45%) with CarlsBad twinning (5A). The presence of opaque minerals (7-10%) is also notable, as is quartz (3-5%), which also formed fibrous aggregates with K-feldspars.

The gabbroic samples exhibit an intergranular texture characterized by the arrangement of plagioclase, with pyroxene and olivine filling the spaces between the tabular plagioclase crystals.

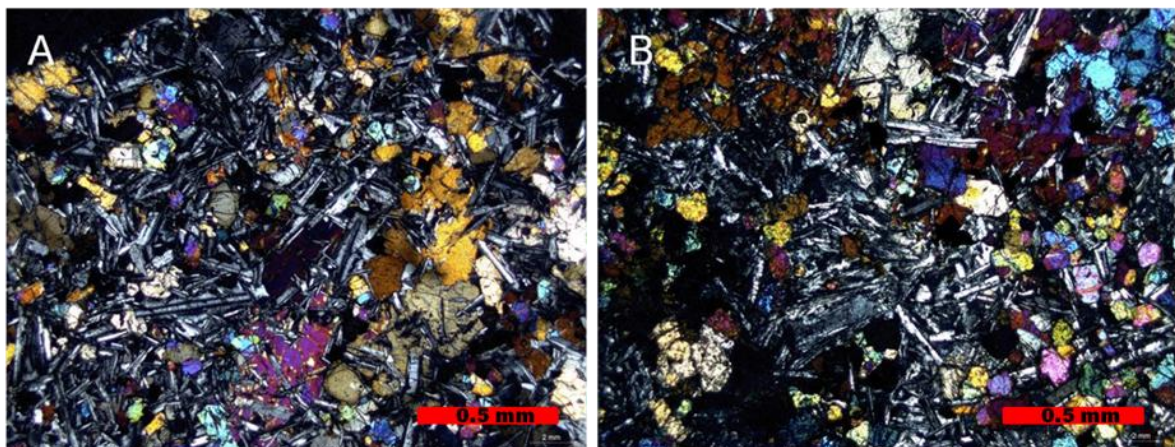


Figure 5 - CAP 14 and B - CAP 42 emphasize the mineralogy, texture, and granulometry of the two samples and the spherulites in image B.

#### 4.2.3 Domes and trachytic lavas

The trachytic samples, on the other hand, have a porphyritic texture, with feldspar phenocrysts, holocrystalline, aphanitic matrix fine-grained (less than 0.1 mm), and equigranular. Some samples have phenocrysts between 1.0 and 1.5 cm as seen in Figure 5.

Under the microscope, the trachytic rocks have a characteristic trachytic texture matrix, with a fine matrix of ripiform feldspar crystals (65-90%), quartz (5-10%), clinopyroxene (5-25%), opaque minerals (3-5%), and apatite (<1%). The matrix shows an orientation of the minerals that contours the phenocrysts (Figure 6). In this way, the feldspar glomerulus formed before the matrix, while no other minerals are found grouped with them (6B).

A petrographic feature found in trachytic and comenditic rocks are pyroxene, augite, and aegirine crystals, with dissolution features forming a texture known as a sieve (Fig 6C and 6D).

Some varieties are dominantly glomeroporphyritic (CAP 54, Figure 5B). The matrix, characterized by a pearlitic texture characterized by concentric spheres and cracks, is also important to mention.

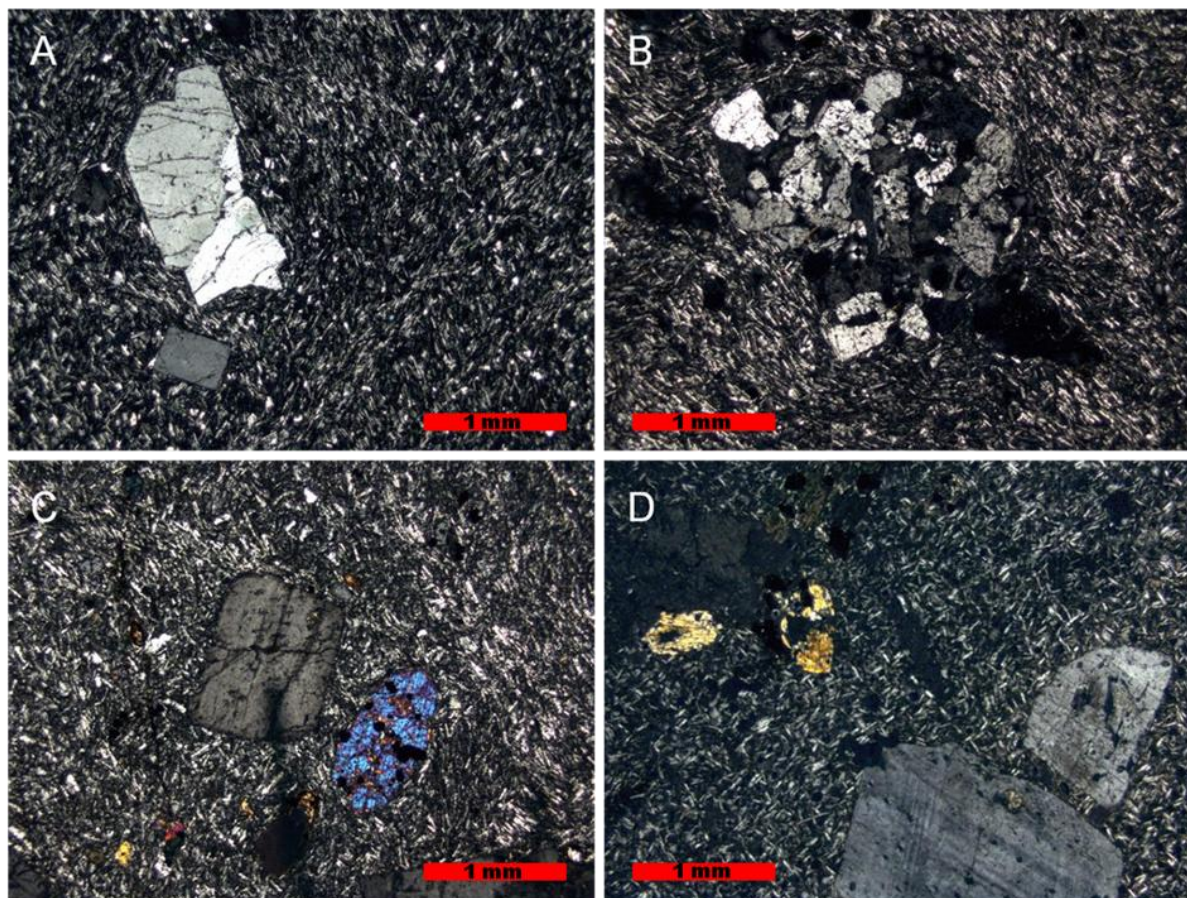


Figure 6 - Photomicrographs of samples A - CAP 13 A, B - CAP 15, C - CAP 31, and D - CAP 40, crossed polarizers, showing the mineralogy, texture, and granulometry of the samples, as well as the features of imbalance in images C and D.

#### 4.2.4 Domes and comenditic lavas

The commendite samples have a porphyritic texture, holocrystalline, aphanitic matrix fine-grained matrix (less than 0.1 mm) that makes it difficult to identify the minerals even under petrographic microscopes, with feldspar phenocrysts, some samples between 1.0 cm and 1.5 cm, Figure 7A, forming agglomerates.

The commendites have a characteristic trachytic texture, with a preferential orientation of the matrix, but are weaker than the trachytes. The minerals that make up this rock are alkali feldspar (55-75%), quartz (10-20%), aegirine (10-15%) and opaque minerals (5%). in addition, the presence of glass is observed in some samples

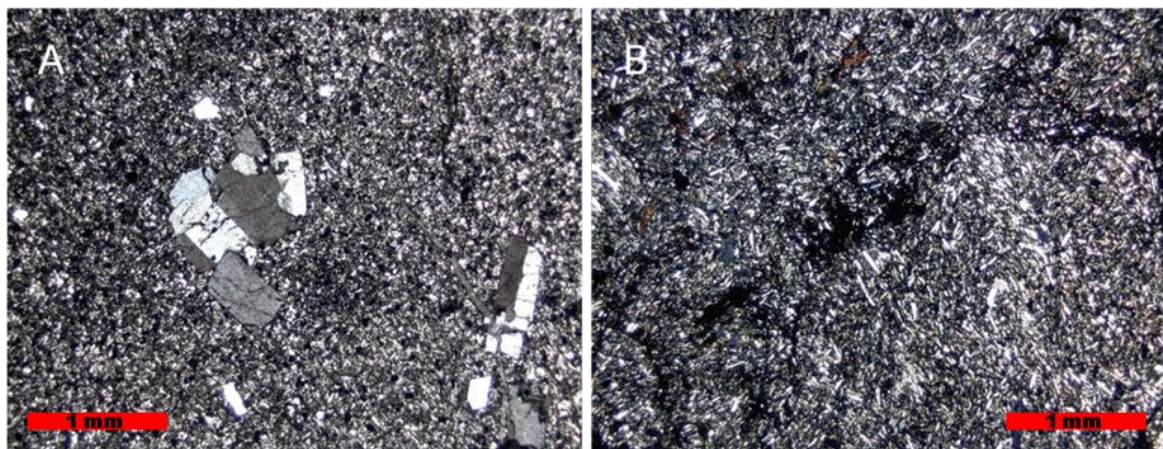


Figure 7 - Photomicrographs of samples A - CAP 53 and B - CAP 55 A crossed polarizers, emphasizing the two sample's mineralogy, texture, and granulometry.

#### 4.2.5 Pyroclastic rocks

The pyroclastic samples present different textures. Figure 8A, is made up of lithic fragments (10%) of trachyte, feldspar, and pyroxene, varying in size from less than 0.1 to 0.5 mm, mostly anhedral, and in specific portions of the matrix is notable the presence of carbonate (5%).

Sample CAP 11 has two portions, light and dark CAP 11 C (Figure 8B) and CAP 11 E (Figure 8C), respectively. The light portion comprises a very fine grayish aphanitic matrix; anhedral quartz (20%) and feldspar (30%) comprise the clasts and grayish lithic fragments. On the other hand, the dark portion is made up of a dark gray to black matrix, with elongated and subhedral feldspar microcrystals, as well as feldspar and pyroxene phenocrysts (5-10%), the latter fragmented and with inclusions of opaque minerals (5%).

The relationship between these two portions is characterized by a linear division, like two depositional cycles. Unfortunately, the sample wasn't collected oriented.

Figure 8D shows a photomicrograph of an ignimbrite with subhedral and equigranular feldspar (65%) and quartz crystals (25%). The matrix comprises a greenish aphanitic material, which includes pyroxene, rare opaque minerals (5%), and lithic fragments (2%), with a high percentage of felsic minerals.

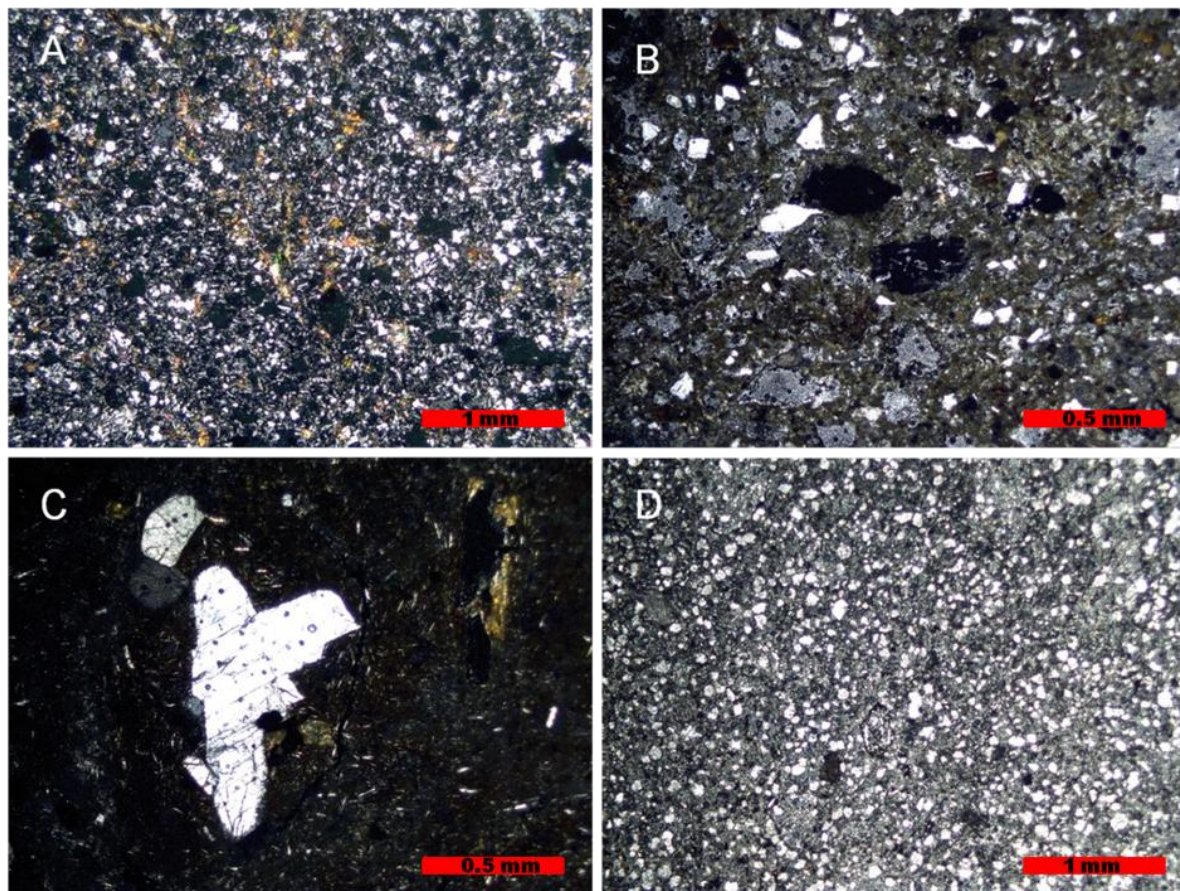


Figure 8 - Photomicrographs of samples A- CAP 08 A, B- CAP 11C, C- CAP 11E, and D- CAP 45 crossed polarizers, emphasizing the sample's mineralogy, texture, and granulometry.

### 4.3 Lithogeochemistry

#### 4.3.1 Analytical Classification

Table 3 shows the chemical analysis of total rock for major elements in percentage by weight, and Table 4 shows the results for trace elements in ppm.

The  $\text{SiO}_2$  content (Table 4), it is possible to separate the samples into two groups, acid rocks with  $\geq 77.4$  wt.% by weight of silica and basic rocks with  $\leq 43.1$  wt.%, as well as a third group with the results of 4 pyroclastic rock samples, that are also acid rocks.

The results obtained by lithogeochemical analysis allow the construction of graphs and diagrams that help us identify and interpret the studied samples, mainly the trachyte and commendite samples.

Table 4 - Total rock analysis of major elements in wt.%.

SAMPLES/ OXIDES	Basic rocks							Felsic rocks					
	CAP 6	CAP 38	CAP 58	CAP 59	CAP 14	CAP 39 A	CAP 41	CAP 54	CAP 5	CAP 13	CAP 15	CAP 19	CAP 31
SiO <sub>2</sub>	48.2	48.7	49.2	46.1	45.4	44.6	43.1	66.6	65	68.9	65.8	69	62.5
Al <sub>2</sub> O <sub>3</sub>	16.55	16.65	15.9	14.65	13.7	13.6	12.7	14.1	15.6	13.85	14.45	13.35	16.1
Fe <sub>2</sub> O <sub>3</sub>	11.55	11	11.1	14.75	13.2	13.35	13.85	2.95	5.52	4.42	4.31	5.41	5.58
CaO	5.05	5.83	8.67	8.54	9.05	9.03	8.08	0.6	1.55	0.26	0.82	0.56	1.58
MgO	1.7	2.23	5.49	3.73	9.9	8.53	14.25	0.02	0.4	0.07	0.04	0.01	0.42
Na <sub>2</sub> O	3.82	4.08	3.41	3.58	2.99	3.53	2.67	4.34	5.3	5.95	5.34	6.15	5.94
K <sub>2</sub> O	2.79	2.81	1.83	1.92	0.87	1.12	0.76	6.7	1.55	4.88	5.18	4.68	5.26
Cr <sub>2</sub> O <sub>3</sub>	0.004	0.004	0.03	0.004	0.041	0.025	0.056	<0.002	5.04	<0.002	<0.002	<0.002	<0.002
TiO <sub>2</sub>	2.71	2.73	2	4.21	1.73	1.91	1.32	0.29	0.62	0.28	0.37	0.35	0.6
MnO	0.12	0.16	0.15	0.19	0.17	0.18	0.17	0.1	0.11	0.08	0.07	0.14	0.08
P <sub>2</sub> O <sub>5</sub>	0.95	1.08	0.52	1.5	0.35	0.43	0.26	0.02	0.16	0.02	0.09	0.03	0.18
SrO	0.09	0.09	0.11	0.08	0.06	0.04	0.05	<0.01	0.02	<0.01	<0.01	<0.01	0.01
BaO	0.1	0.09	0.4	0.09	0.03	0.03	0.02	0.01	0.15	<0.01	0.02	<0.01	0.14
LOI	4.42	4.61	1.47	2.42	1.18	2.16	1.08	4.74	1.86	1.18	1.82	1.03	1.77
Total	98.05	100.06	100.58	101.76	98.67	98.54	98.37	100.47	101.33	99.89	98.31	100.71	100.16

Felsic rocks							Pyroclastic rocks - Felsic Rocks			
SAMPLES/ OXIDES	CAP 40	CAP 18	CAP 53	CAP 55 A1	CAP 55 A2	CAP 57 A	CAP 08A	CAP 11C	CAP 11E	CAP 45
SiO <sub>2</sub>	63.9	70.6	73.3	71.3	69.5	73.3	74.9	65	63.4	77.4
Al <sub>2</sub> O <sub>3</sub>	16.95	13.4	12.6	13.1	13.2	9.77	10.7	14.1	15.55	8.88
Fe <sub>2</sub> O <sub>3</sub>	2.68	4.46	4.06	4.49	5.55	4.93	5	5.29	5.95	3.9
CaO	1.61	0.21	0.14	0.46	0.45	0.14	0.23	0.91	0.96	0.25
MgO	0.32	0.02	0.01	0.02	0.03	0.01	<0.01	0.43	0.26	0.03
Na <sub>2</sub> O	5.24	5.9	5.46	4.52	4.48	4.59	5.25	4.15	5.92	4.24
K <sub>2</sub> O	1.61	5.03	4.9	4.6	4.71	4.03	4.21	5.84	5.48	3.65
Cr <sub>2</sub> O <sub>3</sub>	5.42	<0.002	<0.002	<0.002	<0.002	<0.002	<0.002	<0.002	<0.002	<0.002
TiO <sub>2</sub>	0.6	0.27	0.25	0.47	0.47	0.2	0.22	0.57	0.64	0.18
MnO	0.1	0.11	0.09	0.04	0.05	0.08	0.11	0.13	0.09	0.08
P <sub>2</sub> O <sub>5</sub>	0.13	0.01	0.02	0.06	0.06	0.02	0.04	0.03	0.06	0.03
SrO	0.01	<0.01	<0.01	<0.01	<0.01	<0.01	<0.01	0.01	<0.01	<0.01
BaO	0.13	<0.01	<0.01	<0.01	<0.01	<0.01	<0.01	0.13	0.21	<0.01
LOI	2.02	0.75	0.62	2.38	2.41	0.71	0.6	4.38	2.54	2.04
Total	99.11	100.76	101.45	101.44	100.91	97.78	101.26	100.97	101.06	100.68

The TAS diagram (total alkalis vs. silica) by Le Maitre et al. (1989) classifies the studied rocks according to their scientific nomenclature (Fig. 9A). In the diagram, the absence of intermediate samples is evident, the predominance of two groups of samples are notable, basic rocks (basalt, trachybasalt and basaltic trachyandesite), between 43.1 wt.% to 48.7 wt.% of silica, and acidic rocks (trachyte and rhyolite), between 62.5 wt.% to 77.4 wt.%. A sequence with an alkaline tendency is also observed. The dashed line separates the fields of alkaline (upper) from subalkaline (lower) rocks, according to Irvine & Baragar (1971).

Since the studied samples show an alkaline tendency, when using the Winchester & Floyd (1977) diagram (Fig. 9B), the Nb/Y ratio is greater than 1 in all samples, obtaining values near to 7 for samples with higher silica content, corroborating the alkaline tendency of the samples, which are classified as alkaline basalt, trachyte, and phonolite.

The CAP 08A, CAP 13, CAP 18, CAP 19, and CAP 53 samples plotted in the phonolite field have high ppm of Zr (Table 5). In addition, the percentage of TiO<sub>2</sub> is the lowest among the analyzed samples, 0.22, 0.28, 0.27, 0.35, and 0.25 wt.%, respectively, resulting in an elevated Zr/TiO<sub>2</sub> ratio.

According to Shand (1943), the alumina saturation index diagram (Fig. 9), A/NK = Al<sub>2</sub>O<sub>3</sub>/(Na<sub>2</sub>O + K<sub>2</sub>O) [molar ratio] and A/CNK = Al<sub>2</sub>O<sub>3</sub>/(CaO + Na<sub>2</sub>O + K<sub>2</sub>O) [molar ratio] is used to classify the samples in metaluminous, peraluminous and peralkaline compositions. Samples are classified as metaluminous and peralkaline, the basic rocks are metaluminous, while the trachyte, commendites, and pyroclastic rocks are classified as peralkaline, or very near to the transitional line, having a very low percentage of CaO, in addition, the high concentration of zirconium is indicative of peralkaline rock, which occurs with these samples.

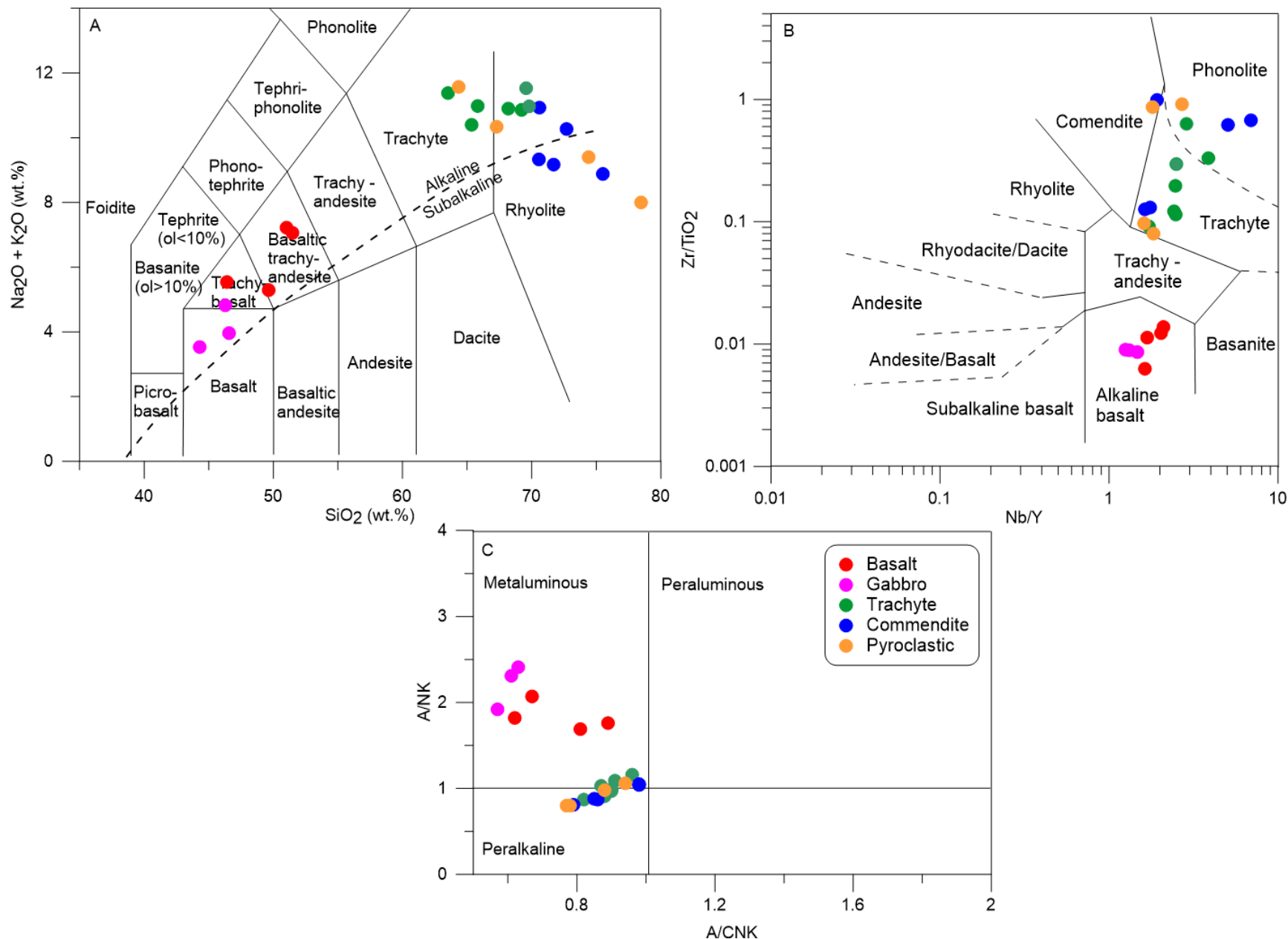


Figure 9 - A - Geochemical classification according to Le Maitre (1989) and Irvine & Baragar (1971). B - Diagram proposed by Winchester & Floyd (1977) corroborating the alkaline tendency of the samples studied. C - Alumina Saturation Index diagram proposed by Shand (1943) for the analyzed samples.

#### 4.3.2 Harker Diagrams

The Harker diagrams (Figs. 10 and 11) reveal a distinctly bimodal magmatism, characterized by two groups of samples: basic and felsic rocks. These diagrams, which plot major element oxides against silica ( $\text{SiO}_2$  wt.%) content, help define relationships between the geochemistry and mineralogy of the samples (Fig. 10). Specifically, the oxides  $\text{Na}_2\text{O}$ ,  $\text{K}_2\text{O}$ , and  $\text{CaO}$  clearly reflect the composition of feldspars. In the basic samples (depicted in red and pink),  $\text{Na}_2\text{O}$  and  $\text{K}_2\text{O}$  levels are lower, while  $\text{CaO}$ , indicative of plagioclase chemistry, is significantly higher, ranging from 5.05 to 9.05 wt.%. In contrast, the trachytes (green), comendites (blue), and pyroclastic rocks (orange) show low  $\text{CaO}$  content ranging from 0.26 to 1.61 wt.% in trachytes, 0.14 to 0.46 wt.% in comendites, and 0.23 to 0.96 wt.% in pyroclastic samples, while  $\text{Na}_2\text{O}$  and  $\text{K}_2\text{O}$  concentrations are elevated, reflecting the dominance of alkali feldspars.

Higher  $\text{MgO}$  and  $\text{FeOT}$  contents in the basic samples are attributed to the greater abundance of olivine and pyroxene compared to the acidic rocks.  $\text{TiO}_2$  is predominantly present in the basic rocks, derived from titanium-rich augites, while  $\text{P}_2\text{O}_5$  is also more concentrated in the basic samples.

$\text{Al}_2\text{O}_3$  exhibits a clear bimodal pattern, with an increasing trend in the basic samples and a decreasing trend in the acidic samples, closely mirroring the behavior observed in the Alumina Saturation Index diagram.

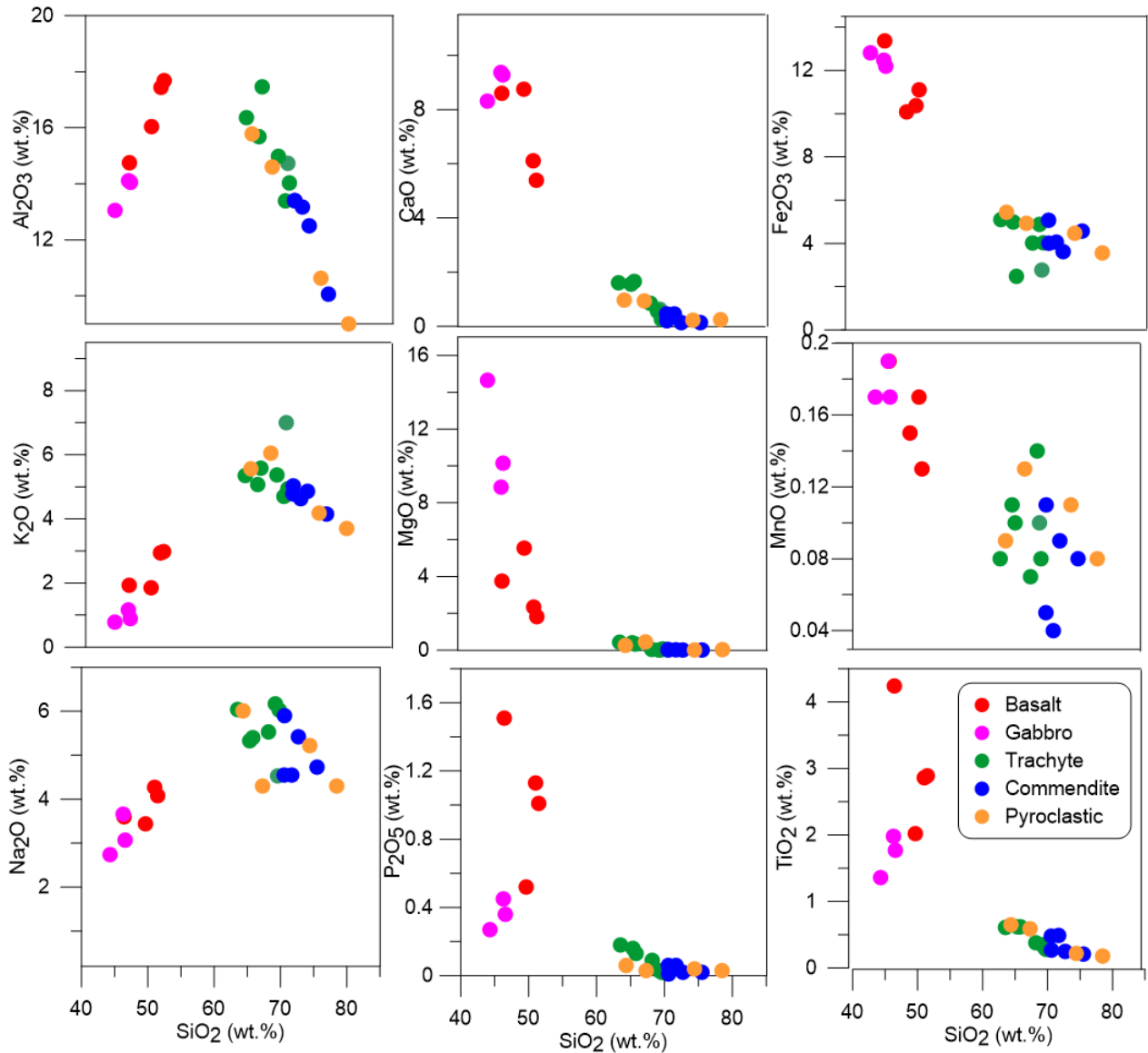


Figure 10: Variation diagram representing the most abundant major elements in the lithogeochemical analysis as a function of  $\text{SiO}_2$  (wt.%).

Table 5 presents the concentrations of trace elements in parts per million (ppm). While some values and elements have been discussed previously, this section focuses on diagrams specifically related to trace element analysis. Notable positive anomalies are observed, particularly for Ba in sample CAP 58, Zr in samples CAP 08A, CAP 13, CAP 18, CAP 19, and CAP 53, as well as V and U in sample CAP 40.

Figure 11, which displays trace element variation as a function of  $\text{SiO}_2$ , reveals a pronounced linear relationship for nearly all elements, with the exception of Ba, Y, and Cs, where a noticeable dispersion of data points is observed.

Furthermore, incompatible lithophile elements such as Rb, U, Hf, Zr, Nb, and Th exhibit a positive correlation with increasing  $\text{SiO}_2$  concentrations, indicating enrichment with increasing silica content.

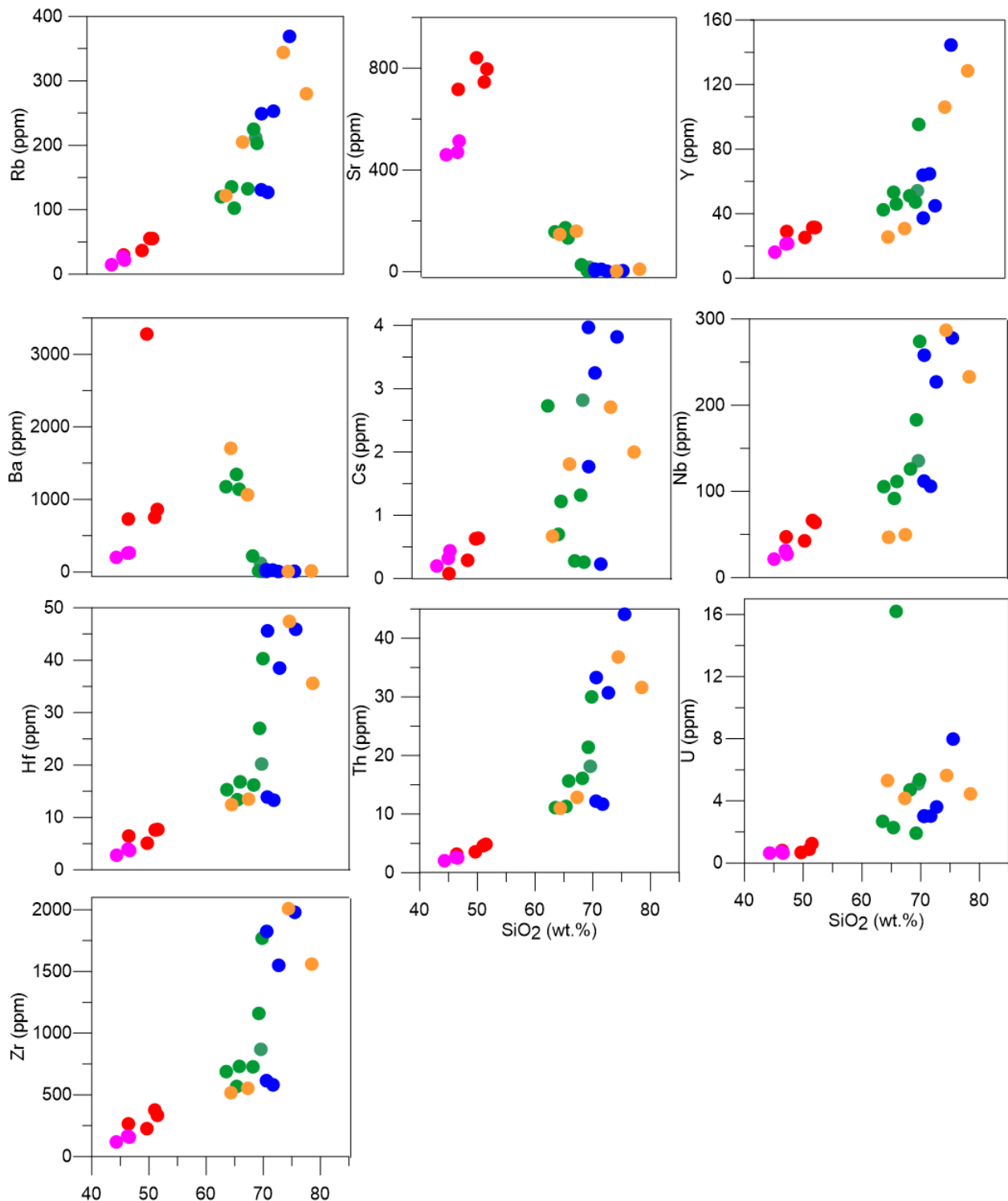


Figure 11: Trace element variation diagram as a function of  $\text{SiO}_2$  (wt.%).

Table 5 - Total rock analysis of trace elements in ppm (ICP-MS by lithium borate fusion).

SAMPLES/ ELEMENTS	Basic rocks							Felsic rocks					
	CAP 6	CAP 38	CAP 58	CAP 59	CAP 14	CAP 39 A	CAP 41	CAP 54	CAP 5	CAP 13	CAP 15	CAP 19	CAP 31
V	127	156	240	348	234	222	177	<5	5	5	<5	<5	23
Cr	29	33	250	29	340	178	470	5	20	<5	9	6	8
Ga	25.9	24.7	20.8	23.9	20.4	20.6	17.8	31.8	30.9	50.6	35.1	45.7	30.1
Rb	55.3	55.5	36.7	29.9	21.9	27.1	14.7	212	135.5	203	132.5	225	120
Sr	797	746	841	717	514	470	460	17.8	173	5.6	27.6	3.8	157
Y	31.4	31.5	25.3	29	21.5	21.3	16.2	54.2	53.3	95.3	51.1	47.2	42.4
Zr	334	377	226	265	157	165	118	869	568	1770	727	1160	688
Nb	63.9	66.3	42.7	47.3	27	31.4	21.5	135.5	91.8	274	126	183	105.5
Ba	862	753	3280	730	265	260	201	120.5	1345	8.8	220	13.8	1175
Cs	0.64	0.63	0.29	0.08	0.44	0.32	0.2	2.82	0.7	0.26	0.28	1.32	2.73
La	48.3	47.3	31.6	41.7	20.4	22.4	16	98.9	84	197	92.4	108	74.4
Ce	94.8	97.1	61.6	89.7	40.3	46.7	32.1	190	150	346	169.5	242	140
Pr	12.05	11.7	7.66	10.5	5.19	5.33	3.99	19.55	17.4	41.9	19.75	23.6	14.65
Nd	51.8	51.7	30.6	47.9	21.3	25.4	16.4	71.9	64.7	142	69.5	95.8	58.3
Sn	2.9	3.7	2	2.2	2	1.7	2	6	4	12	5.8	7.9	5.1
Sm	11.2	11.5	6.23	9.52	4.81	5.36	3.5	14.55	11.95	26.6	13.2	16.5	10.35

Eu	3.39	3.59	1.86	3.11	1.58	1.7	1.27	1	2.73	0.99	1.21	0.77	2.65
Gd	9.68	8.96	5.64	8.8	4.63	5.24	3.65	11.65	9.9	20.6	9.41	12.25	8.92
Tb	1.3	1.28	0.81	1.2	0.7	0.82	0.58	1.76	1.6	3.31	1.67	1.86	1.46
Dy	6.53	6.93	4.48	6.44	3.83	4.42	3.07	10.7	8.91	19.15	9.1	10.8	8.49
Ho	1.3	1.27	0.88	1.16	0.78	0.83	0.61	2.14	1.77	3.95	2.03	2.13	1.68
Er	2.94	2.72	2.25	2.85	1.89	2.08	1.54	5.9	5.03	10.95	5.15	5.49	4.27
Tm	0.39	0.4	0.34	0.39	0.3	0.33	0.24	0.91	0.71	1.58	0.82	0.94	0.64
Yb	2.34	2.14	1.83	2	1.6	1.7	1.16	5.49	4.02	10.8	5.51	6.88	3.78
Lu	0.36	0.33	0.26	0.3	0.23	0.22	0.16	0.79	0.61	1.53	0.87	1	0.62
Hf	7.71	7.62	5.1	6.47	3.7	3.98	2.8	20.2	13.4	40.3	16.2	27	15.3
Ta	3.7	3.7	2.7	2.7	3.7	2	1.4	8	6.3	16	7	10.6	5.7
W	84.6	70.8	149	218	241	81.5	107	312	96	194	2.6	492	131.5
Th	4.85	4.6	3.56	3.16	2.53	2.62	2.04	18.15	11.3	30	16.1	21.4	11.1
U	1.25	0.88	0.68	0.81	0.64	0.73	0.64	5.1	2.28	5.37	4.71	1.92	2.68
La/Yb	20.64	22.10	17.27	20.85	12.75	13.18	13.79	18.01	20.90	18.24	16.77	15.70	19.68
La/Nb	0.76	0.71	0.74	0.88	0.76	0.71	0.74	0.73	0.92	0.72	0.73	0.59	0.71
La/Ta	13.05	12.78	11.70	15.44	5.51	11.20	11.43	12.36	13.33	12.31	13.20	10.19	13.05
Ti/Yb	11581.20	12757.01	10928.96	21050	10812.50	11235.29	11379.31	528.23	1542.29	259.26	671.51	508.72	1587.30
Zr/Nb	5.23	5.69	5.29	5.60	5.81	5.25	5.49	6.41	6.19	6.46	5.77	6.34	6.52
Zr/Y	10.64	11.97	8.93	9.14	7.30	7.75	7.28	16.03	10.66	18.57	14.23	24.58	16.23
Y/Nb	0.49	0.48	0.59	0.61	0.80	0.68	0.75	0.40	0.58	0.35	0.41	0.26	0.40
Ba/Rb	15.59	13.57	89.37	24.41	12.10	9.59	13.67	0.57	9.93	0.04	1.66	0.06	9.79
K/P	2.94	2.60	3.52	1.28	2.49	2.60	2.92	335	31.50	244	57.56	156	29.22

SAMPLES/ ELEMENTS	Felsic Rocks					Pyroclastic rocks - Felsic Rocks				
	CAP 40	CAP 18	CAP 53	CAP 55 A1	CAP 55 A2	CAP 57 A	CAP 08A	CAP 11 C	CAP 11 E	CAP 45
V	17	15	9	<5	<5	<5	<5	16	10	7
Cr	<10	<10	<10	<5	8	6	6	9	7	7
Ga	33.2	44.5	42	37.2	49.9	44.3	49	27.5	30.2	37.2
Rb	102.5	249	253	127	131	369	344	205	122	280
Sr	133	3.5	2.1	9.6	10.2	4.2	2.9	159.5	147	10
Y	46	37.3	44.9	64.7	63.9	144.5	106	30.8	25.5	128.5
Zr	731	1825	1550	581	615	1980	2010	553	517	1560
Nb	111.5	258	227	106	112	278	287	49.8	46.8	233
Ba	1140	7.9	6.4	26.7	31.6	9.5	8	1065	1705	14.5
Cs	1.22	1.77	0.23	3.25	3.97	3.82	2.71	1.81	0.67	2
La	82.5	104	89.9	87.2	84.4	195	202	63.3	59.7	169.5
Ce	173.5	184.5	161.5	170	169.5	337	374	107	98.7	324
Pr	17.8	18.15	18.1	21.3	20.6	42.3	45.2	12.4	11.85	36.3
Nd	62.9	57.3	57.2	82.2	77.2	168.5	166.5	91	80.8	143.5
Sn	5	14	12	3.5	4.8	15.5	16.1	5.9	4.2	11.7
Sm	12.1	9.36	9.51	17.25	15.8	34.3	33.2	10.1	8.07	28.3

Eu	2.47	0.31	0.32	1.02	0.94	0.92	0.88	2.09	2.99	0.81
Gd	9.04	7.07	6.96	13.15	12.95	28.7	25.1	8.24	7.02	24.4
Tb	1.45	1.25	1.22	2.13	2.06	4.75	3.79	1.18	1.06	4.11
Dy	8.4	7.57	7.11	12.85	11.5	27.2	21.7	7.58	6.1	24.3
Ho	1.69	1.46	1.6	2.66	2.39	5.75	4.27	1.37	1.15	4.9
Er	4.41	4.33	4.91	7.15	7.03	15.6	11.3	3.79	3.08	13.7
Tm	0.68	0.7	0.82	1.03	0.92	2.29	1.67	0.55	0.51	2.03
Yb	3.91	4.88	5.97	7.6	6.58	14.35	10.85	3.41	2.89	12.2
Lu	0.59	0.77	0.9	1.11	1.04	1.98	1.75	0.52	0.49	1.71
Hf	16.8	45.6	38.5	13.3	13.9	45.9	47.4	13.5	12.45	35.6
Ta	8.4	17.7	15.9	5.2	5.7	15.4	16.5	5.1	4.6	12.8
W	295	372	253	166	3.4	3.8	118.5	119.5	144.5	498
Th	15.65	33.3	30.7	11.7	12.2	44.1	36.8	12.85	11	31.6
U	16.2	3.04	3.61	3.02	3	7.98	5.64	4.16	5.31	4.45
La/Yb	21.10	21.31	15.06	11.47	12.83	13.59	18.62	18.56	20.66	13.89
La/Nb	0.74	0.40	0.40	0.82	0.75	0.70	0.70	1.27	1.28	0.73
La/Ta	9.82	5.88	5.65	16.77	14.81	12.66	12.24	12.41	12.98	13.24
Ti/Yb	1534.53	553.28	418.76	618.42	714.29	139.37	202.76	1671.55	2214.53	147.54
Zr/Nb	6.56	7.07	6.83	5.48	5.49	7.12	7.00	11.10	11.05	6.70
Zr/Y	15.89	48.93	34.52	8.98	9.62	13.70	18.96	17.95	20.27	12.14
Y/Nb	0.41	0.14	0.20	0.61	0.57	0.52	0.37	0.62	0.54	0.55
Ba/Rb	11.12	0.03	0.03	0.21	0.24	0.03	0.02	5.20	13.98	0.05
K/P	41.69	503.00	245.00	76.67	78.50	201.50	105.25	194.67	91.33	121.67

#### 4.3.3 Trace Elements

The analyzed samples exhibit enrichment of incompatible elements when compared to the primitive mantle-normalized values of Sun and McDonough (1989) (Figure 17). In contrast, lithologies with lower SiO<sub>2</sub> concentrations display more typical geochemical behavior. The comendites (blue) show notable negative anomalies for Ba and Sr, alongside positive anomalies for Zr and Rb. Trachytes (green) exhibit a similar pattern, though with less pronounced anomalies, indicating plagioclase fractionation. Additionally, sample CAP 40 reveals a distinct positive U anomaly. Pyroclastic rocks (orange) generally follow the geochemical trends of acidic samples, showing Ba and Sr anomalies. In comparison, the basalt sample CAP 58 behaves similarly to other basic rocks but displays a positive Ba anomaly.

In the primitive mantle-normalized diagram (Figure 12), three reference compositions from Sun and McDonough (1989) were included: Lower Continental Crust (LCC), N-MORB, and Upper Continental Crust (UCC). While the overall geochemical behavior is similar, positive anomalies are observed in relation to N-MORB, with the exceptions of Sr and Nd. The basic samples align with this trend, while the acidic samples show negative Sr anomalies and positive Nd anomalies. The LCC and UCC data appear more linear, featuring positive anomalies for Ba, Ti, Sr, P, Zr, and Ti, and negative anomalies for Ba, Th, U, Sr, Eu, and Tb.

A chondrite-normalized diagram (Figure 12) further demonstrates that the lithologies exhibit largely consistent geochemical behavior. Eu anomalies in the comenditic samples are positive in CAP 53 and 55, but negative in CAP 18.

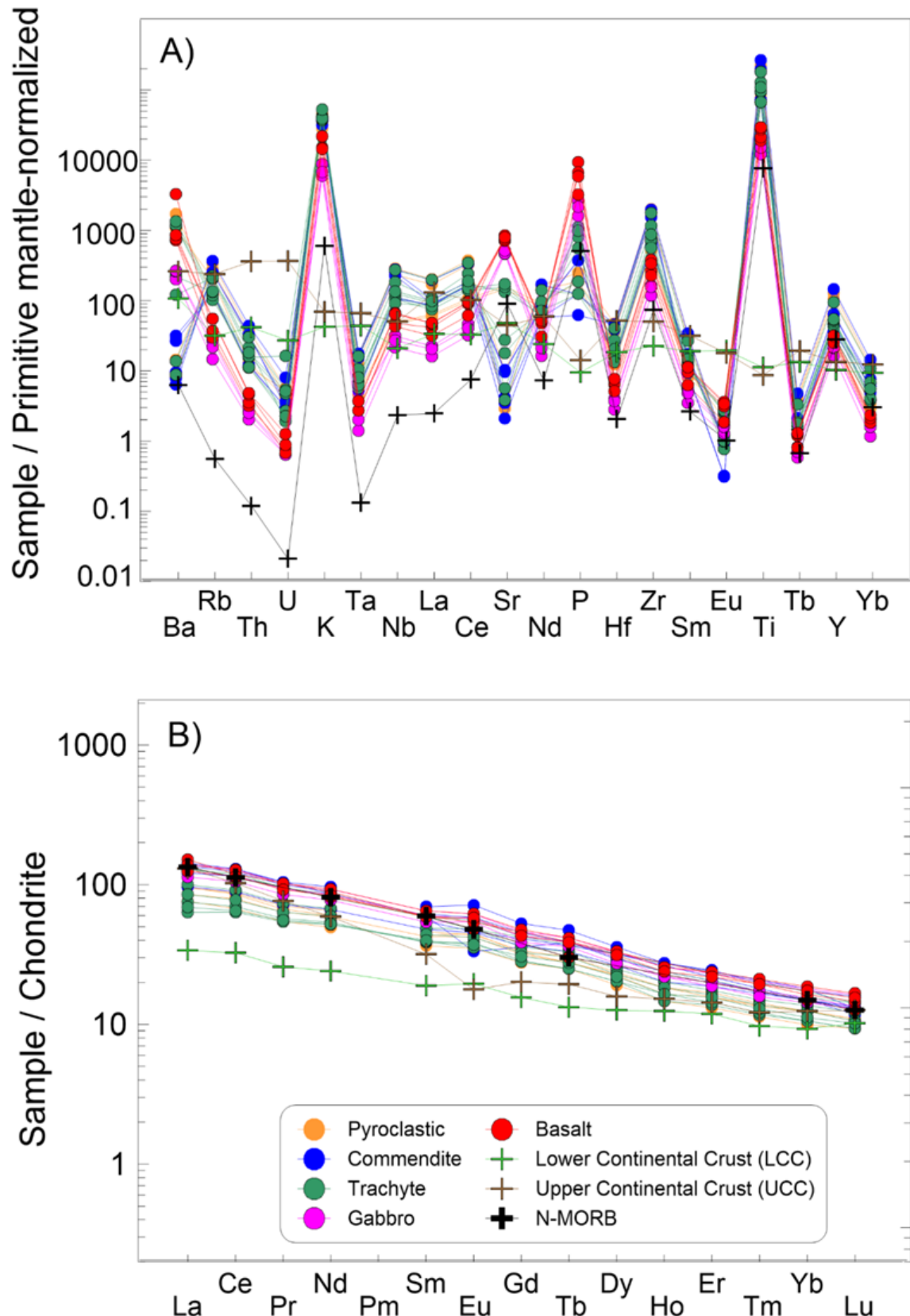


Figure 12 - Diagrams of normalized trace elements according to the values of Sun & McDonough (1989) for primitive mantle and chondrite.

Certain geochemical diagrams facilitate the interpretation of rock environments and provenance by analyzing the ratios of specific trace elements. Figure 13 illustrates the Nb/Yb versus Th/Yb diagram from Pearce (2008), which provides insight into these relationships. In this diagram, the basic rock samples are plotted near the Ocean Island Basalt (OIB) field, whereas the acidic samples deviate from the mantle's compositional variation trend, indicating significant crustal contamination. The dotted arrow highlights the enrichment of thorium and niobium, particularly pronounced in the comenditic samples.

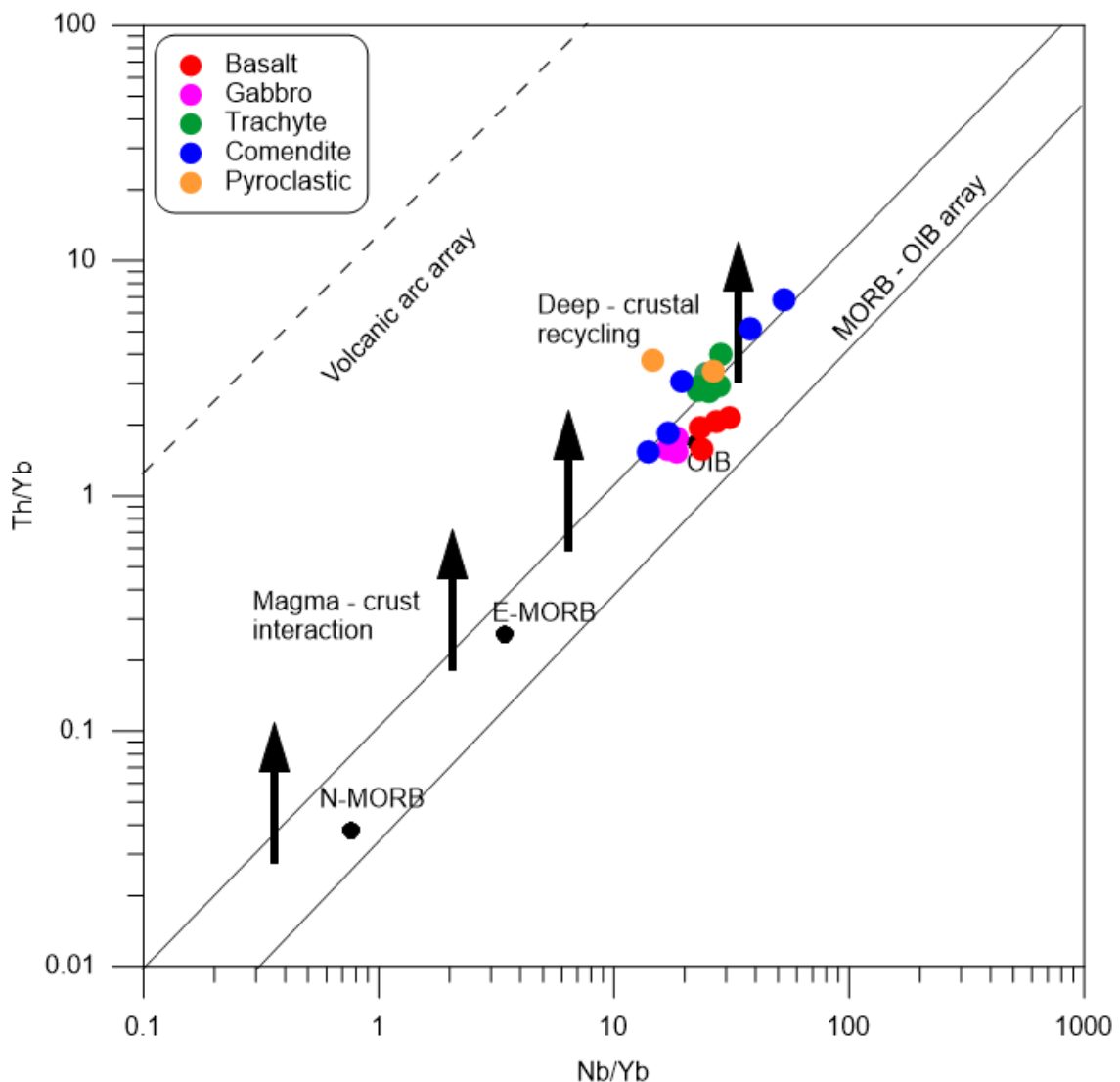


Figure 13: Nb/Yb vs. Th/Yb diagram from Pearce (2008), the dark arrows indicate crustal contamination, while the dotted arrow indicates the evolution path of the samples studied.

#### 4.4 Mineral chemistry

The alkali feldspar and plagioclase classification diagram (Figure 14A) illustrates four distinct lithologies. The analyzed trachytes and comendites predominantly contain alkali feldspars, with compositions ranging from 63% to 70% Ab (anorthoclase) in some samples, while others exhibit sanidine with Or content between 60% and 65%. The comendites, in particular, exhibit a strong correlation with Ab content between 63% and 67% and An < 0.4%.

In contrast, the basic samples primarily consist of plagioclase, with labradorite compositions characterized by An content ranging from 60% to 62% and Ab from 35% to 37%. Some samples, however, show more diverse results, with three points classified as sanidine and one as anorthoclase, indicating the presence of alkali feldspars. Gabbro samples contain both plagioclase and alkali feldspar, with An content ranging from 12% to 73% and Ab from 25% to 80%, classified as bytownite, labradorite, andesine, and anorthoclase. Notably, half of the analyzed points in the gabbro samples are classified as labradorite.

Pyroxene classification (Figure 14B) reveals that the basalt, gabbro, and trachytic sample CAP 40 contain pyroxenes predominantly classified as diopside, with compositions ranging from Wo<sub>39–59</sub>, En<sub>35–02</sub>, Fs<sub>11–4</sub> at a minimum, to Wo<sub>47–52</sub>, En<sub>41–87</sub>, Fs<sub>18–97</sub> at a maximum. However, two readings were classified as hypersthene, with Wo<sub>01</sub>, En<sub>67.5</sub>, and Fs<sub>31.5</sub>. The acidic sample was classified as containing augite.

Figure 14C presents the classification of olivines from three basic samples, indicating a high Mg content in forsterite ( $Mg_2SiO_6$ ), with Fo concentrations exceeding 50%. Notably, sample CAP 58 contains measurements of Fo > 80%, indicating a particularly high forsterite content.

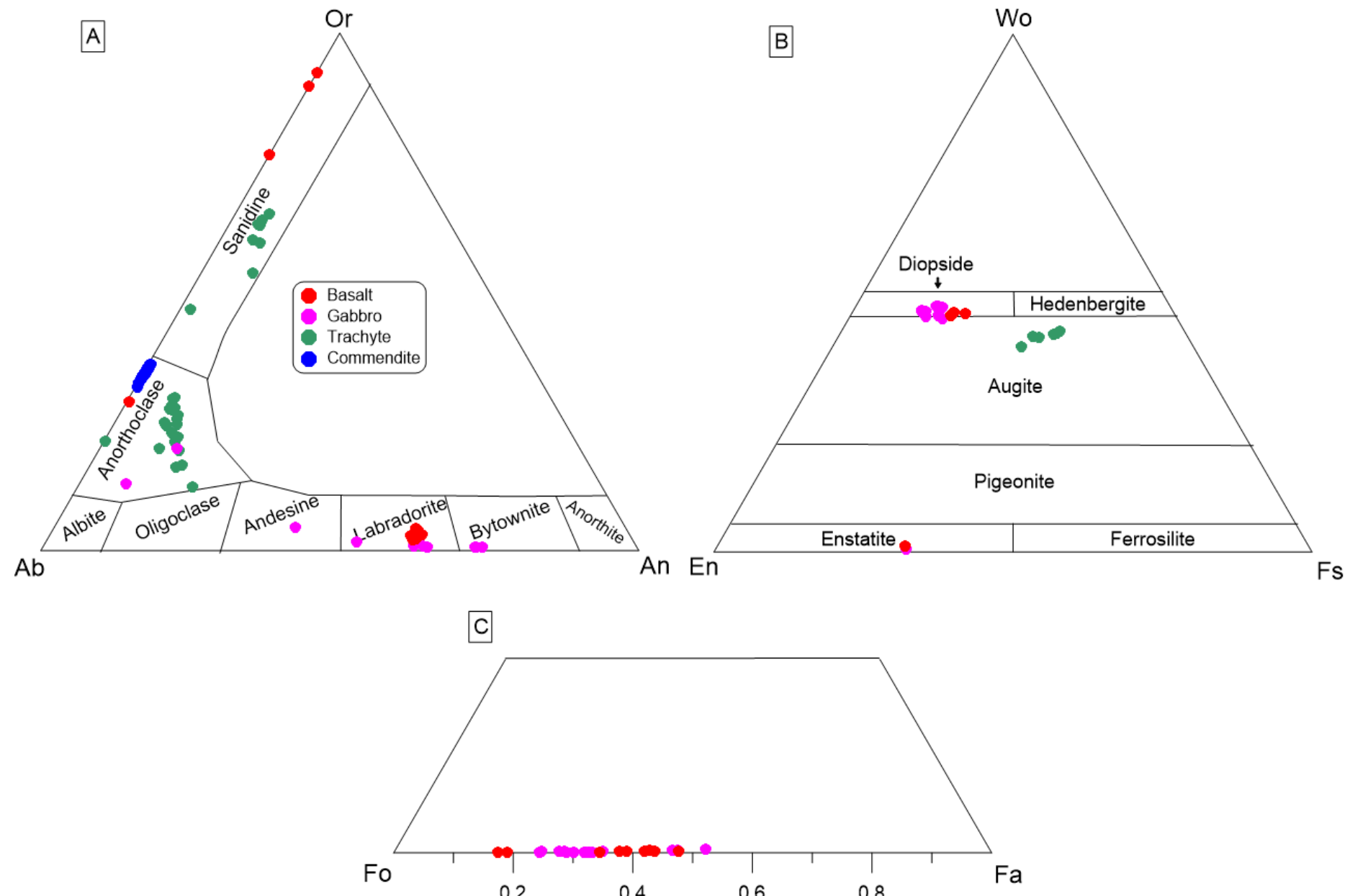


Figure 13 - Diagrams developed applying the microprobe analysis (A) Ab-An-Or diagram for feldspar classification proposed by Deer et al. (1963). (B) En-Fs-Wo pyroxene classification diagram by Morimoto (1988). (C) Fo-Fa-Tp olivine classification diagram.

#### 4.5 Geochronology

At the conclusion of the geochronological sample preparation process, apatite grains were retained following separation using dense liquids. Two trachyte samples, CAP 26 and CAP 40, were selected for U-Pb dating.

Secondary electron images were obtained via SEM imaging, providing detailed morphological descriptions of the mineral grains. Additionally, SEM-EDS analysis confirmed the identification of the grains as apatites, with only one zircon observed (highlighted by red circles in Figure 15).

The apatites fall into two groups, characterized by colorless, transparent grains with a glassy luster (Figure 14). The crystals range in size from 60 to 350 micrometers. The images also revealed multiple sets of rough fractures and irregular boundaries in the crystal structure.

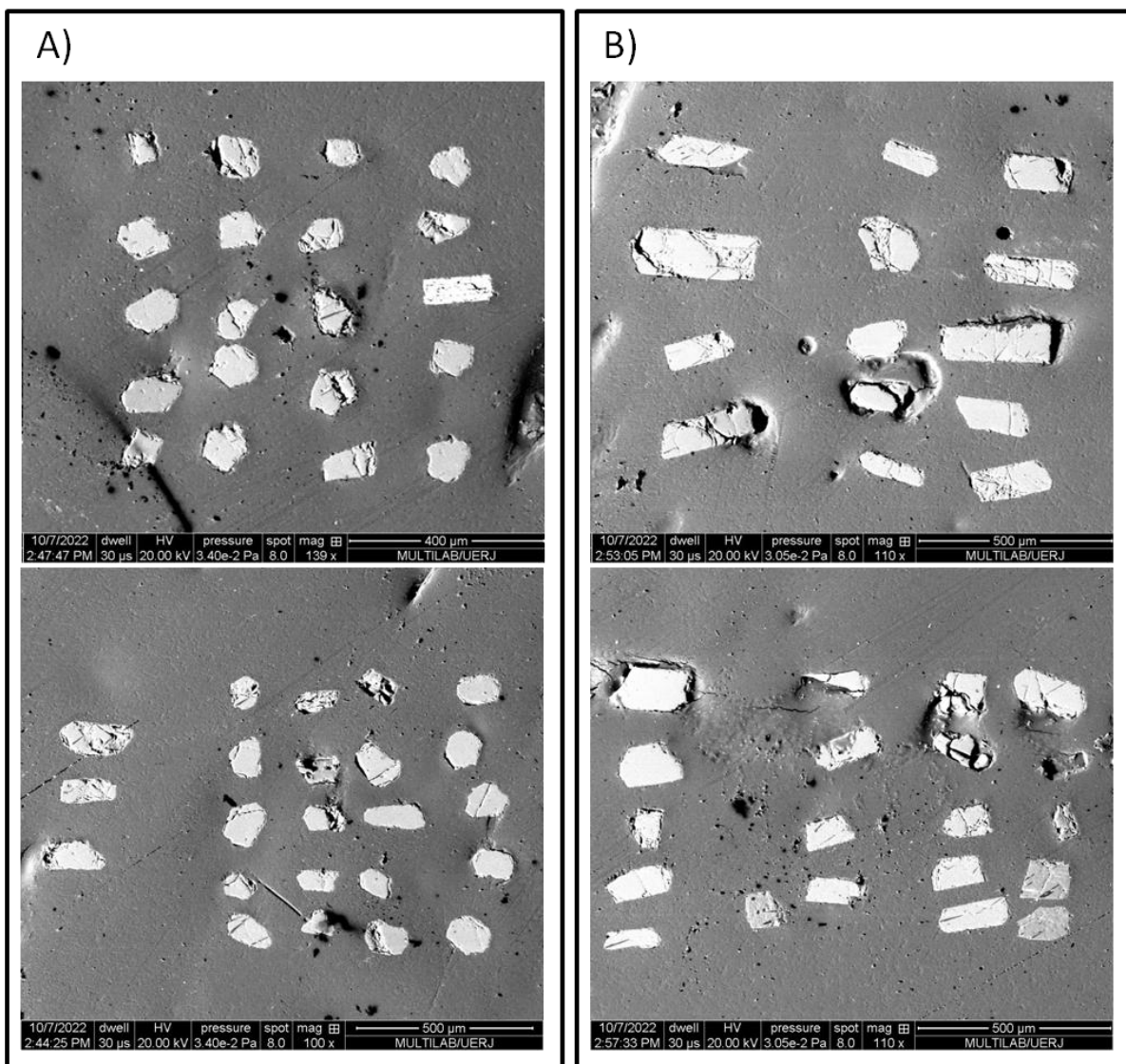


Figure 14 - Secondary electron images of the apatites, emphasizing the morphology of the grains for the three trachytic samples. A - CAP 26; and B - CAP 40.

The  $^{238}\text{U}/^{206}\text{Pb}$  versus. The  $^{207}\text{Pb}/^{206}\text{Pb}$  diagram facilitates the construction of concordia plots using Isoplot R (Figure 15), with cathodoluminescence images from SEM inserted into each graph for reference. No common lead correction was applied during the diagram's development; instead,  $^{207}\text{Pb}$  was used due to the minimal variation in uranium content within the grains. This limited variation increases the margin of error, as the concordia would be narrowly spaced based on the collected values.

When analytical errors are accounted for, the obtained ages for the studied samples are both close and comparable (Figure 15), with trachyte CAP 26 dated at

$27.09 \pm 1.37$  Ma and CAP 40 at  $25.29 \pm 1.70$  Ma. The mean squared weighted deviation (MSWD) values vary, both above and below 1. Sample CAP 26 has an MSWD < 1, indicating less observed dispersion than predicted by the analytical uncertainties, classifying the data as "underdispersed" and suggesting that the analytical uncertainties may have been overestimated. In contrast, sample CAP 40 shows MSWD values > 1, with the observed dispersion exceeding that predicted by the analytical uncertainties.

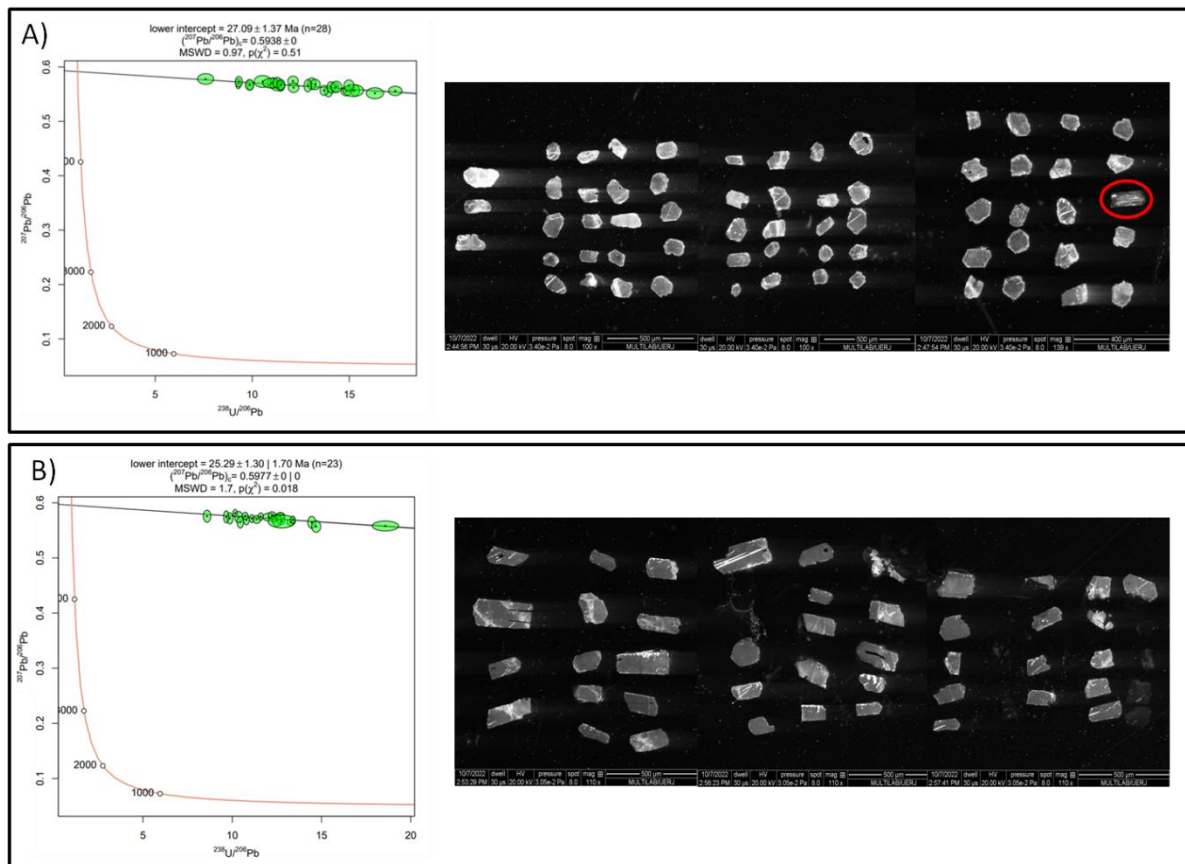


Figure 15 - The concordia diagrams,  $^{238}\text{U}/^{206}\text{Pb}$  versus.  $^{207}\text{Pb}/^{206}\text{Pb}$ , showing U-Pb geochronological analysis of the apatites for two trachytic samples from the Sierra de Apas region, and the cathode images . A - CAP 26; and B - CAP 40. Data are plotted uncorrected for common Pb. n - indicates the number of analyses used to calculate the age.

#### 4.6 Sr and Nd Isotopic ratios

Seven samples from *Sierra de Apas* were analyzed for Sr and Nd isotopes, two samples of commendites, trachytes, and gabbros, and also one basalt (Table 5).

Sm and Nd are light rare earth elements (ETR); most rock-forming minerals have difficulty admitting ETR into their crystal structures, although feldspars, biotite, and apatite tend to concentrate light elements (Lutetium to Neodymium), while pyroxenes, amphiboles and grandas concentrate heavy ETR (Gadolinium to Lutetium; Geraldes., 2010).

The  $^{143}\text{Nd}/^{144}\text{Nd}_{(\text{m})}$  isotopic ratios range from 0.512606 to 0.512894, with  $\epsilon\text{Nd}$  varying from - 0.62 to + 4.99. The  $^{87}\text{Sr}/^{86}\text{Sr}_{(\text{m})}$  ratios obtained from the *Apas* samples range between 0.703723 and 0.900385. After recalculating, the initial isotopic ratios yielded the following values:  $^{143}\text{Nd}/^{144}\text{Nd}_{(\text{i})}$  range from 0.512412 to 0.512874, with  $\epsilon\text{Nd}(\text{i})$  varying from - 0.3 to + 5.3, and  $^{87}\text{Sr}/^{86}\text{Sr}_{(\text{i})}$  range between 0.703690 and 0.767785.

Table 5 - Table showing the results of the Sr and Nd isotopic geochronology analyses for the seven selected samples, their respective identifications, and lithologies.

Samples	Lithology	$^{143}\text{Nd}/^{144}\text{Nd(m)}$	$^{143}\text{Nd}/^{144}\text{Nd(i)}$	$^{147}\text{Sm}/^{144}\text{Nd(m)}$	Rb/Sr	$^{87}\text{Sr}/^{86}\text{Sr(m)}$	$^{87}\text{Sr}/^{86}\text{Sr(i)}$	$\epsilon\text{Nd}$	$\epsilon\text{Nd(i)}$	TDM
CAP 05	Trachyte	0.512611	0.512592	0.1137	0.7832	0.705937	0.705131	-0.53	-0.2	0.71
CAP 14	Gabbro	0.512857	0.512834	0.1390	0.0426	0.704059	0.704015	+4.27	+4.6	0.47
CAP 18	Commendite	0.512682	0.512666	0.1009	71.13	0.769113	0.704690	+0.86	+1.3	0.54
CAP 40	Trachyte	0.512894	0.512872	0.1369	0.7707	0.705943	0.705150	+4.99	+5.3	0.39
CAP 41	Gabbro	0.512658	0.512412	0.1028	0.0320	0.703723	0.703690	+0.39	+0.8	0.58
CAP 53	Commendite	0.512673	0.512653	0.1240	120.48	0.900385	0.767785	+0.68	+1.0	0.69
CAP 58	Basalt	0.512606	0.512874	0.1136	0.0436	0.705084	0.705039	-0.62	-0.3	0.71

The basalt, gabbros, trachytes, and commendites are placed between the end members of the depleted mantle (DM) and the enriched mantle type 1 (EM1), Figure 16. Sample CAP 14 (gabbro) is close to the Hawaii field, while sample CAP 41 is plotted outside the mantle arrangement. Samples CAP 05 (trachyte) and CAP 58 (basalt) are plotted outside and above the mantle arrangement. The trachyte, CAP 40, is plotted in the upper part of the Tristan da Cunha field and inside the Bulk Silicate Earth (BSE). Lastly, the comenditic rocks have higher  $^{87}\text{Sr}/^{86}\text{Sr}_{(\text{m})}$  ratios for CAP 18 is 0.769113, and CAP 53 yielded the value of 0.900385, thus the most radiogenic samples, when observed the  $^{87}\text{Sr}/^{86}\text{Sr}_{(\text{i})}$  ratios the CAP 18 plotted inside the mantle array close to the BSE, and the CAP 53 continuous with a high Sr ratio contain.

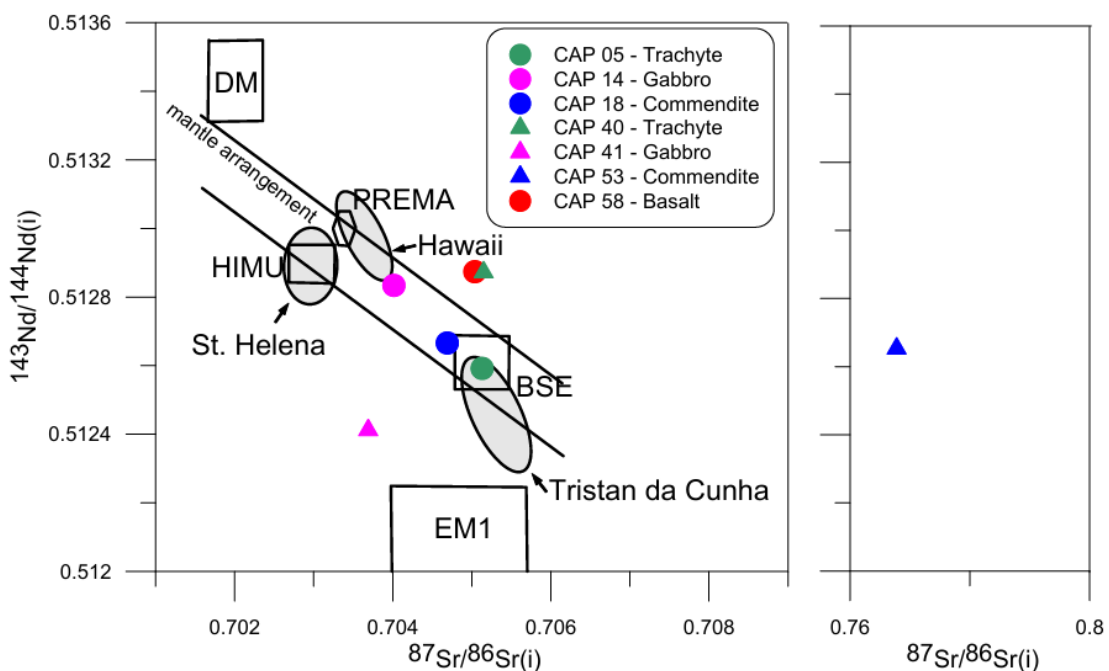


Figure 16 - Relation  $^{143}\text{Nd}/^{144}\text{Nd}(\text{i})$  versus  $^{87}\text{Sr}/^{86}\text{Sr}(\text{i})$  with the addition of pre-established components; the samples studied; mantle arrangement DePaolo and Wasserburg 1977, Zindler et al. 1982); of gray color the oceanic island of Saint Helena (Chaffey et al. 1989), Hawaii (White et al. 1982) and Tristan da Cunha (Rocha-Júnior et al. 2012); and the mantle reservoir (Zindler and Hart 1986). Initial ratios calculated for 26 Ma.

In the  $\epsilon\text{Nd}_{(\text{i})}$  versus  $^{87}\text{Sr}/^{86}\text{Sr}_{(\text{i})}$  diagram (Fig. 17), five samples are plotted to the right of the mantle array. The gabbro sample CAP 14 and the comendite sample CAP 18 fall within the island arc basalt (IAB) field, while samples CAP 05 and CAP 58 are positioned near the IAB field. The gabbro sample CAP 41 is plotted within

the ocean island basalt (OIB) field, close to the Bulk Earth composition. In contrast, samples CAP 40 and CAP 53 are positioned outside these defined fields. According to White (2005), the samples are located in a region indicative of depleted magma sources.

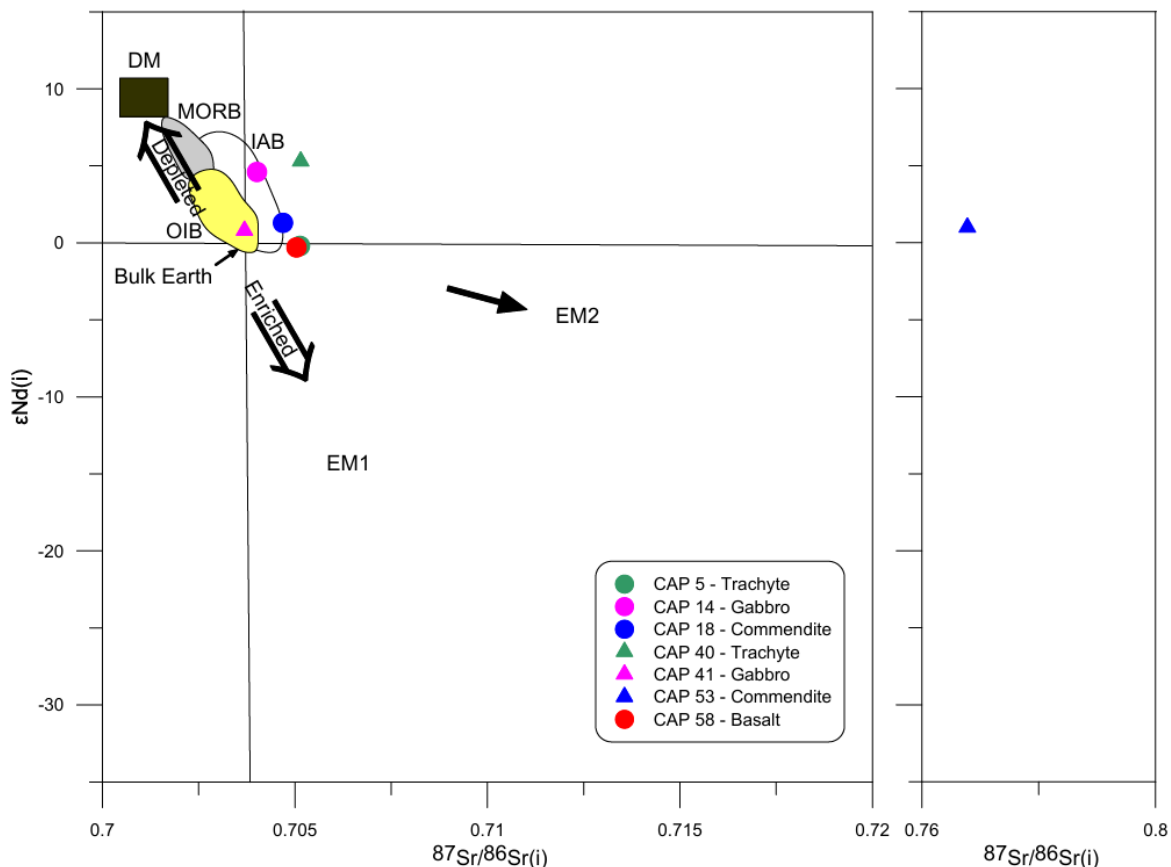


Figure 17 - Relation  $\epsilon_{\text{Nd}}(\text{i})$  versus  $^{87}\text{Sr}/^{86}\text{Sr}(\text{i})$  with the addition of pre-established components; the samples studied; the mantle reservoir (Zindler and Hart 1986); and Depleted and enriched mantle (White 2005); MORB mid-ocean ridge basalts, DM depleted mantle, OIB ocean-island basalts, IAB island-arc basalts. Initial ratios calculated for 26 Ma.

## 5 DISCUSSIONS

### 5.1 Sierra de Apas Volcanic System

The *Sierra de Apas*, part of the *Somuncurá Magmatic Province* (SCMP), presents a diverse range of lithological and evolutionary environments, necessitating various analytical methods to enhance geological understanding of the region. Despite limited previous research on the volcanic body of *Sierra de Apas* (e.g., Croce 1963; Corbella 1975; Corbella and Linares 1977; Remesal 1988;

Ardolino and Franchi 1996; Franchi et al. 2001; Remesal 2001; Remesal et al. 2004), this study contributes valuable insights into the Oligocene-Miocene eruptions in the area.

Approximately 120 samples were collected during fieldwork, with 24 selected for detailed analysis to represent the range of lithologies observed. Although this sample size is insufficient to fully correlate the entire volcanic edifice, it provides a foundation for further data generation, collaboration, and comparison with neighboring ranges, such as *Alta Sierra de Somuncurá*, *Sierras de los Chacays*, *Talagapa*, and *Telsen*. The following methods were applied to the samples: stratigraphic analysis, macroscopic and microscopic examination, microprobe analysis, lithgeochemistry, isotopic analysis, and geochronology.

The investigation began with stratigraphic studies, with volcanic facies classified according to Branney and Kokelaar (2002), McPhie (1993) for volcanic rocks, and Miall (1996) for sedimentary rocks. Eleven lithofacies were identified and grouped into five main units within the Apas volcanic system. The trachytes were classified under the "Trachyte coulées, lava domes, and lavas (and dikes)" unit, comprising porphyritic, banded, massive, coarse, and fine-grained rocks. Pyroclastic samples were categorized in the "PDC deposits" unit, characterized by massive tuffs and well-sorted lapilli-tuffs.

The "Comenditic lava-dome" unit consists of comenditic rocks, distinguished by a very fine aphanitic matrix, feldspar phenocrysts, jigsaw-fit textures, and flow banding. Additionally, two other units—"Basaltic mesa lava flows" and "Subvolcanic bodies"—were identified, representing banded and vesiculated basalts and massive gabbros, respectively.

Field observations, lithologies, lithofacies, lava flows, pyroclastic deposits, and sample descriptions contributed to the development of a geological map of the *Sierra de Apas* volcanic body (Fig. 3), as well as a stratigraphic column (Fig. 18), outlining the sequence of volcanic events ranging from pre-collapse to post-collapse magmatism. This sequence highlights a dynamic volcanic history with varied magma compositions and eruption styles.

The pre-collapse phase is marked by Basalts I and II, which represent early mafic lava flows with rapid effusion and low viscosity, typical of fissure eruptions (Smith & White, 2013). The presence of intrusive gabbros and trachytic lavas reflects the magmatic diversity of the system, ranging from mafic to felsic

compositions (Best, 2003). Trachytic lava flows, rich in alkali feldspar, suggest the presence of viscous, intermediate to felsic magma, often associated with dome or coulée formation due to their high viscosity (Best, 2003).

The syn-collapse phase is characterized by local trachytic lava flows, with coarse-grained lapilli deposits exhibiting parallel stratification, indicating episodic explosive activity and potential changes in vent location or eruption phases (Smith & White, 2013).

Following the caldera collapse, the effusive climax is marked by polycyclic trachytic lavas, indicative of multiple eruptive events, likely driven by shifts in magma chamber dynamics or variations in magma supply rate (Lipman, 2000). The formation of lava cores and roofs suggests rapid cooling during flow emplacement, resulting in solidified crusts around molten cores (Cas & Wright, 1987).

The post-collapse resurgent phase is represented by the formation of a commenditic lava dome, originating from highly evolved rhyolitic magma. Such domes point to advanced magmatic differentiation and degassing processes (Bacon, 1985). Gabbro dikes, indicative of more mafic intrusions, reveal details about the magmatic plumbing system beneath the surface (Best, 2003). Additionally, the presence of trachytic dikes and lava domes suggests ongoing magmatic activity, encompassing both extrusive and intrusive processes.

	Waypoint	Volcanic elements	Volcanic stages
	CAP 57 CAP 56 CAP 53  CAP 54	Commenditic and trachytic lava domes, gabbro and trachitic dikes and basalt III	Post collapse resurgent (crater rim, phase II)
	CAP 40  CAP 31  CAP 26  CAP 12	Polycyclic trachytic lavas	Post collapse caldera rim effusive climax
	CAP 11 CAP 08A CAP 13A	Local trachytic lavas and PDC deposits	Syn collapse magmatism
	CAP 06 CAP 05 CAP 14 CAP 58	Basalts I and II, trachytic lavas and intrusive gabbros	Pre collapse magmatism
<b>References</b> <ul style="list-style-type: none"> <li>[Purple] Commenditic lava dome</li> <li>[Light green] Lava roof</li> <li>[Dark green] Lava core</li> <li>[Red] Basaltic lava flows</li> <li>[Yellow] Parallel stratified coarse-grained lapilli</li> <li>[Orange] Massive lapilli tuffs</li> <li>[Green square] Trachytic lava-dome or coulee</li> <li>[Pink square] Massive Gabbro</li> <li>[// symbol] Trachytic dikes</li> <li>[\\ symbol] Gabbro dikes</li> </ul>			

Figure 19 - Stratigraphic column for Sierra de Apas, indicating waypoints and the interpretations of volcanic elements and stages.

## 5.2 Mineral assembly

Petrographic analyses provide more information about the definitions of lithologies and lithofacies and the development of *Sierra de Apas*. The samples are

classified according to the texture, mainly granulometry, and quantitative mineralogical composition (Wilson 1989). Using these characteristics, the samples can be identified as basalts, gabbros, trachytes, commendites, and tuffs.

The basalts have a porphyritic to glomeroporphyritic texture. The samples are altered, and the mineral iddingsite is derived from the alteration of olivine. The clinopyroxenes, augite, also exhibit evidence of alteration with the inclusion of opaque minerals. The matrix, with disseminated opaques, in turn, shows flow orientation, defined by the orientation of the plagioclases.

The gabbros have an ophitic texture. The samples comprise olivine, clinopyroxene (augite), plagioclase, and opaques. The presence of spherulites with fibrous aggregates of quartz and K-feldspars is also a notable characteristic, indicating devitrification texture. Spherulites are common in acid rocks but also in basic rocks. According to Holness (2002), it results from the early nucleation and growth of plagioclase (probably metastable) forming granophytic intergrowths with quartz, with coarse-grained irregular intergrowths forming after the nucleated alkali feldspar.

Trachytes and commendites have very similar petrographic characteristics. They are porphyritic in texture, with feldspars reaching 1 to 1.5 cm, forming agglomerates. The trachytes also have porphyries of augite. The matrix of both lithologies is very fine, < 0.1 mm, composed of quartz and feldspar. In the trachytes, it is flow-oriented, while in the commendites, it is massive. A petrographic feature found in those rocks is augite crystals, with dissolution features forming a texture known as a "sieve", indicating the instability of these minerals with the magmatic liquid that generates the matrix.

According to Winter (2001), the mixture of magma with different temperatures and volatile content and contamination of the underlying rock can lead to thermal and compositional instability, causing reabsorption, corrosion, and fusion of minerals already formed, changing the composition of the residual magma.

The last lithology analyzed is pyroclastic rock, tuff. Three samples, inequigranular anhedral, contain lithic fragments of trachytes, feldspar, pyroxene, and opaque minerals. The intragranular presence of carbonate is noticeable. Sample CAP 11 shows two distinct parts separated by a linear division, like two depositional cycles. Unfortunately, the sample was not collected in an oriented way.

The microprobe analysis also allows discussions to be developed about the evolution of mineralogy and magma.

The feldspar diagram (Or-Ab-An) shows that the basic samples predominantly plot within the labradorite fields, suggesting these rocks are derived from less involved magmas with moderate amounts of sodium and calcium. In contrast, the felsic rocks lie closer to the sanidine and anorthoclase fields, indicating crystallization from more evolved, potassium-rich magmas formed at lower temperatures (Philpotts & Ague, 2009; Winter, 2010).

The pyroxene diagram (Wo-En-Fs) presents the most basic rocks clustering around the diopside field, typical of crystallization under moderate pressure conditions in deep crustal environments. The augite seen in trachyte samples suggests a more evolved magma that could have formed through fractional crystallization or magma mixing processes (Deer et al. 1992).

The olivine diagram (Tp-Fo-Fa) indicates the basalt and gabbro samples displaying a forsterite composition consistent with mantle-derived magmas that have experienced limited differentiation. The presence of fayalite olivine in some samples suggests either contamination by crustal materials or interaction with more evolved magmas (Best, 2003).

### 5.3 Magma chamber

The lithogeochemical data provide compositional details of major and trace elements, which allow a greater study of the units and lithofacies, developing diagrams and elementary ratios.

A corroborative interpretation of the new data obtained for *Sierra de Apas* (bright colors), combined with references from previous studies in the Somuncura Magmatic Province (dark gray), Figure 19. The data compiled are Stern (1987), Ardolino (1995), Marquez et al. 2010; Remesal and Maro (2012); Asiain (2016), Asiain (2017), and Remesal and Salani (2018), which studied basalts, basaltic trachy-andesites, trachytes and rhyolites domes.

The samples analyzed range in SiO<sub>2</sub> content from 42 wt.% to 78 wt.%. The TAS diagram (total alkalis *versus* silica) proposed by Le Maitre et al. (1989) shows

the data grouped into two groups, marked by gray areas, with lower and higher silica content.

It is important to mention the absence of intermediate rocks in this set of samples. On the other hand, looking at examples of igneous rocks from the basement (light gray), Pankhurst and Rapela (1995), Rapela (2005), and Zaffarana (2020), such as dacites, andesites, granites, and rhyolites, outcropping on the edges of the SCMP, the presence of intermediate rocks can be seen.

Recent experimental works by Salar-Naranjo and Vlach (2023) relate oxygen fugacity ( $f\text{O}_2$ ) to silica saturation. According to Pilet et al. (2010), basanites are the main parental candidates of the alkaline magmatic series, so these will be considered the parental liquid of the samples studied. Thus, the generation of alkaline liquids is differentiated from primary ultrabasic magmas in terms of the set of minerals and their composition.

The ultrabasic basanitic evolved as a sodic liquid under 1 atmosphere (atm) and 1,150–1,000 °C (lower temperature), producing more evolved melts. Under low to high pressures and reduced conditions, the main evolution trend is marked by the increase in the total alkalis with minor variations in  $\text{SiO}_2$  contents.

A 1 atm experiment better comprehends the  $f\text{O}_2$  effects on melt evolution. The glasses derived from the ultrabasic basanite parental magmas can generate large amounts of evolved sodic melts during equilibrium crystallization.

The author's experiments involve Ti-clinopyroxenes, and considering that all the lithologies studied present Ti-augites, these observations can be considered. The mutual substitution of  $\text{Ti}^{+4}\text{Si}^{+4}$  occurs mainly at low pressures, with an increase in the concentration of Ti in clinopyroxenes.

These experiments can explain the high silica ratios and the absence of intermediate ends in the magmatic evolution of the *Apas* volcanic system, with increasingly silicic melts.

The alkaline character of the samples is another significant chemical aspect. The line proposed by Irvine & Baragar (1971) on the TAS diagram reveals this and may extrapolate to the samples compiled contemporaneously, as well as the  $\text{Nb/Y} > 1$  ratio proposed by Winchester & Floyd (1977).

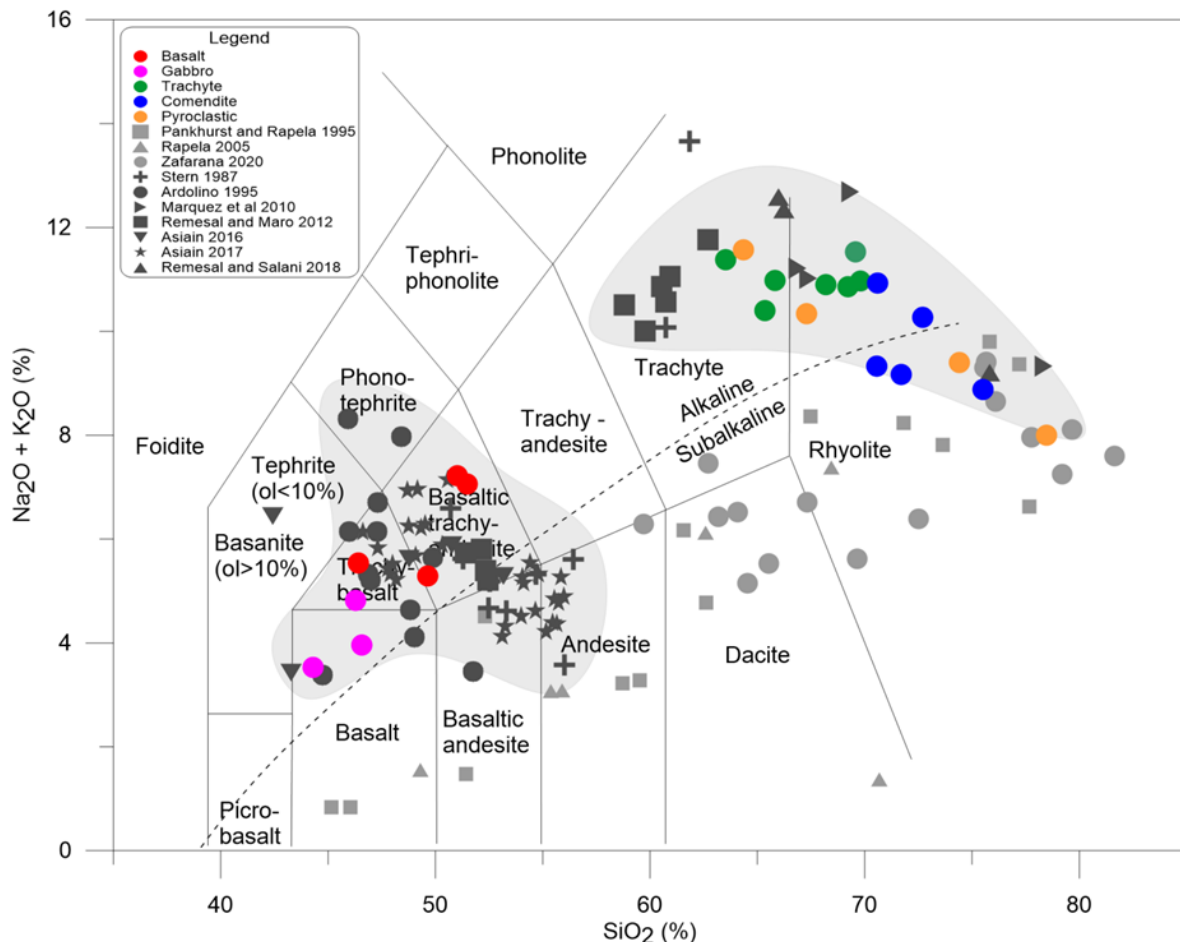


Figure 19- TAS diagram (total alkalis *versus.* silica) proposed by Le Maitre et al. (1989), where compiled new data from the *Sierra de Apas*, with contemporary lithological references, Stern (1987); Ardolino (1995); Marquez et al. 2010; Remesal and Maro (2012); Asiain (2016); Asiain (2017); and Remesal and Salani (2018) - dark gray, and with basement rocks nearby the SCMP, Pankhurst and Rapela (1995); Rapela (2005); and Zaffarana (2020) - light gray, there are two main groups of samples, highlighted by the gray fields.

Additionally, Shand (1943) diagram uses the molar ratios, A/NK = Al<sub>2</sub>O<sub>3</sub>/(Na<sub>2</sub>O + K<sub>2</sub>O) and A/CNK = Al<sub>2</sub>O<sub>3</sub>/(CaO + Na<sub>2</sub>O + K<sub>2</sub>O), to determine the alumina saturation index (ASI), as seen in Fig. 9C. The samples are classified as Metaluminous and Peralkaline, basic and felsic rocks, respectively. The peralkaline character of the comenditic and trachytic samples can be emphasized by the Zr content (ppm), with values between 600 and 2,000 ppm.

As previously presented in the Geochronology section, the presence of zircons is very limited. The high concentrations of Zr, Hf, Nb, and Ta are linked to the enhanced solubility of these elements in alkaline melts via high melt temperatures (Hoshino et al. 2016).

The effects of Andean subduction on the Oligo-Miocene magmatism of Apas and their influence on the development of the volcanic system will be considered. Allowing the introduction that solute-rich supercritical fluids, especially those with peralkaline compositions, are, therefore, effective agents for transferring Zr and other HFSEs in subduction zones. The solubility of zircon in solute-rich supercritical fluids is 1 to 2 orders of magnitude greater than in dilute aqueous fluids (Chen et al. 2021).

A dominant characteristic in the variation diagrams is the separation of the samples studied into two groups, major and trace elements (Figs. 10 and 11), besides a gap between the groups referring to the intermediate rocks, as in the TAS diagrams. A dominant characteristic in the variation diagrams is the separation of the samples studied into two groups, major and trace elements (Figs. 10 and 11), besides a gap between the groups referring to the intermediate rocks, as in the TAS diagrams. The oxides directly reflect the mineralogy, and together with the rare earth elements (REE), incompatible elements, indicate that the genesis of the magma may be related to evolution by variations in the degree and depth of melting and even by the mixing of magmas, where fractional crystallization would be the main process controlling the compositional variation in these rocks (Remesal 1988).

The samples analyzed are enriched in incompatible elements, mainly in the acidic ones. There are negative Ba and Sr anomalies and positive Rb and Zr anomalies in the trachytes, commendites, and tuffs (Fig 12A).

The behavior of the samples in the normalized chondrite diagram is concordant. This would indicate different sources for the samples, while the less and most differentiated samples overlap. The samples show a similar behavior to the LCC, with the more differentiated samples having Eu anomalies, which agrees with the UCC.

According to Wedepohl (1974), Sr is concentrated in plagioclase of intermediate composition and subordinately in potassium feldspar, which is why the separation of plagioclase led to this depletion of Sr. According to the same author, Ba is more easily accepted in potassium feldspar and micas, but this is linked to the fractionation of andesine-oligoclase, which consumed a large part of the existing Ba. The positive Rb and Zr anomaly is related to increased magmatic differentiation.

Furthermore, using the results of lithogeochemistry in whole rock, some ratios are applied in diagrams such as Nb/Yb vs. Th/Yb from Pearce (2008) to

enable interpretation of the environment and provenance of the rocks studied (Fig. 13). The basic samples are plotted in the field of alkaline rocks close to the composition of the OIB, while the acidic rocks are in the crustal recycling and contamination zones.

Salavati, M. (2008) states that basaltic rocks affected by crustal contamination have  $K/P > 7$ ,  $La/Ta > 22$ , and  $La/Nb > 1.5$ . The values obtained to study samples corroborate that crustal contamination of basic rocks is minimal or non-existent, showing ratios  $K/P < 3.52$ ,  $La/Ta < 15.44$ , and  $La/Nb < 0.88$  (Table 5).

#### **5.4 Sierra de Apas Ages**

One of the significant advancements presented in this study is the application of the U-Pb dating method to two trachyte samples, CAP 26 and CAP 40, using apatite minerals. Initial expectations regarding the presence of zircon in these samples were based on the previously noted high zirconium (Zr) content; however, thin section analyses suggested the absence of zircon crystals.

According to Chew et al. (2011), the high ratios of common radiogenic lead (Pb), or initial Pb, pose challenges for dating using apatite, as it typically does not achieve the same precision as zircon dating. Nevertheless, Chew et al. (2011, 2021) have demonstrated that apatite can yield very discordant U-Pb dates due to its tendency to incorporate common Pb (Pbc). This issue is particularly pronounced in young samples, which have had insufficient time to accumulate significant amounts of radiogenic Pb(Pb\*), as well as in apatites with low uranium (U) concentrations. Although corrections for the presence of Pbc can be applied, doing so for samples with high Pbc/Pb\* ratios can lead to substantial age uncertainties and potentially imprecise dates if the initial Pb composition used in the correction is inadequate.

This study employed two reference standards: Durango for downhole correction normalization and Sumé for quality control. Additionally, plateau and post-plateau rocks in the region were analyzed using K/Ar and  $^{40}\text{Ar}/^{39}\text{Ar}$  dating methods (e.g., Ardolino 1981; Ramos and Kay 1992; Gorring et al. 1997). The ages obtained from these analyses range from 33 to 11 Ma, representing basaltic flows from the Somuncura Magmatic Province.

The ages reported in this study pertain specifically to trachytic rocks, which date to the Upper Oligocene, with an average age of  $26.19 \pm 1.54$  Ma. This finding is corroborated by data from Cordenons et al. (2020), which present  $^{40}\text{K}/^{39}\text{Ar}$  ages for trachytes and olivine basalts at *Cerro Marabella*, dated at  $26 \pm 3$  Ma. Furthermore, the *Apas Volcanic Complex* (AVC) trachytes are reported to have ages of  $28 \pm 2$  Ma, suggesting they occurred prior to the formation of the olivine basalts in the *Loma Larga* region. Peralkaline trachytic dikes have also been dated at  $31 \pm 2$  Ma (Corbella and Linares, 1977). More recent silicic lavas, such as the *Cerro Colorado* comenditic dome, and a trachyte near *Puesto Contreras*, dated at  $19 \pm 2$  Ma, are covered by mafic flows.

Overall, the stratigraphic and geochronological evidence indicates a prolonged and recurrent magmatic history, spanning approximately 10 to 15 Ma, which contributes to the complex evolutionary narrative of the region (Ardolino and Franchi, 1996).

## 5.5 Model implications

The isotopic analyses (Table 5), presented for the 7 samples, provide data for a range of rock samples, including trachyte, gabbro, comendite, and basalt, with values for Nd and Sr isotopic ratios, epsilon Nd ( $\epsilon\text{Nd}$ ), and depleted mantle model ages ( $T_{\text{DM}}$ ). These data offer valuable insights into these rock's petrogenesis, source characteristics, and evolutionary history, allowing for correlations with the Somuncurá Magmatic Province and regional basement rocks.

The Nd isotopic compositions of the samples show a range of  $\epsilon\text{Nd}$  values, reflecting different magmatic sources and processes. For instance, CAP 14 (gabbro) exhibits a notably higher  $\epsilon\text{Nd}$  value of + 4.27 compared to CAP 41 (gabbro) with + 0.39. This suggests that CAP 14 likely has a more juvenile or less contaminated source, while higher  $\epsilon\text{Nd}$  values indicate a younger, more depleted mantle source (Elliott et al. 1999).

The trachytes (CAP 05 and CAP 40) also display significant variations in  $\epsilon\text{Nd}$ , with values of - 0.53 and + 4.99, respectively. These variations can be attributed to different degrees of interaction with the mantle and crustal contamination. Lower  $\epsilon\text{Nd}$  values in CAP 05 suggest more substantial crustal

contamination or an older source, while the higher  $\epsilon_{\text{Nd}}$  in CAP 40 indicates a relatively less contaminated or more juvenile mantle source (Taylor & McLennan, 1995; Zindler & Hart, 1986).

The Sr isotopic compositions complement these observations. For example, CAP 14 has an  $^{87}\text{Sr}/^{86}\text{Sr}$  ratio of 0.704059, indicating less crustal contamination than CAP 41, which has a ratio of 0.703723. This supports the notion that higher Sr ratios reflect significant interaction with crustal material (Hofmann, 1997). The trachytes and commendites show varying Sr ratios, which align with models suggesting that different degrees of crustal contamination influence magmatic compositions (Kelley et al. 2006).

The  $T_{\text{DM}}$  values provide insights into the crustal contributions and magmatic evolution histories. For instance, CAP 05 has a  $T_{\text{DM}}$  value of 0.71, indicating a relatively older crustal involvement, while CAP 14 has a lower  $T_{\text{DM}}$  value of 0.47, suggesting a younger or less evolved crustal source. Lower  $T_{\text{DM}}$  values are often associated with more juvenile or less contaminated sources (Albarede, 1998; White & Hofmann, 1982), which align with the higher  $\epsilon_{\text{Nd}}$  values observed for CAP 14.

Integrating major and trace element data with isotopic considerations reveals that multiple geodynamic factors, including Andean subduction, mantle plumes, and crustal contamination, contributed to the genesis of the magmas in the Somuncurá Magmatic Province (Kay et al. 1999; Lucassen et al. 2002).

Figure 20 (A and B), compares MgO vs. initial isotopic ratios, there is clear evidence of fractional crystallization (FC) and assimilation with fractional crystallization (AFC) processes. The Figura 20C, presented the diagram Nb versus La, allowing the interpretation of FC as the evolutionary process for the volcanic sequence in the *Sierra de Apas*. The fractional crystallization trends seen here are common in intraplate settings where primary basaltic magmas evolve to form more silica-rich compositions like trachytes and rhyolites (Wilson, 1989). This is consistent with the presence of basaltic, gabbroic, and trachytic compositions in the *Sierra de Apas*.

Deviations from simple FC trends indicate the influence of AFC processes. Certain samples, particularly the more evolved trachytes, and commodities, show signs of crustal contamination, a process well-documented in many continental volcanic provinces (DePaolo, 1981).

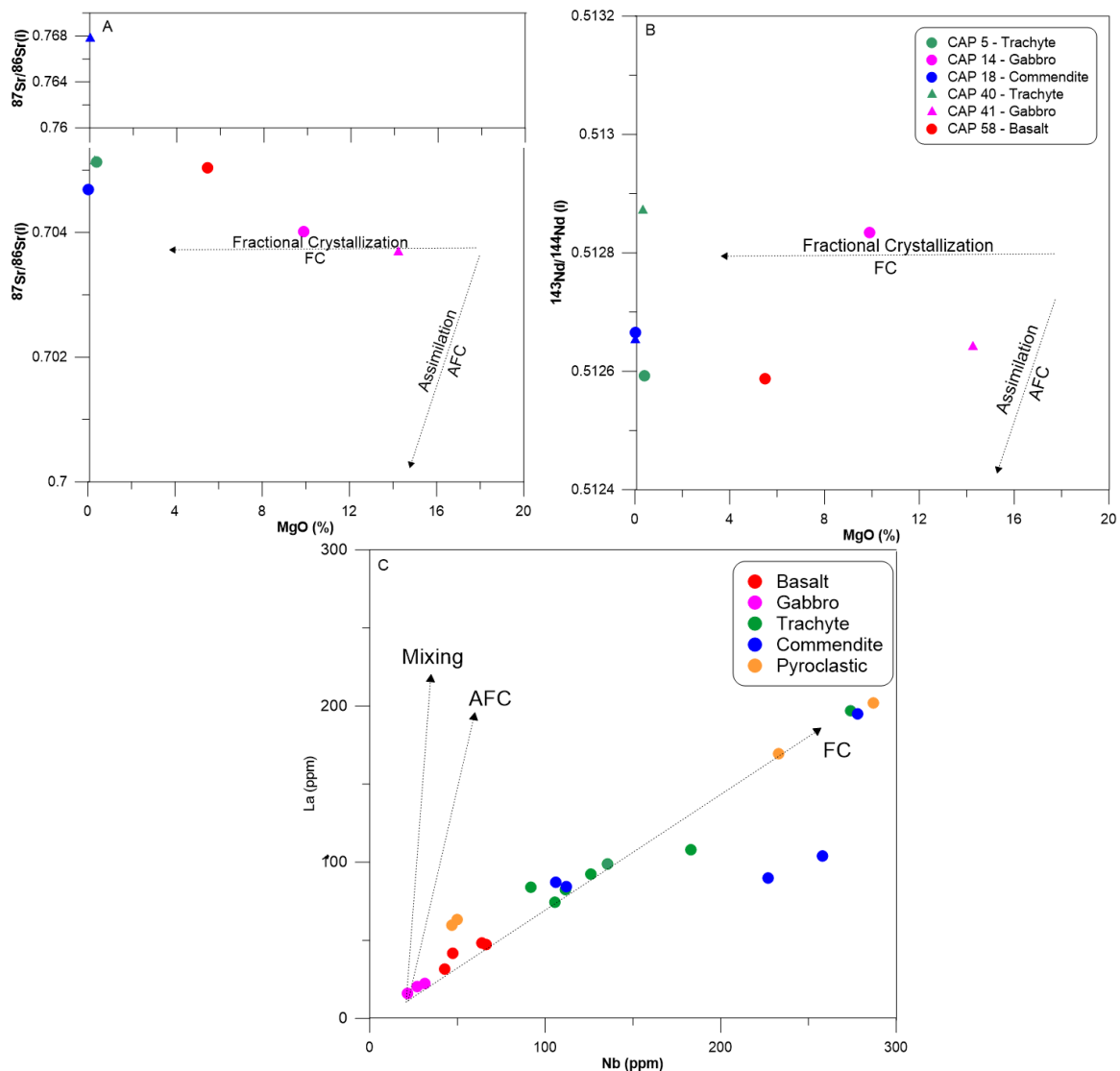


Figure 20 - Diagrams of interpretation modeling for *Sierra the Apas* (A) The variation of MgO vs.  $^{87}\text{Sr}/^{86}\text{Sr}_{(i)}$ , (B) MgO vs.  $^{143}\text{Nd}/^{144}\text{Nd}_{(i)}$  diagram, and (C) Nb vs. La diagram.

The diagrams comparing trace element ratios like Ba/Th vs. Th/Nb and Sr/La vs. Th/Yb (Fig. 21) reveal a significant influence from subduction-derived components. These ratios are commonly used as indicators of subduction influence, where fluids released from the dehydrating slab enrich the mantle wedge in Ba and Sr (Hawkesworth et al. 1997; Pearce & Peate, 1995).

Elevated Ba/Th and Sr/La (Fig. 21A) ratios suggest the influence of subduction-derived fluids in the magmatic source, particularly for the basaltic and gabbroic samples. These enrichments align with arc setting findings, where slab-derived fluids modify the mantle wedge before magma generation (Turner et al. 1996). This suggests that despite the intraplate tectonic setting, the Somuncura

magmatism still bears a geochemical signature of the Andean subduction to the west.

The lower Th/Nb and Th/Yb (Fig. 21B) ratios in some samples, particularly the less evolved basalts, imply minimal sedimentary input from the subducting slab. This is consistent with models of mantle plumes interacting with a subduction-modified lithospheric mantle (Murphy et al. 1998). The clear dichotomy between high Ba/Th and low Th/Yb values in different samples indicates that some magmas tapped a mantle source modified by slab fluids, while others may reflect a more pristine mantle plume component.

Although subduction signals are apparent in several samples, the overall geochemical signature of the magmas also suggests a mantle plume component. The low Th/Yb ratios in some of the basalts and pyroxenites are consistent with melting in a plume-derived source, as these values typically reflect a deeper, less depleted mantle source unaffected by subduction inputs (Hofmann, 1997).

Mantle plumes are often associated with large igneous provinces (LIPs) and intraplate volcanic activity (Campbell & Griffiths, 1990). In the Somuncurá Province, the presence of primitive basaltic compositions alongside more evolved trachytic and rhyolitic rocks suggests the contribution of a mantle plume, likely originating from a deep-seated thermal anomaly (Richards et al. 1989).

The isotopic and trace element data indicate that while a mantle plume may have initiated the magmatic activity, interaction with a subduction-modified lithosphere and crustal contamination processes further altered the magma. This hybrid geochemical signature, seen in the elevated Sr/La and Ba/Th ratios, supports a model where mantle plume magmatism was modified by the pre-existing Andean tectonic setting (Storey et al. 2012).

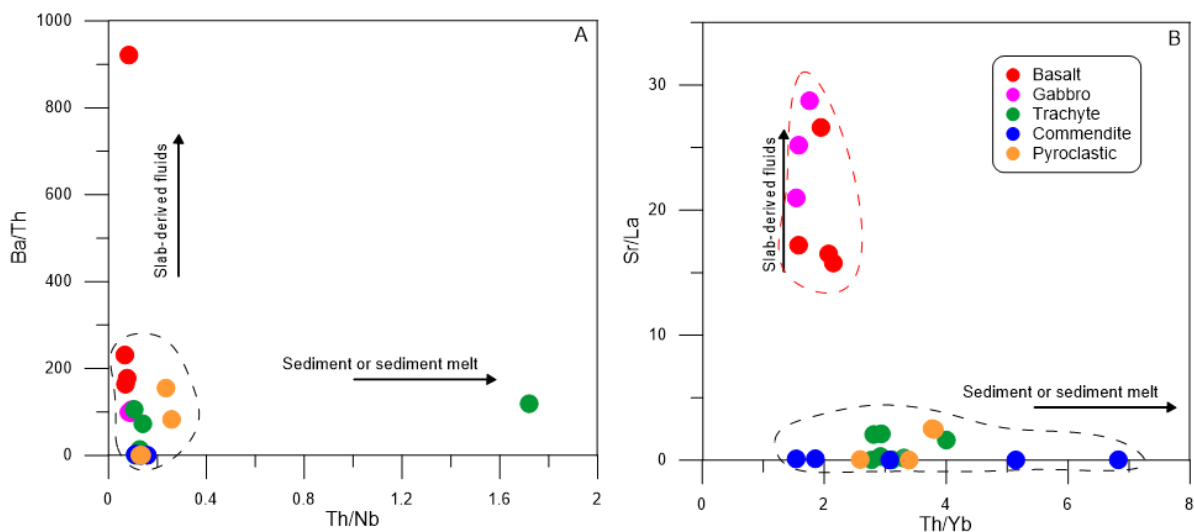


Figure 21 - Diagrams of interpretation modeling for *Sierra de Apas* (A) Th/Nd vs. Ba/La diagram (Shaw, 1970) that indicates all the samples follow the slab-derived fluid melt array, and (B) Th/Yb vs. Sr/La diagram (Li et al. 2017).

The assimilation of crustal material during magma evolution is evident from both the trace element trends and isotopic data. Previous studies have shown that contamination with crustal rocks significantly alters the isotopic ratios of Sr, Nd, and Pb, increasing the magma's radiogenic components (DePaolo, 1981; Hildreth & Moorbath, 1988). This contamination is particularly visible in some evolved trachytic and comenditic rocks, which show the highest degrees of differentiation.

Based on our previous discussions, isotopic data from *Sierra de Apas* samples likely reveal a mixed source with mantle-derived and crustal materials contributions. The AFC processes reflected in the diagrams would increase the  $^{87}\text{Sr}/^{86}\text{Sr}$  ratios and lower the  $^{143}\text{Nd}/^{144}\text{Nd}$  values, indicating contamination by older, radiogenic crust. This is consistent with other studies of Andean magmatism, where crustal assimilation is a key factor in generating more evolved magmas (Kay et al. 1999).

The Nd isotopic ratios, in particular, can help differentiate between a purely plume-derived source and one that has interacted with the lithosphere. As seen in other continental volcanic provinces, high  $^{87}\text{Sr}/^{86}\text{Sr}$ , and low  $^{143}\text{Nd}/^{144}\text{Nd}$  values suggest significant interaction with ancient continental crust (McCulloch & Gamble, 1991).

## 6 CONCLUSIONS

The *Sierra de Apas*'s magmatic evolution within the *Somuncurá* Magmatic Province reveals a complex volcanic history spanning from pre- to post-collapse phases. This study identifies a diverse range of lithologies, from basalts to highly evolved rhyolites, and characterizes eleven lithofacies across five main units, reflecting a dynamic system shaped by varied magmatic compositions and eruption styles.

The mineralogical diversity and ternary diagrams indicate a dynamic magma chamber environment where fractional crystallization and magma mixing are pivotal. Hybrid mineral compositions across different rock types suggest frequent magma injections into an evolving chamber, supporting the magma mixing hypothesis.

The lithogeochemical analysis further highlights the evolution of alkaline magmas from ultrabasic basanitic sources, driven primarily by fractional crystallization under variable pressure and temperature conditions. The distinct compositional groups, marked by high silica, zirconium, and rare earth elements, suggest the influence of Andean subduction and the role of solute-rich supercritical fluids in mobilizing high-field strength elements.

The isotopic evidence from the *Somuncura* Magmatic Province, specifically in the *Sierra de Apas* region, reveals a magmatic system influenced by mantle plume activity and subduction-related processes. The diverse isotopic signatures, including the radiogenic Nd and variable Sr ratios, indicate a multi-source origin, with contributions from a depleted mantle plume, enriched lithospheric mantle, and continental crust. These findings are consistent with the region's complex geodynamic environment, where intraplate magmatism is modified by crustal processes linked to Andean subduction.

The *Somuncurá* Magmatic Province exemplifies a hybrid tectonic setting where intraplate magmatism driven by mantle plumes is significantly influenced by subduction processes. The geochemical and isotopic evidence points to a modified mantle source, where subduction-derived sediments and fluids interact with upwelling mantle material, resulting in a unique magmatic signature.

Overall, this research provides crucial insights into the magmatic processes of the *Sierra de Apas*, contributing significantly to the understanding of Oligocene-Miocene volcanic activity in the region. It establishes a foundational framework for

further studies and correlations with adjacent volcanic systems, advancing our knowledge of the region's volcanic and tectonic history.

## 7 ACKNOWLEDGMENTS

Msc. Gilmar Pachá would like to thank the cooperation with the laboratory and the laboratory technician who helped me to develop the analyses, Gabriela from LGPA/UERJ; Wagner from Multilab/UERJ; Carla Neto, Gilberto da Silva Vaz, João Ricardo Coutinho and Claudio Valeriano from LAGIR/UERJ for the Sr-Nd analysis during the COVID-19 pandemic; Also, he would like to thank Dr. Roberto Ventura, Dr. Guilherme Gonçalves and Dr. Tiago Jalowitzki from LEGGA/UnB; Dr. Júlio Mendes, Iara Ornelas and Amanda Tosi from LABSONDA/UFRJ; and *Laboratorio de Petrotomía* from INGEOSUR-UNS. Dr. Anderson Santos would like to thank CNPq PQ 2021 Process nº 304837/2021-0 for all support. Dr. Anderson Santos would like to thank the research groups from which he has developed several partnerships, such as GeoBioTec (Aveiro University, Portugal), Dom Luiz Institute (Lisboa University, Portugal), Tektos Group and GeoAtlantic Institute (Rio de Janeiro State University, Brazil). He would also to thank the *Universidade do Estado do Rio de Janeiro* for the PROCAD Program (Capacitation Program) leave and CAPES [Process 88.881.177228/2018-01] for the postdoctoral fellowship to execute part of this research at Aveiro University and Lisboa University, Portugal, and FAPERJ [Entidades Estaduais 2018 nº 210.297/2018; APQ1 2019 nº 210.179/2019; JCNE 2022 nº 201.469/2022].

## REFERENCES

- ALBAREDE, F., 1998. Geochemistry: An Introduction. Cambridge University Press.
- AMEGHINO FLORENTINO, 1898. Sinopsis geológico-paleontológica de la Argentina. "Segundo Censo de la República Argentina" (mayo 10 de 1895), t. I, Territorio. Buenos Aires.
- ARAGÓN, E., D'ERAMO, F., CASTRO, A., PINOTTI, L., BRUNELLI, D., RABBIA, O., RIVALENTI, G., VARELA, R., SPACKMAN, W., DEMARTIS, M., CAVAROZZI, C.E., AGUILERA, Y.E., MAZZUCHELLI, M., & RIBOT, A. (2011). Tectono-magmatic response to major convergence changes in the North Patagonian suprasubduction system; the Paleogene subduction-transcurrent plate margin transition. *Tectonophysics*, 509(3-4), 218-237.
- ARDOLINO, A.A., 1981. El volcanismo cenozoico del borde suroriental de la meseta de Somuncurá. Provincia del Chubut. 8º Congreso Geológico Argentino. Actas 1:65 y3:7-23.
- ARDOLINO A.A. Y FRANCHI, M.R, 1993. El volcanismo cenozoico de la Meseta de Somún Cura Provincias de Río Negro y Chubut. 12º Congreso Geológico Argentino y 2º Congreso de Exploración de Hidrocarburos, Actas 4:225-235.
- ARDOLINO A.A. & FRANCHI, M. (1996). Hoja Geológica 4366-I Telsen.
- ASIAIN, L. M., GARGIULO, M. F., REITINGER, J., NTAFLOS, T., & BJERG, E. A. (2016). Petrografía y geoquímica de basanitas del sector oeste de la Meseta de Somuncurá, provincia de Río Negro.
- ASIAIN, L. M., GARGIULO, M. F., REITINGER, J., NTAFLOS, T., & BJERG, E. A. (2017). Petrografía y geoquímica de lavas básicas del sector noroeste de la Meseta de Somuncurá, provincia de Río Negro
- BACON, C. R. (1985). Implications of silicic vent patterns for the presence of large crustal magma chambers. *Journal of Geophysical Research: Solid Earth*, 90(B13), 11243-11252.
- BARBIERI, M. Y CORBELLA, H., 1987. Relaciones  $^{87}\text{Sr}/^{86}\text{Sr}$  de las rocas alcalinas de la sierra de los Chacays y edad de las volcanitas potásicas del cerro Planluán, Patagonia Extrandina, Chubut, Argentina. 10º Congreso Geológico Argentino, Actas 4:186-187.
- BEN-AVRAHAM, Z. V. I. et al. 1981. Continental accretion: from oceanic plateaus to allochthonous terranes. *Science*, v. 213, n. 4503, p. 47-54.
- BERTOTTI, Anelise Losangela. 2005. Metodologia Samário/Neodímio: uma abordagem analítica simplificada e alguns exemplos aplicativos.
- BEST, M.G. 2003. Igneous and Metamorphic Petrology. Wiley-Blackwell.
- BRANNEY, M. J., & KOKELAAR, B. P. (2002). Pyroclastic density currents and the sedimentation of ignimbrites. Geological Society of London.

- BUSTEROS, A., GIACOSA, R. Y LEMA, H., 1998. Hoja geológica 4166- IV, Sierra Grande, provincia de Río Negro. Instituto de Geología y Recursos Minerales. Boletín 241:I-75.
- CAMINOS, R., 1999. Hoja geológica 4166- 1, Valcheta, provincia de Río Negro. Instituto de Geología y Recursos Minerales, inédito.
- CAMPBELL, I.H. & GRIFFITHS, R.W., 1990. Implications of mantle plume structure for the evolution of flood basalts. *Earth and Planetary Science Letters*, 99, 79-93.
- CAS, R. A. F., & Wright, J. V. (1987). Volcanic successions: Ancient and modern. Allen and Unin, London.
- CHAFFEY, D. J., CLIFF, R. A., & WILSON, B. M. (1989). Characterization of the St Helena magma source. *Geological Society, London, Special Publications*, 42(1), 257-276.
- CHEN, W., XIONG, X., & TAKAHASHI, E. (2021). Zircon Solubility in Solute-Rich Supercritical Fluids and Zr Transfer From Slab to Wedge in the Deep Subduction Process. *Journal of Geophysical Research: Solid Earth*, 126(9), e2021JB021970.
- CHEW, D. M., SYLVESTER, P. J., & TUBRETT, M. N. (2011). U-Pb and Th-Pb dating of apatite by LA-ICPMS. *Chemical Geology*, 280(1-2), 200-216.
- CHEW, D. M., PETRUS, J. A., & KAMBER, B. S. (2014). U-Pb LA-ICPMS dating using accessory mineral standards with variable common Pb. *Chemical Geology*, 363, 185-199.
- CHEW, D. M., & SPIKINGS, R. A. (2021). Apatite U-Pb thermochronology: A review. *Minerals*, 11(10), 1095.
- CONDIE, K. C. (2001). *Mantle plumes and their record in Earth history*. Cambridge university press.
- CORBELLA, H. (1975). Diseño radial de diques traquíticos en la sierra de Apas, Macizo Nordpatagónico, provincia de Río Negro, Argentina. *Revista de la Asociación Geológica Argentina*, 30(1), 110-11.
- CORBELLA, H., & LINARES, E., 1977. Acerca de la naturaleza peralcalina y la edad de algunos afloramientos volcánicos de la Sierra de Apas y de la Sierra Negra de Telsen, Macizo Nordpatagónico, provincias de Río Negro y Chubut, Argentina. *Revista de la Asociación Geológica Argentina*, 32(2), 152.
- CORBELLA, H., 1982. Naturaleza litológica del complejo alcalino sierra de Queupuniyu, Patagonia Extraandina norte, Argentina. V Congreso Latinoamericano de Geología, Actas II, 197-211. Buenos Aires.
- CORDENONS, P. D. (2017). *Geología y petrología del Complejo Volcánico Sierra de los Chacays, Provincia de Chubut, Patagonia extraandina* (Doctoral dissertation, Universidad de Buenos Aires. Facultad de Ciencias Exactas y Naturales).
- CORDENONS, P. D., REMESAL, M. B., SALANI, F. M., & CERREDO, M. E. (2020). Temporal and spatial evolution of the Somún Curá magmatic province,

northern extra-andean Patagonia, Argentina. *Journal of South American Earth Sciences*, 104, 102881.

CROCE, R. (1963). *El sistema del somuncura las altas sierras del somuncura y sus aledaños*. El Museo.

CUCCHI, R., BUSTEROS, A. Y LEMA, H., 1999. Hojageológica 4169- II, Los Menucos, provincia de Río Negro. Instituto de Geología y Recursos Minerales, inédito.

DE IGNACIO, C., LÓPEZ, I., OYARZUN, R., & MÁRQUEZ, A. (2001). The northern Patagonia Somuncura plateau basalts: a product of slab-induced, shallow asthenospheric upwelling?. *Terra Nova*, 13(2), 117-121.

DEER. W.A., HOWIE, R.A., ZUSSMAN, J. 1992. Rock forming minerals. Londres, Longman, 558p.

DEPAOLO, D. J., & WASSERBURG, G. J. (1977). The sources of island arcs as indicated by Nd and Sr isotopic studies. *Geophysical Research Letters*, 4(10), 465-468.

DEPAOLO, D.J. (1981). Trace element and isotopic effects of combined wallrock assimilation and fractional crystallization. *Earth and Planetary Science Letters*, 53(2), 189-202.

DOERING, A., 1882. Informe oficial de la Comisión científica agregada al Estado Mayor General de la expedición al Río Negro. Entrega, 3, 401-430.

EAGLES, G., & SCOTT, B. G. (2014). Plate convergence west of Patagonia and the Antarctic Peninsula since 61 Ma. *Global and Planetary Change*, 123, 189-198.

ELLIOTT, T., HAWKESWORTH, C., & KEMP, A., 1999. The Role of Mantle Plumes in the Generation of Continental Flood Basalts. *Nature*, 398, 682-686.

ENCINAS, A., FOLGUERA, A., OLIVEROS, V., DE GIROLAMO DEL MAURO, L., TAPIA, F., RIFFO, R., HERVÉ, F., FINGER, K.L., VALENCIA, V.S., GIANNI, G., & ÁLVAREZ, O. (2016). Late Oligocene–early Miocene submarine volcanism and deep-marine sedimentation in an extensional basin of southern Chile: Implications for the tectonic development of the North Patagonian Andes. *Bulletin*, 128(5-6), 807-823.

ERNST, R. E., & BUCHAN, K. L. (2003). Recognizing mantle plumes in the geological record. *Annual Review of Earth and Planetary Sciences*, 31(1), 469-523.

FERNÁNDEZ PAZ, L., BECHIS, F., LITVAK, V. D., ECHAURREN, A., ENCINAS, A., GONZÁLEZ, J., LUCASSEN, F., OLIVEROS, V., VALENCIA, V., & FOLGUERA, A. (2019). Constraints on trenchward arc migration and backarc magmatism in the North Patagonian Andes in the context of Nazca Plate Rollback. *Tectonics*, 38(11), 3794-3817.

- FIGARI, E.G., 2005. Evolución Tectónica de la Cuenca de Cañadón Asfalto. Tesis Doctoral 3896, Facultad de Ciencias Exactas y Naturales, Universidad Nacional de Buenos Aires. Biblioteca Digital FCEN-UBA, 198 pp.
- FLORES, M. A., 1956. Perfiles en el Chubutiano y observaciones geológicas en parte central y norte de Chubut. YPF, Informe inédito, Buenos Aires.
- FLORES, M. A. (1957). Perfiles En El Chubutiano (II Parte). YPF, Informe Inédito, Buenos Aires.
- FRANCHI, M. R., & SEPÚLVEDA, E. G., 1983. Descripción geológica de la hoja 41h Cona Niyeu, provincia de Río Negro. Servicio Geológico Nacional., Informe inédito. Buenos Aires
- FRANCHI, M., REMESAL, M. Y ARDOLINO, A., 1998. Hoja geológica 4166- III, Cona Niyeu, provincia de Río Negro. Instituto de Geología y Recursos Minerales, inédito.
- FRANCHI, M., ARDOLINO, A. A., REMESAL, M., CABALLERO, R., DALPONTE, M. R., & LIZUAÍN, A. (2001). Hoja Geológica 4166-III Cona Niyeu.
- GERALDES, M. C. 2010. Introdução à geocronologia. SBG-Sociedade Brasileira de Geologia.
- GORRING, M. L., KAY, S. M., ZEITLER, P. K., RAMOS, V. A., RUBIOLO, D., FERNANDEZ, M. I., & PANZA, J. L. (1997). Neogene Patagonian plateau lavas: continental magmas associated with ridge collision at the Chile Triple Junction. *Tectonics*, 16(1), 1-17.
- HARRISON, L. N., WEIS, D., & GARCIA, M. O. (2017). The link between Hawaiian mantle plume composition, magmatic flux, and deep mantle geodynamics. *Earth and Planetary Science Letters*, 463, 298-309.
- HAWKESWORTH, C.J., GALLAGHER, K., HERGT, J.M., & McDERMOTT, F., 1997. Mantle and slab contributions in arc magmas. *Annual Review of Earth and Planetary Sciences*, 25, 175-208
- HERRON, E., HEITZLER, J. (1967). Sea-floor spreading near the Galapagos. *Science*, 158: 775-780.
- HOFMANN, A. W., 1988. "Chemical Differentiation of the Earth: The Relationship between Mantle, Continental Crust, and Oceanic Crust". *Earth and Planetary Science Letters*, 90, 297-314.
- HOLNESS, M. B. (2002). Spherulitic textures formed during crystallization of partially melted arkose, Rum, Scotland. *Geological Magazine*, 139(6), 651-663.
- HONDA, S., ORIHASHI, Y., MIBE, K., MOTOKI, A., SUMINO, H., & HALLER, M. J. (2006). Mantle wedge deformation by subducting and rotating slab and its possible implication. *Earth, planets and space*, 58, 1087-1092.
- HOSHINO, M., SANEMATSU, K., & WATANABE, Y. (2016). REE mineralogy and resources. *Handbook on the physics and chemistry of Rare Earths*, 49, 129-291.

- IRVINE, T.NEIL; BARAGAR, W. R. A, 1971 . A guide to the chemical classification of the common volcanic rocks. Canadian journal of earth sciences, v. 8, n. 5, p. 523-548.
- KAY, S.M., ARDOLINO, A.A., FRANCHI, M.R., RAMOS, V.A., 1992. The Somuncura Platean: An Oligo-Miocene «Baby-Hotspot» in Extra-Andean Patagonia. American Geophysical Unión, Spring meeting. Abstracts.
- KAY, S. M., ARDOLINO, A.A., FRANCHI, M.R., RAMOS, V.A., 1993. El origen de la Meseta de Somun Cura: distribución y geoquímica de sus rocas volcánicas mañas. 12° Congreso Geológico Argentino y 2° Congreso de Exploración de Hidrocarburos, Actas: 4: 236-248.
- KAY, S.M., RAMOS, V.A., & MARQUEZ, M., 1999. Evidence in Cerro Pampa volcanic rocks for slab-melting prior to ridge-trench collision in southern South America. Journal of Geology, 107(6), 693-715.
- KAY, S. M., ARDOLINO, A. A., GORRING, M. L., AND RAMOS, V. A., 2007. The Somuncurá Large Igneous Province in Patagonia: interaction of a transient mantle thermal anomaly with a subducting slab. Journal of Petrology, 48, 1, 43-77.
- KELLEY, K. A., COTTRELL, E., & O'LEARY, M., 2006. The Role of Crustal Contamination in the Petrogenesis of Basaltic Magmas. *Geochimica et Cosmochimica Acta*, 70(16), 3987-4003.
- LANA, C., GONÇALVES, G. O., MAZOZ, A., BUICK, I., KAMO, S., SCHOLZ, R., WANG, H., MOREIRA, H., BABINSKI, M., & QUEIROGA, G. (2022). Assessing the U-Pb, Sm-Nd and Sr-Sr Isotopic Compositions of the Sumé Apatite as a Reference Material for LA-ICP-MS Analysis. *Geostandards and Geoanalytical Research*, 46(1), 71-95.
- LE MAITRE RW (ed) (1989) Igneous Rocks: A Classification and Glossary of Terms, 1st edition. Cambridge University Press
- LI, Y., BROUWER, F. M., XIAO, W., WANG, K.-L., LEE, Y.-H., LUO, B., SU, Y., ZHENG, J., 2017. Subduction-related metasomatic mantle source in the eastern Central Asian Orogenic Belt: Evidence from amphibolites in the Xilingol Complex, Inner Mongolia, China. *Gondwana Research*, 43, 193–212.
- LIPMAN, P.W. 2000. "Calderas." In Sigurdsson, H. (Ed.), *Encyclopedia of Volcanoes* (pp. 643-662). Academic Press.
- LLAMBÍAS, E. J., CAMINOS, R., & RAPELA, C. W. (1984). Las plutonitas y vulcanitas del ciclo eruptivo gondwánico. In *Geología y recursos naturales de la provincia de Río Negro. Relatorio del IX Congreso Geológico Argentino, Asociación Geológica Argentina* (pp. 85-119).
- LUCASSEN, F., FRANZ, G., ROMER, R.L., & SCHULTE, E., 2002. Subduction and recycling of crust in the southern central Andes: The Late Cretaceous to Recent compositional evolution of the back-arc crust. *Journal of South American Earth Sciences*, 15(2), 153-174.

MAGNI, V. (2019). The effects of back-arc spreading on arc magmatism. *Earth and Planetary Science Letters*, 519, 141-151.

MÁRQUEZ, MARCELO J.; MASSAFERRO, GABRIELA I.; FERNÁNDEZ, MARÍA 2010. El volcanismo del complejo Marifil en Arroyo Verde, vertiente suroriental del Macizo de Somún Cura, Chubut. Revista de la Asociación Geológica Argentina, v. 66, n. 3, p. 314-324.

MCCULLOCH, M.T., & GAMBLE, J.A., 1991. Geochemical and geodynamical constraints on subduction zone magmatism. *Earth and Planetary Science Letters*, 102(3-4), 358-374

MCDOWELL, F. W., MCINTOSH, W. C., & FARLEY, K. A. (2005). A precise 40Ar–39Ar reference age for the Durango apatite (U–Th)/He and fission-track dating standard. *Chemical Geology*, 214(3-4), 249-263.

MCPHIE, J. (1993). *Volcanic textures: a guide to the interpretation of textures in volcanic rocks*.

MENEGATTI, N.D., MASSAFERRO, G.I., FERNÁNDEZ, M.I., GIACOSA, R.E., 2014. Geología y geoquímica de los cuerpos básicos alcalinos al sur de los lagos Musters y Colhué Huapí, cuenca del Golfo San Jorge, Chubut. *Rev. Asoc. Geol. Argent.* 71 (4), 484–499.

MIALL, A. D. (1996). Whither stratigraphy?. *Sedimentary Geology*, 100(1-4), 5-20.

MORIMOTO, N., FABRIES, J., FERGUSON, A.K., GINZBURG, I.V., ROSS, M.; SEIFERT, F.A.; ZUSSMAN, J., AOKI, K., GOTTARDI, G., 1988. Nomenclatura of pyroxenes. *Mineral.Magaz.*, 52: 535-550.

MURPHY, J.B., VAN STAAL, C.R., & COLLINS, W.J., 1998. Tectonic influence on the evolution of the Neoproterozoic to Cambrian Avalon arc terrane in the Canadian Appalachians. *Geology*, 26(10), 909-912.

NAKAYAMA, C., 1975. Informe geológico preliminar del área que comprende sierra de los Chacays, cañadón Trapaulco, cerro Ponte y parte del curso inferior del arroyo perdido. YPF inédito. Buenos Aires.

NAVARRETE, C., GIANNI, G., ENCINAS, A., MÁRQUEZ, M., KAMERBEEK, Y., VALLE, M., & FOLGUERA, A. 2019. Triassic to Middle Jurassic geodynamic evolution of southwestern Gondwana: From a large flat-slab to mantle plume suction in a rollback subduction setting. *Earth-science reviews*, 194, 125-159.

NAVARRETE, C., GIANNI, G., MASSAFERRO, G & BUTLER, K. (2020). The fate of the Farallon slab beneath Patagonia and its links to Cenozoic intraplate magmatism, marine transgressions and topographic uplift. *Earth-Science Reviews*, 210, 103379.

NUÑEZ, E.; E. W. BACHMANN; I. RAVAZZOLI; A. BRITOS; M. FRANCHI; A. LIZUAIN y E. SEPULVEDA. 1975. Rasgos geológicos del sector oriental del Macizo de Somuncurá, provincia de Río Negro, República Argentina. II Congr. Iberoamericano de Geología Económica IV: 247-266.

NUR, AMOS; BEN-AVRAHAM, Z. V. I. 1977. Lost Pacifica continent. *Nature*, v. 270, n. 5632, p. 41-43.

ORIHASHI, Y., MOTOKI, A., HALLER & M., SUMINO (2006). Petrogenesis of Somuncura plateau basalt in an extra back-arc province: Dehydration-induced melting of hydrous wadsleyite beneath northern Patagonia. In *The Meeting of the Americas, Foz do Iguazu, Brasil*.

ORIHASHI, Y., CHOI, T., LIM, H. S., & LEE, Y. I. (2010). Detrital zircon U-Pb ages of the late Paleozoic Sadong Formation in the Pyeongchang coalfield, Gangweon-do Province, Korea: implications for depositional age and provenance.

PANKHURST, R. J., & RAPELA, C. R. (1995). Production of Jurassic rhyolite by anatexis of the lower crust of Patagonia. *Earth and Planetary Science Letters*, 134(1-2), 23-36.

PATON, C., HELLSTROM, J., PAUL, B., WOODHEAD, J., HERGT, J., 2011. Iolite: freeware for the visualisation and processing of mass spectrometric data. *J. Anal. At. Spectrom.* 26, 2508–2518

PAVÓN PIVETTA, C., GREGORI, D., BENEDINI, L., GARRIDO, M., STRAZZERE, L., GERALDES, M., DOS SANTOS, A. C., & MARCOS, P. 2020. Contrasting tectonic settings in Northern Chon Aike Igneous Province of Patagonia: subduction and mantle plume-related volcanism in the Marifil formation. *International Geology Review*, 62(15), 1904-1930.

PEARCE, J.A. & PEATE, D.W., 1995. Tectonic implications of the composition of volcanic arc magmas. *Annual Review of Earth and Planetary Sciences*, 23, 251-285.

PEARCE, J. A., & STERN, R. J. (2006). Origin of back-arc basin magmas: Trace element and isotope perspectives. *Back-arc spreading systems: Geological, biological, chemical, and physical interactions*, 166, 63-86.

PEARCE, J. A. (2008). Geochemical fingerprinting of oceanic basalts with applications to ophiolite classification and the search for Archean oceanic crust. *Lithos*, 100(1-4), 14-48.

PHILPOTTS, A. R., & AGUE, J. J. (2009). *Principles of Igneous and Metamorphic Petrology*. Cambridge University Press.

RAMOS, V. A. 1975. Geología del sector oriental del macizo Nordpatagónico entre Aguada Capitán y la Mina Gonzalito, provincia de Río Negro. *Revista de la Asociación Geológica Argentina* 30(3): 274-285.

RAMOS, V. A. 1984. Patagonia: un continente paleozoico a la deriva?. In: 9º Congreso Geológico Argentino, SC Bariloche, Buenos Aires, 1984. p. 311-325.

RAMOS, V. A., & KAY, S. M. (1992). Southern Patagonian plateau basalts and deformation: backarc testimony of ridge collisions. *Tectonophysics*, 205(1-3), 261-282.

RAPELA, C. W., PANKHURST, R. J., FANNING, C. M., & HERVÉ, F. (2005). Pacific subduction coeval with the Karoo mantle plume: the Early Jurasssic

Subcordilleran belt of northwestern Patagonia. *Geological Society, London, Special Publications*, 246(1), 217-239.

REMESAL, M. B. (1988). *Geología y petrología de los basaltos de la meseta de Somuncurá* (Doctoral dissertation, Universidad de Buenos Aires. Facultad de Ciencias Exactas y Naturales).

REMESAL, M., GAGLIARDO, M., Y MÉNDEZ, M.J., 1996. Estructura, petrografía y geoquímica de las coladas basálticas en el límite noreste de la meseta de Somuncura. 12° Congreso Geológico Boliviano, Actas 2:473-482.

REMESAL, M., SALANI, F., FRANCHI, M. Y ARDOLINO, A., 1999. Hoja geológica 4169-IV, Maquinchao, provincia de Río Negro. Instituto de Geología y Recursos Minerales, inédito.

REMESAL, M., SALANI, F., FRANCHI, M., ARDOLINO, A. A., DALPONTE, M. R., ESPEJO, P. M., & LIZUAÍN, A. (2001). Hoja Geológica 4169 IV Maquinchao.

REMESAL, M., SALANI, F. M., MASSAFERRO, G. I., & CERREDO, M. E., 2004. Stratigraphy and petrology of the Northeastern sector of Sierra de Apas. Chubut Province. *Revista de la Asociación Geológica Argentina*, 59(4), 578-590.

REMESAL, M. B., SALANI, F. M., & CERREDO, M. E. (2012). Petrología del complejo volcánico Barril Niyeu (Mioceno inferior), Patagonia Argentina. *Revista mexicana de ciencias geológicas*, 29(2), 463-477.

RICHARDS, M.A., HAGER, B.H., & SLEEP, N.H., 1989. Dynamically supported geoid highs over hotspots: Observation and theory. *Journal of Geophysical Research: Solid Earth*, 94(B10), 13789-13804.

ROCHA-JÚNIOR, E.R.V., PUCHTEL, I.S., MARQUES, L.S., WALKER, R.J., MACHADO, F.B., NARDY, A.J.R., BABINSKI, M., FIGUEIREDO, A.M.G. 2012. Re-Os isotope and highly siderophile element systematics of the Paraná Continental Flood Basalts (Brazil). *Earth and Planetary Science Letters*, 337-338, 164-173.

SALAVATI, M. (2008). Petrology, geochemistry and mineral chemistry Caspian Sea Ophiolite, Northern Alborz, Iran: Evidence of Alkaline magmatism in southern Eurasia. *Journal of Applied Sciences*, 8(12), 2202-2216.

SALAZAR-NARANJO, A. F., & VLACH, S. R. F. (2023). New experimental constraints for the evolution and thermobarometry of alkali ultrabasic to intermediate igneous rocks. *Journal of Petrology*, 64(11), egad078.

SHAND, S.J., 1943. The Eruptive Rocks. 2nd Edition, John Wiley, New York, 444.

SHAW, DM., (1970. Trace element fractionation during anataxis. *Geochim Cosmochim Act* 34: 237-243.

SILVA NIETO, D.; CABALERI, N. & SALANI, F. 2003. Estratigrafía de la Formación Cañadón Asfalto (Jurásico Superior), provincia del Chubut, Argentina. *Ameghiniana*, Vol 40 :p. 46R.

- SMITH, R.L., & WHITE, J.D.L. 2013. Pyroclastic Rocks. Springer.
- STERN, R.C. 1987.  $^{87}\text{Sr}/^{86}\text{Sr}$  of mantle xenolith bearing plio-quaternary alkali basalts of the Patagonian plateau lavas of southernmost south America. Department of Geological Sciences, University of Colorado. USA 80309.
- STOREY, M., MAHONEY, J.J., SAUNDERS, A.D., DUNCAN, R.A., KELLEY, S.P., & COFFIN, M.F., 2012. Timing of hotspot-related volcanism and the breakup of Madagascar and India. *Science*, 314(5803), 587-591.
- SUN, S.S., McDONOUGH, W.F., 1989. Chemical and isotopic systematics of oceanic basalts: implications for mantle composition and processes. *Geological Society, London, Special Publications*, 42, 313-345
- TAYLOR, S. R., & MCLENNAN, S. M., 1995. The Geochemical Evolution of the Continental Crust. *Reviews in Geophysics*, 33(2), 241-265.
- TURNER, S., HAWKESWORTH, C., & ROGERS, N., 1996. U-Th isotope evidence for fluid transfer across the Tonga arc. *Philosophical Transactions of the Royal Society A: Mathematical, Physical and Engineering Sciences*, 355(1726), 1057-1064.
- VAN DER MEER, D.G., VAN HINSBERGEN, D.J.J., SPAKMAN, W., 2018. Atlas of the underworld: Slab remnants in the mantle, their sinking history, and a new outlook on lower mantle viscosity. *Tectonophysics* 723, 309–448
- VON GOSEN, W. 2003. Thrust tectonics in the North Patagonian Massif (Argentina): implications for a Patagonia plate. *Tectonics*, v. 22, n. 1.
- WEDEPOHL K.H. 1974. Strontium, Handbook Of Geochemistry. Berlin, Springer-Verlag, p. 38-A - 38-N.
- WHITE, W.M., HOFMANN, A.W. 1982. Sr and Nd isotope geochemistry of oceanic basalts and mantle evolution. *Nature*, 296, 821-825.
- WHITE, W.M., Geochemistry, Cornell Univ. An online textbook, eventually to be published by John-Hopkins University Press. Last modified 11/11/05, <http://www.geo.cornell.edu/geology/classes/geo455/chapters.HTML>
- WILSON, M. (Ed.). (1989). *Igneous petrogenesis*. Dordrecht: Springer Netherlands.
- WINCHESTER, JOHN A.; FLOYD, PETER A., 1977. Geochemical discrimination of different magma series and their differentiation products using immobile elements. *Chemical geology*, v. 20, p. 325-343.
- WINDHAUSEN, A., 1921. Ein Blick auf Schichtenfolge und Gebirgsbau im südlichen Patagonien. *Geologische Rundschau*, 12(3), 109-137.
- WINDHAUSEN, Anselmo. 1931. Geología argentina: segunda parte, geología histórica y regional del territorio argentino. Casa Jacobo Peuser.

WINTER J.D. 2001. An introduction to igneous and metamorphic petrology. London, Prentice Hall, 697 p.

WINTER, J. D. (2010). *Principles of Igneous and Metamorphic Petrology*. Prentice Hall.

YLLAÑEZ Y LEMA, 1979. Estructuras anulares y geología del noroeste de Telsen (provincia del Chubut). 7º Congreso Geológico Argentino. Actas 1:445-454.

ZAFFARANA, C. B., LAGORIO, S. L., GALLASTEGUI, G., WÖRNER, G., ORTS, D. L., GREGORI, D., POMA, S., BUSTEROS, A., GIACOSA, R., SILVA NIETO, D., RUIZ GONZÁLEZ, V., BOLTSHAUSER, B., PUIGDOMENECH, C., & HALLER, M. (2020). Petrogenetic study of the Lonco Trapial volcanism and its comparison with the Early-Middle Jurassic magmatic units from northern Patagonia. *Journal of South American Earth Sciences*, 101, 102624.

ZINDLER, A., JAGOUTZ, E., GOLDSTEIN, S. 1982. Nd, Sr and Pb isotopic systematics in a three-component mantle: a new perspective. *Nature*, v. 298, p. 519-523.

ZINDLER, A., HART, S.R., 1986. Chemical geodynamics. Annual reviews: Earth and Planetary Science Letters, v. 14, p. 493–571.

## APÊNDICE C - SAMPLE TABLE

Samples	S	W	Petrography	Lithogeochemistry	U-Pb	Nd and Sr
CAP 05	-42.0392	-67.4600	Trachyte	X	X	X
CAP 06	-42.0385	-67.4868	Basalt	X		
CAP 08 A	-42.0333	-67.4829	Tuff	X		
CAP 11 C	-42.0301	-67.4853	Tuff	X		
CAP 11E	-42.0301	-67.4853	Tuff	X		
CAP 13A	-42.0409	-67.4944	Trachyte	X		
CAP 14	-42.0427	-67.4947	Gabbro	X		X
CAP 15	-42.0460	-67.5007	Trachyte	X		
CAP 18	-42.0609	-67.5171	Commendite	X		X
CAP 19	-42.0584	-67.5650	Trachyte	X		
CAP 26	-42.0172	-67.4999	Trachyte		X	
CAP 31	-42.0132	-67.4770	Trachyte	X		
CAP 38	-42.0314	-67.4988	Basalt	X		
CAP 39A	-42.0324	-67.5036	Gabbro	X		
CAP 40	-42.0333	-67.5038	Trachyte	X	X	X
CAP 41	-42.0333	-67.5045	Gabbro	X		X
CAP 42	-42.0334	-67.5045	Gabbro			
CAP 45	-42.0351	-67.5131	Tuff	X		
CAP 53	-42.0460	-67.5969	Commendite	X		X
CAP 54	-42.0450	-67.5995	Trachyte	X		
CAP 55 A1	-42.0449	-67.5998	Commendite	X		
CAP 55 A2	-42.0449	-67.5998	Commendite	X		
CAP 56C	-42.0448	-67.6001	Commendite			
CAP 57 A	-42.0447	-67.6012	Commendite	X		
CAP 58	-42.1972	-67.4313	Basalt	X		X
CAP 59	-42.2329	-67.3952	Basalt	X		

## APÊNDICE D - PETROGRAPHIC TABLE

Samples	Lithology	Mineralogy	Intergranular relationship	Grain shape	Granulometry	Crystallinity	Texture
CAP 05	Trachyte	Essential minerals: feldspar 75% pyroxene 10%, quartz 10 %. Accessory minerals: opaque minerals 3%. Apatite 2%	Porphyritic	Subhedral	Fine (< 0,5 mm)	Holocrystalline	Trachytic Pilotassitic
CAP 06	Basalt	Essential minerals: plagioclase 55%, pyroxene 15% Iddingsite 15%, olivine 5%. Accessory minerals: opaque minerals 10%.	Subophitic	Subhedral	Fine (< 0,5 mm)	Hypocrystalline	Trachytic
CAP 08 A	Tuff	Essential minerals: feldspar 40% quartz 20% pyroxene 10% fragmentos líticos 10% Glass 10 % opaque minerals.5% carbonate 5%	More Juvenile than accessory fragments (70/30)	Anhedral	Ash (< 0,2 mm)	Holocrystalline	Pyroclastic

CAP 11 C	Tuff	Essential minerals: feldspar 30% quartz 20%, pyroxene 5% opaque minerals 5% very fine matrix - 40%	More accessory fragments than juvenile (70/30)	Anhedral	Lapilli (0.2 - 0.5 mm)	Holocrystalline	Pyroclastic
CAP 11E	Tuff	Essential minerals: feldspar 55%, quartz 20%, glass 15% opaque minerals 10%,	More juvenile than accessory fragments (80/20)	Anhedral	Lapilli (0.2 - 1 mm)	Holocrystalline	Pyroclastic
CAP 13A	Trachyte	Essential minerals: feldspar 78%, quartz 10%, pyroxene 7%, . Accessory minerals: opaque minerals 3%. Apatite 2%	Porphyritic	Subhedral	Fine (< 0,5 mm)	Holocrystalline	Trachytic Pilotassitic
CAP 14	Gabbro	Essential minerals: plagioclase 40%, pyroxene 30, olivine 15%, . Accessory minerals: opaque minerals 10%. quartz 5%	Inequigranular	Subhedral	Fine (>0,5 - <1 mm)	Holocrystalline	Subophitic
CAP 15	Trachyte	Essential minerals: feldspar 80%, quartz 10%, pyroxene 5%, . Accessory minerals: opaque minerals 4%. Apatite 1%	Porphyritic	Subhedral	Fine (< 0,5 mm)	Holocrystalline	Trachytic Pilotassitic

CAP 18	Commendite	Essential minerals: feldspar 60%, quartz 20%, pyroxene 15% Accessory minerals: opaque minerals 5%.	Porphyritic	Anhedral	Fine (< 0,5 mm)	Holocrystalline	Trachytic Pilotassitic
CAP 19	Trachyte	Essential minerals: feldspar 65% pyroxene 25%, quartz 5%. Accessory minerals: opaque minerals 4% Apatite <1%	Porphyritic	Anhedral	Fine (< 0,5 mm)	Holocrystalline	Trachytic Pilotassitic
CAP 26	Trachyte	Essential minerals: feldspar 70% pyroxene 20%, quartz 5%. Accessory minerals: opaque minerals 4% Apatite <1%	Porphyritic	Anhedral	Fine (< 0,5 mm)	Holocrystalline	Trachytic Pilotassitic
CAP 31	Trachyte	Essential minerals: feldspar 75% pyroxene 15%, quartz 5%. Accessory minerals: opaque minerals 4% Apatite <1%	Porphyritic	Subhedral	Muito fina (< 0,5 mm)	Holocrystalline	Trachytic Pilotassitic
CAP 38	Basalt	Essential minerals: plagioclase 55%, pyroxene 15% Iddingsite 15%,	Subophitic	Subhedral	Fine (< 0,5 mm)	Hypocrystalline	Trachytic

		olivine 5%. Accessory minerals: opaque minerals 10%					
CAP 39A	Gabbro	Essential minerals: plagioclase 45%, olivine 25%, pyroxene 20%, . Accessory minerals: opaque minerals 7%. quartzo 3%	Inequigranular	Subhedral	Fine (>0,5 - <1 mm)	Holocrystalline	Subophitic
CAP 40	Trachyte	Essential minerals: feldspar 80%, pyroxene 10%, quartz 5%, . Accessory minerals: opaque minerals 4% Apatite <1%	Porphyritic	Subhedral	Fine (< 0,5 mm)	Holocrystalline	Trachytic Pilotassitic
CAP 41	Gabbro	Essential minerals: plagioclase 45%, olivine 30%, pyroxene 15%, . Accessory minerals: opaque minerals 7%. quartzo 3%	Inequigranular	Subhedral	Fine (>0,5 - <1 mm)	Holocrystalline	Subophitic
CAP 42	Gabbro	Essential minerals: plagioclase 40%, olivine 25%, pyroxene 25%, . Accessory minerals: opaque minerals 5%. quartzo 3% alkali-feldspar 2%	Inequigranular	Subhedral	Fine (>0,5 - <1 mm)	Holocrystalline	Subophitic
		Essential minerals:	Mostly		Ash (< 0,2 mm)	Holocrystalline	Pyroclastic

CAP 45	Tuff	feldspar 70%, quartz 25%, opaque minerals 5%,	accessory fragments	Anhedral			
CAP 53	Commendite	Essential minerals: feldspar 60%, quartz 20%, pyroxene 15% Accessory minerals: opaque minerals 5%.	Porphyritic	Anhedral	Fine (< 0,5 mm)	Holocrystalline	Trachytic Pilotassitic
CAP 54	Trachyte	Essential minerals: f eldspar 90%, pyroxene 10%, . Accessory minerals: opaque minerals < 1%	Porphyritic	Subhedral	Fine (>0,5 - <1 mm)	Holohyalline	Perlite
CAP 55 A	Commendite	Essential minerals: feldspar 70%, quartz 15%, pyroxene 10% Accessory minerals: opaque minerals 5%.	Porphyritic	Subhedral	Fine (< 0,5 mm)	Hypocrystalline	Trachytic Pilotassitic
CAP 56C	Commendite	Essential minerals: feldspar 75%, quartz 10%, pyroxene 10% Accessory minerals: opaque minerals 5%.	Porphyritic	Anhedral	Fine (< 0,5 mm)	Holocrystalline	Trachytic Pilotassitic
CAP 57 A	Commendite	Essential minerals: feldspar 55%, quartz 15%, pyroxene 15% Accessory minerals: opaque minerals 5%.	Porphyritic	Anhedral	Fine (< 0,5 mm)	Holocrystalline	Trachytic Pilotassitic

CAP 58	Basalt	Essential minerals: plagioclase 55%, pyroxene 25% Iddingsite 5%, olivine 5%. Accessory minerals: opaque minerals 10%	Inequigranular	Subhedral	Fine (>0,5 - <1 mm)	Holocrystalline	Subophitic
CAP 59	Basalt	Essential minerals: plagioclase 50%, pyroxene 30% Iddingsite 5%, olivine 5%. Accessory minerals: opaque minerals 10%	Inequigranular	Subhedral	Fine (< 0,5 mm)	Hypocrystalline	Subophitic

